VERY HIGH ENERGY GAMMA-RAY EMISSION FROM TYCHO'S SUPERNOVA REMNANT

by

Dana Boltuch Saxon

A dissertation submitted to the Faculty of the University of Delaware in partial fulfillment of the requirements for the degree of Doctor of Philosophy in Physics

Spring 2014

© 2014 Dana Boltuch Saxon
All Rights Reserved

UMI Number: 3631211

All rights reserved

INFORMATION TO ALL USERS
The quality of this reproduction is dependent upon the quality of the copy submitted.

In the unlikely event that the author did not send a complete manuscript
and there are missing pages, these will be noted. Also, if material had to be removed,
a note will indicate the deletion.

UMI 3631211

Published by ProQuest LLC (2014). Copyright in the Dissertation held by the Author.

Microform Edition © ProQuest LLC.
All rights reserved. This work is protected against
unauthorized copying under Title 17, United States Code

ProQuest LLC.
789 East Eisenhower Parkway
P.O. Box 1346
Ann Arbor, MI 48106 - 1346

VERY HIGH ENERGY GAMMA-RAY EMISSION FROM TYCHO'S SUPERNOVA REMNANT

by

Dana Boltuch Saxon

Approved: _____
Edmund R. Nowak, Ph.D.
Chair of the Department of Physics and Astronomy

Approved: _____
George H. Watson, Ph.D.
Dean of the College of Arts and Sciences

Approved: _____
James G. Richards, Ph.D.
Vice Provost for Graduate and Professional Education

I certify that I have read this dissertation and that in my opinion it meets the academic and professional standard required by the University as a dissertation for the degree of Doctor of Philosophy.

Signed: _____

Jamie Holder, Ph.D.
Professor in charge of dissertation

I certify that I have read this dissertation and that in my opinion it meets the academic and professional standard required by the University as a dissertation for the degree of Doctor of Philosophy.

Signed: _____

Todor Stanev, Ph.D.
Member of dissertation committee

I certify that I have read this dissertation and that in my opinion it meets the academic and professional standard required by the University as a dissertation for the degree of Doctor of Philosophy.

Signed: _____

John Gizis, Ph.D.
Member of dissertation committee

I certify that I have read this dissertation and that in my opinion it meets the academic and professional standard required by the University as a dissertation for the degree of Doctor of Philosophy.

Signed: _____

Reshmi Mukherjee, Ph.D.
Member of dissertation committee

ACKNOWLEDGEMENTS

I would like to thank Dr. Jamie Holder for his guidance, patience, and enthusiasm during this long and winding journey.

I would like to thank Dr. Ester Aliu, Dr. Matthieu Vivier, Dr. Karsten Berger, and Sajan Kumar for their collaboration, conversation, and consideration.

I would like to thank the faculty members and support staff in the University of Delaware Department of Physics and Astronomy who taught and supported me. The expertise in this department is astounding, and I never could have broadened the horizons of my knowledge as far as I have without them.

I would like to thank my many colleagues and friends within the VERITAS collaboration. It has been a privilege to be a member of such a dedicated and wonderful group. I would also like to thank the technical support staff at the Fred Lawrence Whipple Observatory and at the collaborating institutions. They truly do keep us going.

I would like to express my sincerest thanks to the NASA Delaware Space Grant Program for supporting me through much of this research. I would also like to thank the several members of the Fermi-LAT team who have provided me with invaluable support and answered my many questions, particularly those who were involved with the Fermi Summer School.

Lastly, I would like to thank the friends and family who have provided me with so much support as I completed my dissertation. Without their encouragment (and babysitting services!), my achievement would not have been possible. In particular, I would like to thank A. Robin Bowles, librarian extraordinare, for both her professional and personal support during this process.

DEDICATION

I dedicate this work to my husband, Tony, my son, Connor, my parents, Nick and Melissa, and my brother, Peter. They have encouraged and inspired me to pursue this path, and I could not have made it this far without their unending love and support.

TABLE OF CONTENTS

LIST OF TABLES . . . . . **x**
LIST OF FIGURES . . . . . **xi**
ABSTRACT . . . . . **xvi**

Chapter

1 TYCHO'S SUPERNOVA REMNANT **1**

1.1 A Brief Historical Background 1
1.2 Modern Observations of Tycho's Supernova Remnant 4

2 SUPERNOVA REMNANTS AND COSMIC RAY ACCELERATION **9**

2.1 Cosmic Rays and Diffusive Shock Acceleration 9
2.2 Observational Evidence 15

2.2.1 Evidence of Accelerated Electrons and Unidentified Parent Particles 16
2.2.2 Evidence of Accelerated Hadrons 20

3 TEV GAMMA-RAY ASTRONOMY **24**

3.1 Very High Energy Gamma-Ray Production in Astrophysical Sources . 24

3.1.1 Leptonic Gamma-Ray Production 25

3.1.1.1 Inverse Compton Scattering 25
3.1.1.2 Bremsstrahlung 25

3.1.2 Hadronic Gamma-Ray Production 25

3.2 Gamma-Ray Absorption in Space 26

3.3 Atmospheric Air Showers & Cherenkov Radiation 29

3.3.1 Gamma Ray Air Showers 30
3.3.2 Cosmic Ray Air Showers 33

3.4 TeV Source Classes 37

3.4.1 Galactic Sources 37

3.4.1.1 Pulsar Wind Nebulae 38
3.4.1.2 Pulsars 40
3.4.1.3 Supernova Remnants 42
3.4.1.4 Stellar Winds and Superbubbles 44
3.4.1.5 Globular Clusters 45
3.4.1.6 Binaries 46
3.4.1.7 The Galactic Center 46
3.4.1.8 Unidentified Objects 48

3.4.2 Extragalactic Sources 48

3.4.2.1 Active Galactic Nuclei: Blazars, Flat Spectrum Radio Quasars, and Radio Galaxies 48
3.4.2.2 Starburst Galaxies 52
3.4.2.3 The Large Magellenic Cloud 53
3.4.2.4 Gamma-Ray Bursts 53
3.4.2.5 Dark Matter 55

4 INSTRUMENTATION FOR OBSERVING GAMMA RAYS . . . 56

4.1 Imaging Atmospheric Cherenkov Telescopes 56

4.1.1 Historical Instruments 56
4.1.2 Modern IACTs 58
4.1.3 VERITAS 60

4.1.3.1 Observing Constraints 60
4.1.3.2 Optics 63
4.1.3.3 Camera 63
4.1.3.4 Tracking and Pointing 65
4.1.3.5 Trigger System 66
4.1.3.6 Data Acquisition and Recording 68

4.2 Gamma-Ray Satellites 71

4.3 Ground-based Particle Detectors . . . 74

4.3.1 Water Cherenkov Telescopes . . . 74
4.3.2 Extensive Air Shower Arrays . . . 77

5 CHERENKOV TELESCOPE DATA ANALYSIS . . . 80

5.1 Data Quality Selection . . . 80
5.2 Calibration . . . 82

5.2.1 Flat-Fielding . . . 82
5.2.2 Pedestals . . . 83
5.2.3 Absolute Calibration . . . 87
5.2.4 Simulations . . . 90

5.3 Shower Reconstruction . . . 92

5.3.1 Image Cleaning . . . 92
5.3.2 Image Parameterization . . . 96

5.4 Generating Skymaps . . . 102

5.4.1 θ^2 Cut . . . 102
5.4.2 Background Signal Calculation . . . 103
5.4.3 Camera Acceptance and Exclusion Regions . . . 109

5.5 Generating Spectral Energy Distributions . . . 110

6 DETECTING GAMMA RAYS FROM TYCHO'S SUPERNOVA REMNANT . . . 114

6.1 VERITAS Data on Tycho . . . 114

6.1.1 Dataset . . . 114
6.1.2 Analysis . . . 115

6.1.2.1 Cuts . . . 117

6.1.3 Skymaps and Morphological Studies . . . 118

6.1.3.1 Statistical Trials . . . 118
6.1.3.2 Exclusion Region . . . 120
6.1.3.3 Morphological Studies . . . 120

6.1.3.4 Fitting a 2-D Gaussian Function to the Skymap . . . 121
6.1.3.5 Testing the Code on Tycho Background 125
6.1.3.6 Testing the Code on Other Source Backgrounds . . . 126
6.1.3.7 Results of Morphological Studies on Tycho 128
6.1.3.8 Other Attempted Fitting Functions 128
6.1.3.9 Likelihood Ratio Testing 131

6.2 Fermi Data on Tycho 131
6.3 Spectral Energy Distribution 132

6.3.1 TeV Spectrum of Tycho's SNR 132
6.3.2 GeV Spectrum of Tycho's SNR 137

7 MODELS, INTERPRETATIONS, AND FUTURE WORK 138

7.1 Models of MeV-TeV Emission from Tycho's Supernova Remnant . . . 138

7.1.1 Modeling of Hadronic Emission 138
7.1.2 Modeling of Leptonic Emission 145

7.2 Summary of Results 148
7.3 Future Work 150
7.4 Summary of Original Work and Conclusion 154

BIBLIOGRAPHY 156

Appendix

PUBLICATION PERMISSIONS 175

LIST OF TABLES

3.1 Gamma-ray shower parameters at various energies. 32

4.1 Properties of selected IACTs prior to the current generation. 59

4.2 Properties of the current generation of IACTs. 61

6.1 A summary of VERITAS observations of Tycho's SNR discussed in this work. 116

6.2 The differential flux points in the 1-10 TeV spectrum of Tycho data from 2008-2010. 134

6.3 The differential flux points in the 1-10 TeV spectrum of Tycho data from 2008-2011. 135

7.1 The estimated errors on differential flux points in the 1-10 TeV spectrum of Tycho data after 150 hours of observations with VERITAS. 151

LIST OF FIGURES

1.1 Left: Illustration from *De Nova Stella*. Right: Portrait of Tycho Brahe. 2

1.2 ^{12}CO radio map showing a molecular cloud at the northeastern boundary of Tycho's SNR. 7

2.1 The cosmic ray spectrum. 11

2.2 Comparison of shock profiles and particle energy distributions from shocks modified and unmodified by NLDSA. 14

2.3 Multiwavelength map and spectrum of RX J1713.7-3946. 18

2.4 *Chandra* image of Tycho's SNR showing nonthermal stripes. 21

2.5 *Fermi*-LAT spectra of IC 443 and W44. 23

3.1 H.E.S.S. measurement of the extragalactic background light. 28

3.2 Diagram of an electromagnetic air shower. 33

3.3 Diagram of a hadronic air shower. 35

3.4 Lateral shower profiles of Cherenkov light from electromagnetic and hadronic air showers. 36

3.5 TeV all-sky map. 37

3.6 Spectrum of the Crab Nebula from *Fermi*-LAT data, demonstrating synchrotron self-Compton emission. 39

3.7 Energy dependent morphology of PWN J1825-137. 41

3.8 Spectrum of the Crab Pulsar from VERITAS data. 43

3.9 Orbit-to-orbit variability in binary LS I+61°303. 47

3.10 Multiwavelength observations of unidentified source TeV J2032+4130. 49

3.11 Spectrum of Markarian 501. 51

3.12 VHE image of M82. 54

4.1 The first major VHE telescope, operated in the Crimea. 57

4.2 The Whipple 10 m gamma-ray telescope. 58

4.3 The two layouts of the VERITAS array, pre- and post-summer 2009. 62

4.4 VERITAS telescope mirror reflectivity vs. wavelength. 63

4.5 Measured photon detection efficiency and quantum efficiency of new VERITAS PMTs. 65

4.6 Example of a bias curve. 68

4.7 Example of an offset muon ring as seen in a VERITAS camera. . . 69

4.8 Example of an event FADC trace. 70

4.9 Schematic of the VERITAS trigger system and data acquisition system. 71

4.10 *Fermi*-LAT performance plots. 75

4.11 Schematic diagram of the *Fermi*-LAT telescope. 76

4.12 Illustrations of the HAWC water Cherenkov telescope. 77

4.13 All-sky map as seen by Milagro. 78

5.1 Example of FIR data. 82

5.2 Example of a relative high-gain distribution for one telescope. . . . 84

5.3 Example of the distribution of charges measured in a single PMT during a flasher run. 85

5.4 Example of a pedestal event FADC trace. 86

5.5 Example of a bright Cherenkov event FADC trace. 87

5.6 Left: The "holey plate" used for single photoelectron measurements. Right: histogram showing peaks for 0, 1, 2, 3, and 4 photoelectrons. 89

5.7 Example of lookup tables for width (left) and length (right). 92

5.8 CORSIKA simulations illustrating air showers initiated by a 1 TeV photon (left) and a 1 TeV proton (right). 94

5.9 Examples of images produced in a VERITAS camera by a hadronic air shower (left), and a possible electromagnetic air shower (right). 95

5.10 Cartoon illustrating the development of the air shower across the camera. 96

5.11 Cartoon illustrating the main Hillas parameters of an image. 97

5.12 Diagram showing the projection of an air shower onto the image plane of a telescope. 99

5.13 Cartoon of an event seen by all four VERITAS telescopes. 100

5.14 Example of distributions of mean scaled width (left) and mean scaled length (right). 102

5.15 Histogram showing the θ^2 value of reconstructed events for a point source. 104

5.16 Cartoon illustrating the ring background model (left) and the reflected region background model (right). 107

5.17 Cartoon illustrating how correlated sky maps are produced. 108

5.18 Example of an acceptance curve. 110

5.19 Example of a gamma-ray signficance map showing bright stars and exclusion regions. 111

5.20 Example of an effective area curve at various zenith angles. 113

5.21 Spectrum of the Crab Nebula before (left) and after (right) the inclusion of the effective area curve. 113

6.1 Uncorrelated difference maps of VERITAS data on Tycho's SNR from 2008-2010 (left), and 2008-2011 (right). 121

6.2 Map of excess events from VERITAS observations of Tycho's SNR from 2008-2010. 122

6.3 Fraction of vertical gamma-ray showers triggering n_T telescopes as a function of the impact position on the ground. 123

6.4 θ^2 distribution from 1 TeV gamma-ray showers simulated at zenith. 124

6.5 χ^2 distribution of results of fit to symmetric test Gaussian superimposed on Tycho background data from 2008-2010. 127

6.6 Map of excess events from VERITAS observations of Tycho's SNR from 2008-2011. 129

6.7 TS map of Tycho's SNR from 34 months of *Fermi*-LAT data. . . . 133

6.8 The differential gamma-ray photon spectrum of VERITAS data on Tycho's SNR from 2008-2010. 135

6.9 The differential gamma-ray photon spectrum of VERITAS data on Tycho's SNR from 2008-2011. 136

6.10 The SED data points from *Fermi*-LAT and VERITAS detections of Tycho's SNR. 137

7.1 Spectral energy distribution of radio, X-ray, and VHE gamma-ray emission from Tycho's SNR, along with models of the emission. . . 139

7.2 Broadband SED models of Tycho's SNR from *Fermi*-LAT data assuming leptonic emission (left) and hadronic emission (right). . . 141

7.3 Models of hadronic and leptonic emission from Tycho's SNR by Morlino & Caprioli. 142

7.4 Model of hadronic emission from Tycho's SNR by Berezhko, Ksenofontov, and Völk. 143

7.5 Model of hadronic emission from Tycho's SNR by Zhang, et al.. . . 145

7.6 Model of leptonic emisson from Tycho's SNR by Atoyan & Dermer. 147

7.7 All models proposed to explain the GeV and TeV emission from Tycho's SNR. 148

7.8 The published TeV SED of Tycho's SNR, and the estimated TeV SED of Tycho's SNR after 150 hours of observations with VERITAS. 152

7.9 The published and predicted spectrum of Tycho's SNR from *Fermi*-LAT and VERITAS data, along with models of the emission. 153

ABSTRACT

Supernova remnant (SNR) G120.1+1.4 (also known as Tycho's SNR) is the remnant of one of only five confirmed historical supernovae. As such, it has been well studied across the electromagnetic spectrum. This thesis describes the first statistically significant detection of very high energy (VHE) ($\sim$100 GeV to 100 TeV) gamma rays from Tycho's SNR, reported in 2011 by the VERITAS collaboration. The analysis that led to that detection was performed by this author, and this dissertation will discuss the process in detail. Subsequently, a statistically significant detection in high energy (HE) ($\sim$30 MeV to 100 GeV) gamma rays was reported by other authors using data from the Fermi Gamma-Ray Space Telescope. Comparison of models to the spectral energy distribution of the photon flux from this remnant in HE and VHE gamma rays favors a hadronic origin for the emission, particularly when combined with current X-ray data, although a leptonic origin cannot be ruled out at this time. This is significant because a confirmed hadronic origin for the gamma-ray emission would identify this SNR as a site of cosmic ray acceleration, providing observational evidence for the idea that SNRs are the source of the Galactic cosmic ray population.

Chapter 1 of this dissertation will provide historical background on Tycho's SNR, along with a summary of modern observations of the remnant across the electromagnetic spectrum. Chapter 2 is a discussion of the role played by SNRs in the process of cosmic ray acceleration, including both theoretical underpinnings and observational evidence. Chapter 3 provides an overview of the field of VHE gamma-ray astronomy, with discussions of gamma-ray production mechanisms and gamma-ray source classes. Chapter 4 describes the instruments used to observe HE and VHE gamma rays. Chapter 5 is a discussion of general analysis methods and techniques for data from Imaging Atmospheric Cherenkov Telescopes (IACTs). Chapter 6 provides details about the

specific analysis I completed on VERITAS data on Tycho's SNR. Lastly, Chapter 7 discusses the modeling and interpretation of the VHE Tycho detection in the context of current multiwavelength observational results.

Chapter 1

TYCHO'S SUPERNOVA REMNANT

1.1 A Brief Historical Background

Tycho Brahe was undoubtedly one of the great early astronomers. Born in Denmark in 1546 to an upper class family, he was one of ten children. He was educated at the University of Copenhagen and at the University of Leipzig, taking an interest in astronomy despite his family's desires that he study law and rhetoric to prepare for a career as a statesman. In particular, the solar eclipse of 1560 solidified his interest in astronomy. While a student, he studied the work of Ptolemy, who had attempted to explain the motions of the planets, and he made the most accurate measurements to date of the positions of stars, including estimations of errors on the measurements. The instruments he had available to him for his observations were compasses, cross-staves, and sextants, as the telescope had not yet been invented [1].

In 1572, Brahe cemented his reputation as a brilliant astronomer. On the evening of November 11, he noted a new, very bright star in the constellation Cassiopeia. It was so bright that he asked his servants if they, too, could see it, to be sure he was not hallucinating. He immediately took measurements of its position, with the intention of determining its distance by tracking its motion. Since it could be seen in daylight, measurements of its position at 12 hour intervals quickly revealed that it was not moving, and hence must be at a much farther distance than the moon. This was revolutionary, since it ran counter to the Aristotalean view that the heavens were unchanging with the exception of atmospheric effects, which were closer than the moon. He continued to record the star's position, brightness, and color for many weeks, publishing his observations in *De Nova Stella* in 1573 (see Figure 1.1) [1]. It is this 'star'

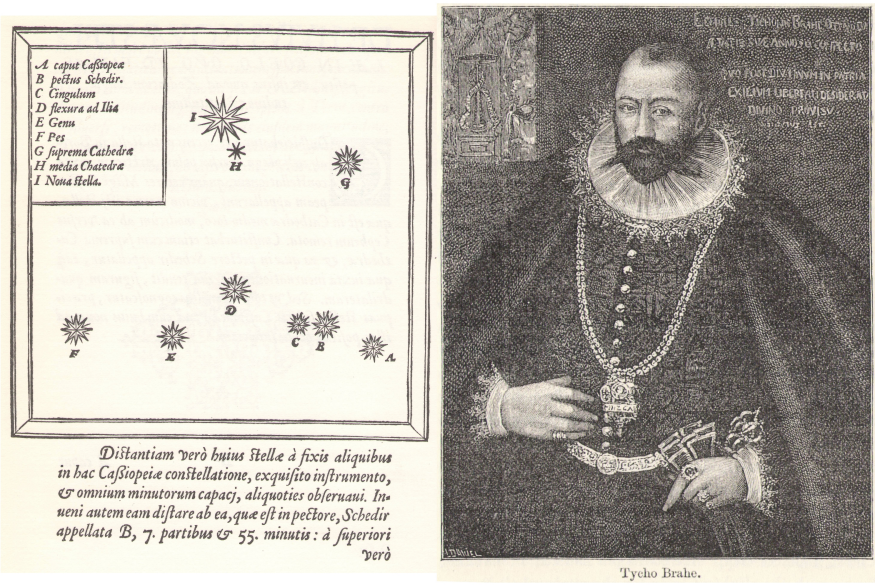

Figure 1.1: Left: Illustration from Tycho Brahe's *De Nova Stella* showing the position and relative brightness of the supernova (I) [4]. Right: Portrait of Tycho Brahe [1].

that is now referred to as Tycho's supernova (SN), and the remnant associated with the explosion will be the main subject of this work. Although Tycho made by far the most detailed and lengthy observations of this 'star', it is worth noting that five records from China, two from Korea, and several others from Europe also note its presence. In fact, records from Korea and the records of Maurolycus, abbott of Messina, note its presence on November 6, a few days sooner than it came to Tycho's attention [2], likely due to poor weather in Denmark [3]. Actually, since it was so bright as to be visible in daylight, Tycho's SN became a bit of a cultural phenomenon, possibly even being referenced years later in the opening scene of Shakespeare's *Hamlet* [3].

Brahe's publication of *De Nova Stella* earned him much publicity, and he was invited by King Frederick II of Denmark to become a lecturer at the University of Copenhagen. His work was also very well-received in Germany, and he considered moving there. To entice him to remain in Denmark, King Frederick II provided him with a place to focus on his studies. The Island of Hven was given to him, and

upon it were built a house and the greatest observatory of the time, the castle of Uraniborg. Soon, Brahe had many students, and a second observatory was constructed to accommodate them. This observatory housed its instruments below ground, with only the building roofs appearing above ground level, in order to minimize the effect of vibrations on the accuracy of measurements. Among his assistants was Johannes Kepler, who later became a great astronomer in his own right. After Brahe's death his observations were left to Kepler, who built on them, eventually using this large body of accurate data to determine the laws of planetary motion [1].

In addition to being a respected astronomer, Tycho was also a rather colorful character. In 1566, he had a disagreement with another Danish astronomer nobleman. To settle the disagreement they held a nighttime duel, in which Tycho lost his nose. He replaced it with a prosthetic reportedly made of silver and gold [1], although an examination of his exhumed corpse in 1901 revealed that it contained enough copper to leave green marks on his skull [5]. He married a commoner with whom he had eight children [1], employed a dwarf court jester named Jeppe who was reported to be clairvoyant, and had a pet elk who died after becoming drunk on beer at a nobleman's party and falling down the stairs [6]. Tycho himself died in an interesting manner as well; on October 13, 1601 he attended a dinner at which he had consumed much to drink, and felt it impolite to leave the table to relieve himself. After this, he suffered a serious bladder condition and died eleven days later. However, a 1996 analysis of samples of his remains exhumed in 1901 reveals a high concentration of mercury, taken in one large dose within 20 hours prior to his death. Thus, he most likely died of mercury poisoning rather than a bladder infection. It remains unknown whether the mercury was ingested purposely as an attempt at treating his bladder, or unknowingly at the hands of a murderer. It is speculated that both Kepler and the Danish King at the time, Christian IV, had motive, although this mystery is likely to remain unsolved [7].

1.2 Modern Observations of Tycho's Supernova Remnant

Supernova remnants (SNRs) are an active area of study in modern astronomy. In addition to revealing a great deal about stellar evolution, they are likely to be the primary acceleration sites for the Galactic cosmic ray (CR) population, whose origin is as yet undetermined. While this premise has yet to be firmly proven observationally, arguments of energetics point to SNRs as the most likely source for these CRs. This aspect of the importance of SNRs will be explored in detail in Chapter 2, Section 2.1.

As one of only a handful of historical SNRs, Tycho's SNR has been very well studied throughout the electromagnetic spectrum. Historical remnants are those remnants within the Milky Way whose explosions were observed and recorded in human history, and hence whose ages are known precisely. In addition to Tycho's SNR, Kepler's SNR (SN 1604), the Crab Nebula (SN 1054), 3C58 (SN 1181), and the remnant associated with SN 1006 are historical remnants. There are also historical records of supernovae observed in AD393 and AD185, and records of possible supernovae in AD386 and AD369, although the positions of these objects were not recorded with sufficient precision to associate them unambiguously with a particular SNR. Several other historical references to "new" stars exist, including one that is positionally very near to the radio-bright SNR Cassiopeia A, but upon further investigation these were variously likely observations of meteors, comets, or novae, or measurement errors on existing stars [2].

It has been established that Tycho's SNR is the result of a Type Ia supernova (SN) [8]. Type Ia SNe are explosions that result from the mass of a carbon and oxygen white dwarf exceeding the Chandrasekhar limit ($\sim$1.4 M$\odot$). Traditionally, the progenitor system for Type Ia SNe has been thought to be a white dwarf and a companion star in a binary system, with the white dwarf accreting material from the companion star; this is known as the single-degenerate model. However, a double-degenerate model involving the merging of two CO white dwarfs can also produce an explosion consistent with observations, and other, more exotic scenarios have been proposed (see, e.g., [9] for a review). In any scenario, no stellar remnant is left after the

explosion, only the material which has been blown out in a cloud, forming a SNR (see, e.g., [10]). Through optical observations of the light echo from the explosion of Tycho's SN, Krause et al. have obtained a spectrum of the explosion which firmly identifies it as a normal (as opposed to overluminous or subluminous) Type Ia SN [8]. The spectra of Type I SNe show that the progenitor star contained no hydrogen, unlike Type II and Type III SNe. Type Ia are further distinguished by a notable silicon absorption line at 6335 Å at maximum luminosity, along with other identifying spectral features (see, e.g., [8]).

In the traditional model, since the progenitor star in a Type Ia SN is always the same mass, the explosions are assumed always to have the same absolute luminosity. Because of this, they have been used as "standard candles" in astronomy, and as such have provided distance estimates on intergalactic scales. However, in 1993, Phillips discovered that there are intrinsic differences in the absolute magnitudes of individual Type Ia SNe, and determined that there is a correlation between the peak luminosity of the SN and the rate of the initial decline in luminosity [11]. This is explained most simply by a range of progenitor masses. Quite recently, Scalzo et al. have found more direct evidence that Type Ia SNe progenitors have a range of masses from $\sim 0.9 - 1.4$ M$\odot$, with a strong correlation between the mass and the width of the light curve [12]. The role of these objects as standard candles is therefore still useful, but these adjustments must be accounted for. Furthermore, the canonical explanation of identical progenitor systems for these explosions is looking less and less likely.

Although a well-studied historical remnant from a Type Ia SN, Tycho's SNR (also known as G120.1+1.4, 3C10, or SN 1572) does not necessarily provide an idealized example of an evolving SNR. While much is known about this system, there are lingering questions about both its distance and its surrounding environment.

Various methods of estimating the distance have given results ranging from 1.5 kpc [13, 14] to $\geq$6 kpc [15], although most recent results have generally been in the range of 2-3 kpc. Unfortunately, its luminosity at the time of the explosion could not be measured accurately enough to apply the "standard candle" estimate, and the

light echo does not reflect the original luminosity. Using spectral Hα line widths to estimate shock velocity and combining it with proper motion measurements, Chevalier et al. found a distance of 2.3±0.5 kpc [16]. Using the same method with more recent observations, Smith et al. later estimated a distance between 1.5 and 3.1 kpc [13, 14]. A sample of distance estimates based on HI absorption gave results between $2.2^{+1.5}_{-0.5}$ kpc [17] and ≥6 kpc [15], with a more recent estimate of 4.5±0.5 kpc [18]. It should be noted, however, that this method relies heavily on modeling of the velocity in the Perseus arm of the Milky Way, where Tycho's SNR is located, and that the velocity field in that direction is complex. In recent years, a 2010 result from Hayato et al. combines *Suzaku* X-ray measurements of ejecta velocites with *Chandra* X-ray measurements of proper motion to derive a distance of 4±1 kpc [19]. A 2008 model of the gamma-ray emission by Volk et al. based on the TeV detection upper limits that were available at the time derived a lower limit for the distance of 3.3 kpc [20]. It bears mentioning that many of the shorter distance estimates assume adiabatic (no transfer of heat) expansion, and rely on calculations involving the temperature of shocked protons and the velocity of the shock front in this case. If efficient particle acceleration is occurring in this remnant, these assumptions may not be valid (see, e.g., Helder et al. [21]).

It is well established that a molecular cloud (MC) lies along the line of sight of the northeastern portion of Tycho's SNR. The question remains, however, whether the MC is interacting with the SNR, or lies in front of or behind the remnant. VLA observations of the 21-cm HI line show evidence of an interaction between Tycho's SNR and a high-density cloud of neutral hydrogen, particularly towards the eastern half of the remnant [22]. Additionally, VLA measurements of the expansion rate show that the eastern portion of the remnant is expanding slower than the rest of the remnant, further indicating a possible interaction with a dense medium in that area [23]. Separately, an analysis of ^{12}CO radio data shows evidence of a MC at the northeastern boundary of the remnant (see Figure 1.2) [24]. However, Tian & Leahy conclude from HI absorption spectra that the cloud lies in front of the remnant [25].

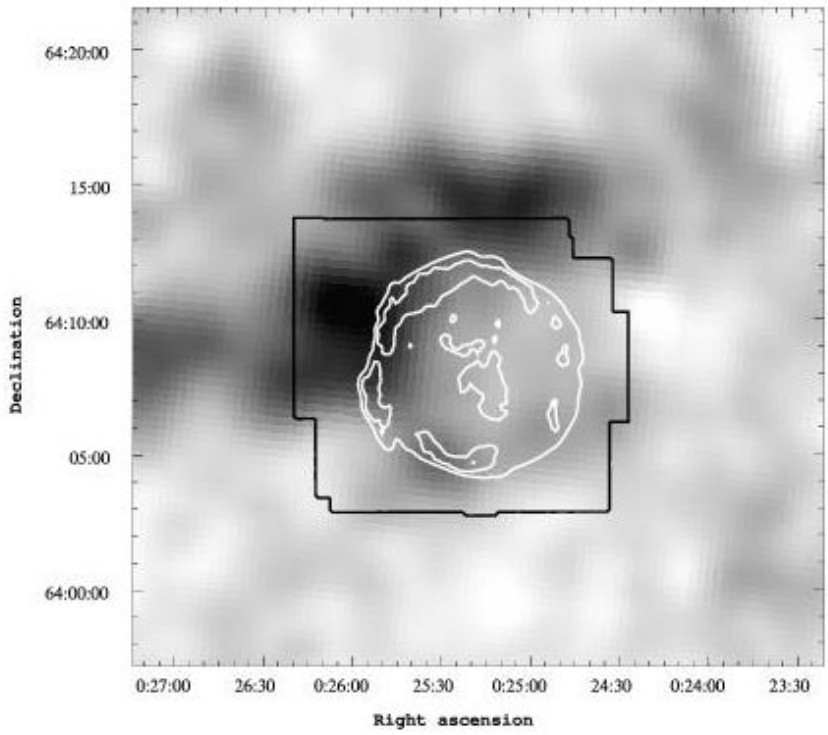

Figure 1.2: Figure 1 from [24]. ©AAS. Reproduced with permission. "Integrated channel map of ^{12}CO from FCRAO [Five College Radio Astronomy Observatory] data (-68 km s$^{-1}\leq v \leq$ -59 km s^{-1}). *White contour:* 1420 MHz radio continuum. *Black boundary:* Nobeyama [45 m radio telescope] observed region."

The question of whether or not the MC is interacting with the remnant is particularly interesting in the context of very high energy (VHE) gamma-ray emission. If it is interacting, the MC provides target material for any accelerated hadrons from the remnant to collide with, leading to the production of gamma rays. Thus, substantial hadronic gamma-ray emission produced by interaction with the MC provides a "smoking gun" for the presence of a large population of accerated hadrons (i.e., CRs). Again, this process will be explored further in Chapter 2.

For many years, Tycho's SNR, despite being an excellent candidate for VHE emission from accelerated CRs, remained undetected at TeV energies. Between 1993

and 1996, the Whipple telescope observed Tycho for ∼14.5 hours. They found a 99% confidence upper limit of 0.8×10^{-11} photons cm^{-2} s^{-1} [26]. In 1997-1998, HEGRA observed this remnant for ∼65 hours. They established a 3σ upper limit of 5.78×10^{-13} photons cm^{-2} s^{-1} for emission above 1 TeV [27]. At the 2009 International Cosmic Ray Conference, the MAGIC collaboration reported 3σ integral upper limits for point-like emission at the remnant center of 2.95×10^{-13} photons cm^{-2} s^{-1} above 1 TeV, and 1.86×10^{-12} photons cm^{-2} s^{-1} above 350 GeV from 69.4 hours of observations [28].

In 2011, VERITAS reported the first detection of Tycho's SNR at TeV energies [29]. The analysis and interpretation of that data will comprise a major portion of this work.

Chapter 2

SUPERNOVA REMNANTS AND COSMIC RAY ACCELERATION

2.1 Cosmic Rays and Diffusive Shock Acceleration

Cosmic rays (CRs) are free, charged, relativistic particles traveling through space. They mainly consist of protons (90%) and alpha particles (9%), but heavier elements, electrons, positrons, and antiprotons can also be present [30]. Although these particles are constantly bombarding the Earth, the exact details of their origin and acceleration remain unclear; because of their electric charge, the paths they travel are changed by interactions with magnetic fields in space. Thus, while they can be detected here on Earth, their direction of travel at the time of detection does not necessarily indicate their direction of origin. CRs constitute a significant portion of the Galactic energy budget, so it is important to understand where that energy is coming from and how it is being transferred to the CR population.

Although we do not know for certain the origin of all CRs, we do know that they span an enormous range in energy. The spectrum of CRs, shown in Figure 2.1, has two noteworthy features: the "knee" and the "ankle". Up to the knee, around 10^{15} eV, the spectrum behaves as a smooth power law of index 2.7. At the knee, the spectral index steepens to $\sim$ 3.0. At the ankle, around 10^{19} eV, the spectrum flattens to a power law of index 2.6 [31]. It is worth mentioning explicitly that the flux of CRs drops off rapidly with increasing energy; at 100 GeV (10^{11} eV), we observe $\sim$1 particle/m^2/s, while at the knee we observe $\sim$1 particle/m^2/year. Current thinking is that below the knee, CRs are likely accelerated within our Galaxy, and that a combination of galactic and extragalactic CRs comprise the population above the knee (see, e.g., [32], [30]) . The reasoning for this is two-fold: first, it is difficult to accelerate particles to energies

above the knee, so there are not many particles of that energy to start with, and second, those few particles that reach those energies diffuse out of the galaxy relatively quickly. An example of this can be calculated with the following equation [33]:

$$r_g = 100 \frac{E_{20}}{ZB_{-9}} Mpc$$

where r_g is the gyroradius of the particle in question, E_{20} is the energy of the particle in question in units of 10^{20} eV, Z is the particle charge, and B_{-9} is the magnetic field strength in units of 10^{-9} G (nG). For a 10^{20} eV proton (Z = 1) in a typical interstellar magnetic field of 1 μG (1000 nG), the gyroradius will be 0.1 Mpc = 100 kpc. The diameter of the Milky Way is ∼30 kpc, so particles with energy that high will easily diffuse out of the Galaxy. Lower energy particles will have smaller gyroradii, and higher energy particles will have even larger gyroradii.

Supernova remnants (SNRs) have been thought to be the site of Galactic CR acceleration since the idea was introduced by Zwicky in 1939 [35][36]. The main argument for this is based on energetics. Following Gaisser [30], the total power required to supply the Galactic cosmic ray population is $\sim 5 \times 10^{40}$ erg/sec. A typical SNR provides power on the order of $\sim 10^{42}$ erg/sec [30]. So, even as little as a few percent of the energy from a SNR would be enough to maintain the overall energy contained in Galactic CRs.

One must also consider the maximum energy to which a SNR shock can accelerate a particle. There are three possible limitations to the maximum particle energy: the age of the SNR (and hence, the finite acceleration time available to particles), radiative losses (mainly a consideration for electrons), and the escape of particles upstream[1] based on energy-dependent changes to the diffusion coefficient κ. The approximate

[1] Note that the terms "upstream" and "downstream" are relative to the shock; material upstream of the shock is in the environment surrounding the SNR, yet to experience the shock

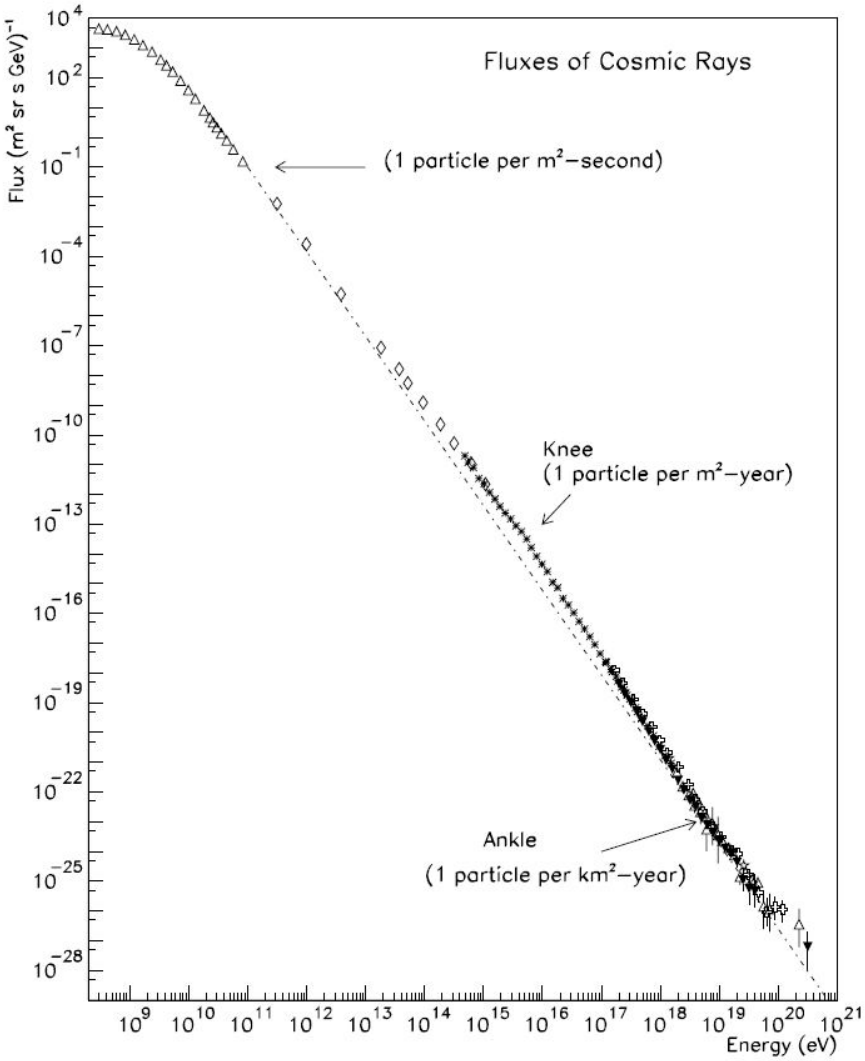

Figure 2.1: Figure 1 from [34]. "The all particle spectrum of cosmic rays - prepared by [S. Swordy] for Cronin *et al.* (1997)."

equations describing these situations are provided below [32]:

$$E_{max}(\text{age, pre-Sedov}) \sim 0.5{u_8}^2 t_3 B_{\mu G}(\eta R_J)^{-1}\text{TeV}$$

$$E_{max}(\text{age, post-Sedov}) = 5E_{max}(\text{age, pre-Sedov})t_{ch}\left[1 - \left(\frac{t}{t_{ch}}\right)^{-0.2}\right]$$

$$E_{max}(\text{rad. loss}) \sim 100u_8(\eta R_J B_{\mu G})^{-\frac{1}{2}}\text{TeV}$$

$$E_{max}(\text{escape}) \sim 10B_{\mu G}\lambda_{17}\text{TeV}$$

where $u_8 \equiv \frac{u_1}{10^8 cm}$ and u_1 is the upstream flow velocity, $t_3 \equiv \frac{t}{1000yrs}$, $B_{\mu G}$ is the upstream magnetic field in microGauss, $\lambda_{17} \equiv \frac{\lambda_{max}}{10^{17}cm}$ and λ_{max} is the maximum wavelength of magentohydrodynamic (MHD) waves present, $\eta \equiv \frac{\lambda_{mfp}}{r_g}$ is the gyrofactor and λ_{mfp} is the effective mean free scattering path of the particle, $R_J(\theta_{Bn})$ is a parameter varying between 1 at $\theta_{Bn} = 0$ and $\frac{1}{1+r_{comp}}$at $\theta_{Bn} = 90°$, where θ_{Bn} is the shock obliquity (the angle between shock normal and the external magnetic field) and $r_{comp} \equiv \frac{\rho_{downstream}}{\rho_{upstream}}$ is the shock compression ratio, and t_{ch} is the age at which the Sedov-Taylor stage of evolution of the remnant (when the mass of material swept up by the remnant exceeds the mass of the ejecta from the remnant [37]) is reached. Typical values for SNR environments easily allow particles to be accelerated to TeV energies.

As additional evidence that SNRs are capable of accelerating the Galactic CR population, the spectrum of particles accelerated in SNRs is predicted to have a similar power-law index (~ 2) to that of CRs below the knee, and the difference in the indices can be explained by the energy dependent confinement time of particles within the galaxy [38]. Lastly, CR electrons have been observed to be accelerated in SNR shocks, so it seems reasonable to think that CR ions might be accelerated at these same sites [39].

The mechanism by which SNRs are thought to accelerate CRs is through diffusive shock acceleration (DSA), also known as first-order Fermi acceleration. The idea was first introduced by Fermi in 1949 [40], and was refined to its current form in

the late 1970s (see, e.g., [32]). In DSA, charged particles are reflected back and forth across a shock front by magnetic irregularities on either side of the shock. With each reflection, they are accelerated (see, e.g., [32] for a review). This process results in a nonthermal power-law energy distribution of particles, with an exponential cutoff at some maximum energy determined by environmental constraints (e.g., lack of scattering centers of appropriate wavelength for resonant scattering, radiative losses in the case of electrons, limited remnant size/age).

While the simple DSA model does result in a population of test particles with a power-law energy spectrum, it treats the test particles as energetically unimportant, and so does not include the effects of the particles on the shock and surrounding environment. For this, non-linear diffusive shock acceleration (NLDSA) must be used. In NLDSA, the scattering of the particles off of MHD fluctuations upstream of the shock causes the upstream fluid to decelerate [32]. This leads to a larger compression ratio r_{comp} between the upstream and downstream fluid velocities, as shown in panel (a) of Figure 2.2. Additionally, since particles of higher energy will typically scatter further ahead of the shock front, those higher energy particles in NLDSA experience the larger compression ratio, leading to a harder spectrum. This is shown in panel (b) of Figure 2.2.

Another difficulty with the basic DSA model lies with the MHD fluctuations which scatter the particles. These fluctuations are present in the interstellar medium, but their amplitude there is too small to constrain energetic particles to the local SNR environment. NLDSA solves this problem by including the effect that the accelerated particles themselves excite MHD waves, which then scatter later generations of particles. This idea was first proposed by Bell in 1978 [41], and was later refined by Bell and Lucek [42]. Numerical simulations done by Lucek and Bell [43] generate a highly irregular magnetic field near the shock front with amplification of Fourier components near the resonant wavelengths for the particles under consideration. This means that lower energy particles, while affected by the overall magnetic field, are more strongly scattered by the appropriate amplified components, and higher energy particles hardly

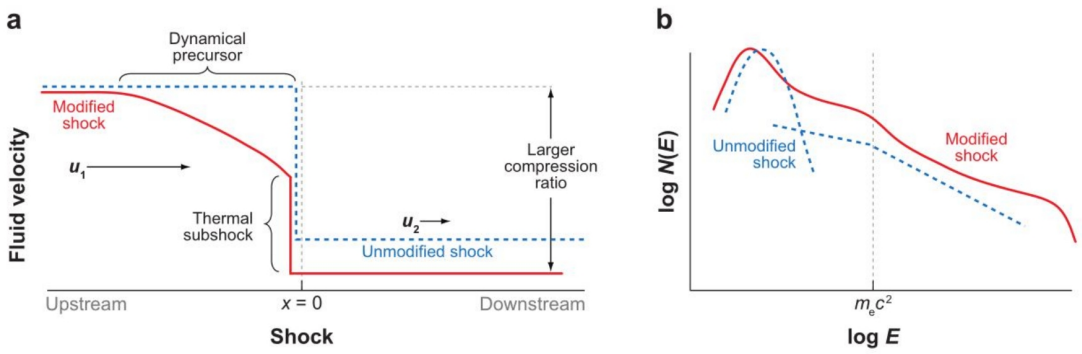

Figure 2.2: Figure 3 from [32]. "(a) Schematic shock profile. Dotted blue line, unmodified shock; solid red line, shock modified by accelerated particles. (b) Corresponding schematic particle energy distributions from unmodified shock (*dotted blue lines*) and modified shock (*solid red line*)."

respond at all to the overall magnetic field, seeing the appropriate amplified components almost exclusively [44].

A difficulty which NLDSA has not solved comes in the form of the "injection problem". In order for a particle to cross the shock front in the first place to begin this acceleration process, it must have sufficient initial energy. For ions, the shock front is only a few thermal gyroradii thick, and having an energy only a few times the mean energy of the population is sufficient. In a Maxwellian distribution of particle velocities, there are a reasonable number of such particles in the tail of the distribution. However, for electrons, the gyroradius (which is directly proportional to the particle mass) is much smaller. Thus, electrons would need an energy boost from elsewhere to be able to initially cross the shock instead of simply being swept along with it. We observe X-rays and gamma rays from populations of accelerated electrons in the vicinity of SNRs (Section 2.2.1 of this chapter will discuss these observations), so there must be a solution to the injection problem, but for now the mechanism for the initial acceleration of electrons remains a mystery.

There has been some additional criticism of SNRs as the acceleration site of CRs generally. The low anisotropy of Galactic CRs would argue against individual

SNRs as the origin. High energy Galactic CRs diffuse out of the Galaxy quickly, and if individual SNRs were the only source of these particles, one would expect greater anisotropy would be observed (see [39], [38] and references therein for more detailed discussion). In recent years, however, evidence of such anisotropy has begun to emerge. Milagro [45] [46], IceTop [47], and ARGO-YBJ [48] (and earlier references therein) have all reported statistically significant anisotropies in the observed CR flux of fractional amplitude $\sim 10^{-3}$ at angular size scales ranging from $\sim 10^{\circ}$ to $\sim 30^{\circ}$. Excesses and deficits are each observed.

Although NLDSA in SNR shocks remains the strongest-supported idea for Galactic CR acceleration, there are other problems with it that are yet to be solved, and hence some competing theories. A detailed study of CR propagation and composition in the galaxy done by Strong, Moskalenko, and Ptuskin in 2007 found that the expected source spectrum should be closer to -2.35 than -2.0 [49]. More generally, the smooth junction of Galactic and extragalactic spectra at the "knee" of the CR spectrum is considered by some to be highly unlikely if these components truly are from two different populations of parent particles [38]. One can also consider the fact that isolated SNRs are rare, and most SNRs exist in superbubbles. Superbubbles are formed when massive stars in a cluster end their short lives, leaving multiple interacting SNRs in close proximity. If we assume that shocks in superbubbles behave similarly to individual SNR shocks, this is not a problem, but such an assumption is not necessarily valid; interacting shocks forming a superbubble present a far more complex environment than an individual SNR might encounter [39]. Although these problems are not addressed by NLDSA, no better coherent theory has yet garnered much supporting evidence, and so NLDSA remains the favored explanation for accelerating Galactic CRs.

2.2 Observational Evidence

While it is encouraging that NLDSA solves most of the theoretical problems with DSA, its predictions must still be confirmed by observational evidence. There is a

growing body of such evidence supporting the idea that SNRs may be the main accelerators of the Galactic CR population. Since the CR particles we are considering are relativistic, they produce non-thermal radiation (as opposed to the thermal blackbody radiation produced by all matter). This non-thermal radiation is most often observed in the radio, X-ray and gamma-ray portions of the electromagnetic spectrum, so I will mainly discuss observations in these wavebands.

2.2.1 Evidence of Accelerated Electrons and Unidentified Parent Particles

While the presence of CR electrons does not also prove the presence of CR ions, it would be evidence against DSA if electrons were not also accelerated by the same process. Indeed, there exists a body of observations which support the idea that electrons are being accelerated to energies near the "knee" in SNRs. In other observations, particularly gamma-ray observations, it is often difficult to firmly identify whether the parent particle population responsible for the emission is hadronic or leptonic; however, a growing number of observations do confirm that particles are being accelerated to energies near the "knee".

X-ray observations of several SNRs reveal bright, non-thermal emission with a featureless spectrum around the rim of the SNR. This emission is synchrotron radiation produced by highly energetic electrons accelerated in strong magnetic fields near the shock front (see, e.g., [50]). Synchrotron radiation occurs when a charged particle is accelerated radially (spirals) around a magnetic field line. While synchrotron radiation is produced in radio through X-ray wavebands, we can relate the energy of the observed synchrotron photons to the energy of the electrons that produced them with the following expression [51]:

$$E_{ph} \approx 4 \text{ keV} \times \frac{B}{1 \text{ mG}} \times \left(\frac{E_e}{10 \text{ TeV}}\right)^2$$

For hard X-ray photons in a magnetic field of a few μ-Gauss this corresponds to electrons with energies in the hundreds of TeV, comparable to energies near the "knee" in

the spectrum of CR nuclei.

The first firm identification of synchrotron radiation from relativistic electrons at a SNR shock front was in the remnant of SN 1006 in 1995 [51]. Since then, synchrotron emission has been observed in other young SNRs, including Cassiopeia A [52], Vela Jr. (also known as RX J0852.0-4622 or G266.6-1.2) [53], RX J1713.7-3946 (also known as G347.3-0.5) [54][55], G1.9+0.3 [56], G 330.2+1.0 [57], and G347.3-0.5 [58]. This list is quickly growing, suggesting that efficient acceleration of electrons in young SNRs may be common.

The H.E.S.S. Cherenkov telescope in Namibia, which will be described in more detail in Chapter 4, Section 4.1.2, observed RX J1713.7-3946. The H.E.S.S. collaboration published results from a data set comprised of 91.3 hours of observations spanning 3 years. The measured spectral energy distribution spans from ∼300 GeV to over 100 TeV [59][60]. Although the H.E.S.S. data are inconclusive with regards to the nature of the parent particle population, they do show that particles are being accelerated to at least 100 TeV (10^{14} eV) in the shell of this remnant. Later, the *Fermi*-LAT collaboration published a detection of RX J1713.7-3946 at MeV-GeV energies [61]. In 2 years of observations, they measured a power-law spectrum between 500 MeV and 400 GeV with a very hard index of $1.5 \pm 0.1_{stat} \pm 0.1_{sys}$. The normalization smoothly connects with the H.E.S.S. spectrum, and they find that the spectral shape and index are in agreement with models of emission due to inverse Compton scattering of electrons. The morphology of the emission is such that the brightest areas in X-rays, MeV-GeV gamma rays, and TeV gamma rays overlap, indicating that the nonthermal emission seen over these broad wavebands is likely due to the same population of accelerated particles (see Figure 2.3 for the skymap and spectral energy distribution). They note that gamma-ray emission with a probable leptonic origin does not signify a lack of accelerated protons in the shell of this remnant, but merely indicates that the ambient matter density is too low for any protons present to produce significant gamma-ray emission. Despite the *Fermi*-LAT collaboration's favoring of a leptonic

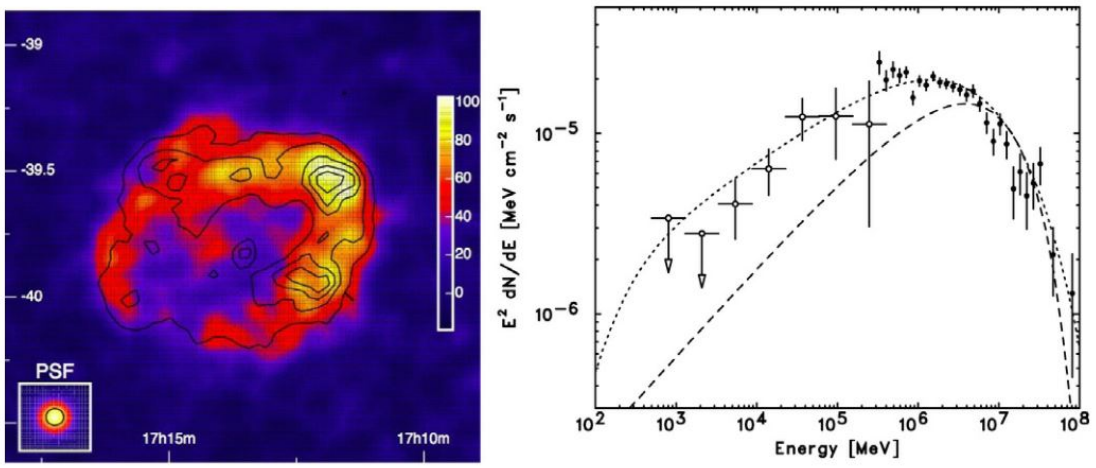

Figure 2.3: Figure 3 from [62]. "Spatial and spectral characteristics of RX J1713.7-3946. (a) (Left panel): The X- and VHE γ-ray images of RX J1713.7-3946 obtained with the ASCA and H.E.S.S. telescope array, respectively (from [59]). (b) (Right panel): The spectral energy distribution of RX J1713.7-3946 based on the Fermi [61] and H.E.S.S. [59] data." Also shown on the spectral energy distribution are models of inverse Compton emission (dotted line) and π^0-decay emission (dashed line).

model to explain the observed MeV-TeV spectrum, Aharonian considers several plausible scenarios in which protons could produce the observed spectrum [62]. Further observations with future instruments having better angular resolution would be able to distinguish between some of these scenarios.

H.E.S.S. also observed the SNR W28 for a total of ∼42 hours over three years, resulting in a detection of four distinct sources of TeV gamma rays in the vicinity ([63], and references therein). W28 is an older SNR, with an age between 35,000 and 150,000 years. Its age makes it likely, though not certain, that any electrons it has accelerated have since lost energy through radiative cooling, and are not capable of producing TeV gamma-ray emission. Furthermore, W28 is interacting with a molecular cloud along its northern and northeastern boundaries. The interaction has been confirmed by the presence of 1720 MHz OH masers, as well as the presence of high-density shocked gas. As mentioned briefly in Chapter 1, molecular clouds (MCs) provide a denser target

material than the interstellar medium for accelerated protons to interact with, generating π^0, which decay into gamma rays (this process will be discussed in greater detail in Chapter 3, Section 3.1.2). The detection of a cluster of gamma-ray sources in the region is likely due to the slow diffusion of CR protons into the adjacent MC. However, at this time electrons cannot be ruled out as the source of the gamma-ray emission via inverse Compton scattering and/or bremsstrahlung; detailed measurements of non-thermal X-ray emission and local magnetic fields would be required to make this distinction. Furthermore, even if the emission could be identified as resulting from hadrons, there are three other SNRs in the H.E.S.S. field of view. One of these is located adjacent to the TeV emission at the northeastern boundary of W28. Another lies $\sim 0.5^\circ$ north of the TeV emission at the northeastern boundary. The third has positional overlap with one of the other detected TeV sources. Ambiguities about the distances to these remnants and to the MC leave open the possibility that some other scenario is responsible for the observed TeV emission.

Tycho's SNR is another remnant which has produced evidence of particle acceleration to energies near the "knee" of the CR spectrum. A 2005 analysis of *Chandra* data by Warren et al. [64] measured the azimuthal-angle-averaged radii of the blast wave[2], contact discontinuity[3], and reverse shock[4] of the remnant using a principal component analysis[5]. They found that the ratio of the average contact discontinuity radius to the average blast wave radius was 0.93, too large to be explained by adiabatic hydrodynamic models. Instead, they interpret their observations as evidence of efficient CR acceleration at the blast wave; the increased local compression factor from CR acceleration shortens the gap between the blast wave and contact discontinuity (as

[2] also known as the forward shock

[3] the division between supernova ejecta and the interstellar medium

[4] shock sent back into the remnant interior when the blast wave initially encounters the interstellar medium

[5] a mathematical technique in which a multi-dimensional space is defined using selected data, and a new set of axes through that space is defined by minimzing the variance in the data

discussed in Section 1 of this chapter) . They also found that the morphology of the rim is not well described by models of a thermal plasma affected by an adiabatic shock, and that spectral analysis of emission at the rim points to it being mostly non-thermal synchrotron radiation.

2.2.2 Evidence of Accelerated Hadrons

More recent observations of Tycho with *Chandra* provide more direct evidence for the presence of protons accelerated up to 10^{15} eV. In 2011, Eriksen et al. [65] reported the discovery of non-thermal, X-ray bright, highly ordered stripes with spacing corresponding to the gyroradii of 10^{14} - 10^{15} eV protons (see Figure 2.4). They explain the presence of the stripes through the Bell mechanism[6], but note that current models cannot explain the regular ordering of the stripes.

Recall again that MCs provide target material for accelerated protons to collide with, producing π^0, which decay into gamma rays. Neutral pion decay will be discussed in greater detail in Chapter 3, Section 3.1.2, but it is important for the following discussion to note that the gamma-ray number spectrum, $F(\epsilon)$, of photons produced by this process is symmetric about ∼70 MeV when displayed in a log-log format. This "70 MeV bump" is a signature of neutral pion decay. Thus, observations at energies below 100 MeV are crucial for firmly identifying π^0-decay gamma rays.

In February 2013, the *Fermi*-LAT collaboration published the first detection of firmly identifiable gamma-ray emission from CR protons in two SNRs, IC 443 and W44 [67]. *Fermi*-LAT is a satellite-based telescope sensitive to gamma rays between 20 MeV and 300 GeV; the instrument will be discussed in greater detail in Chapter 4, Section 4.2. IC 443 and W44 are both middle-aged (∼10,000 years old) remnants interacting with MCs.

After four years of observations, statistics at the lower end of *Fermi*'s energy sensitivity were sufficient to determine significant spectral data points below 200 MeV. Spectra were generated for photons with reconstructed energies between 60 MeV and

[6] amplification of the magnetic field through turbulence caused by CRs [66]

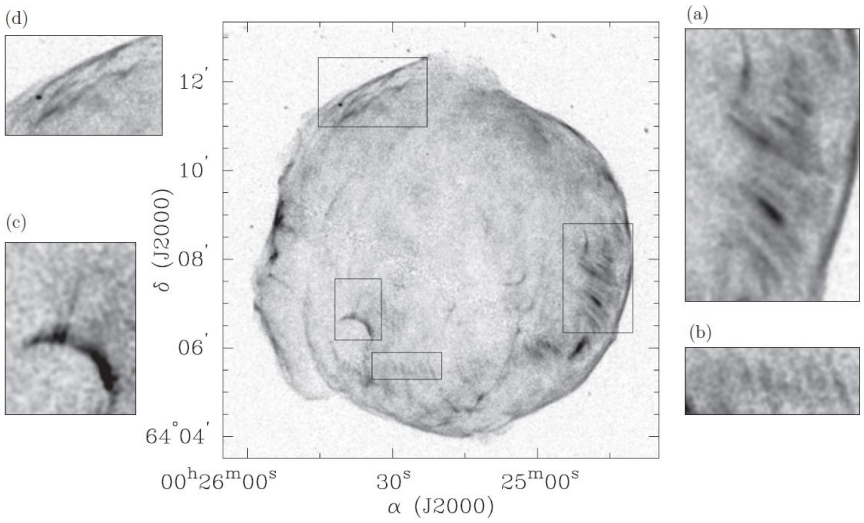

Figure 2.4: Figure 1 from [65]. ©AAS. Reproduced with permission. "*Chandra* X-ray 4.0 - 6.0 keV image of the *Tycho* supernova remnant, smoothed with a $\sim 0''.75$ Gaussian and displayed with an *arcsinh* scaling, showing various regions of striping in nonthermal emission. Clockwise from the upper right: (a) the main western stripes discussed in [65]; (b) a fainter ensemble of stripes; (c) a previously known bright arc of nonthermal emission, with newly discovered streamers; and (d) filaments of 'rippled sheet' morphology common in optical observations of middle-aged SNRs."

100 GeV from each remnant. The results, spectra well-fit by smoothly broken power-laws, are shown in Figure 2.5. Models of various emission mechanisms were fit to the spectral data between 60 MeV and 2 GeV. The π^0-decay model provided the best fit, particularly in the lower energy portion of the spectrum. Models featuring accelerated electrons were ruled out; inverse-Compton scattered electrons were rejected based on energetics, and fitting bremsstrahlung emission required an additional *ad hoc* break in the electron spectrum (although the data do not rule out some small contribution to the emission from electron bremsstrahlung). Furthermore, the *Fermi*-LAT data indicate that most of the CRs producing the emission must come from downstream of the shock; if the CRs were merely distributed upstream (within $0.1R$ of the shock, where R is the SNR radius) prior to the SN explosion and interaction with the MC, the expected energy spectrum at low energies would be much harder than the observations indicate.

While firm identification of accelerated protons in two SNRs is not conclusive proof that the bulk of Galactic CRs are accelerated by SNRs in general, it is certainly an important and very compelling piece of evidence. Further observations of additional SNRs in the crucial 70 MeV energy range will help to determine whether acceleration of protons in SNR shocks is common. This information can, in combination with higher energy data, determine whether these accelerated protons reach energies at, or even beyond, the "knee" in the CR spectrum.

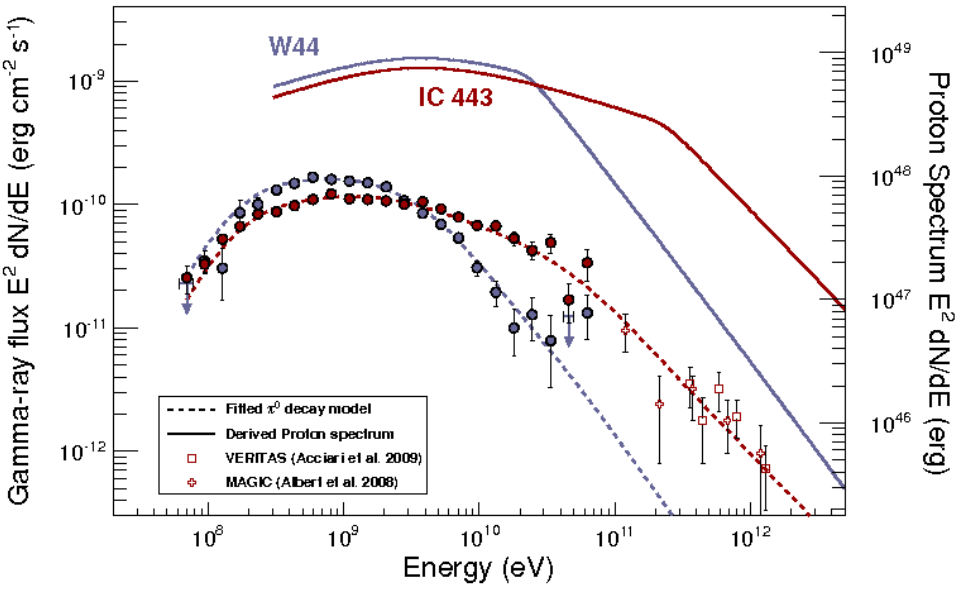

Figure 2.5: Figure 3 from [67]. "Proton and gamma-ray spectra determined for IC 443 and W44. Also shown are the broadband spectral flux points derived in this study, along with TeV spectral data points for IC 443 from MAGIC [68] and VERITAS [69]. The curvature evident in the proton distribution at 2 GeV is a consequence of the display in energy space (rather than momentum space). Gamma-ray spectra from the protons were computed using the energy-dependent cross section parameterized by [70]. We took into account accelerated nuclei (heavier than protons) as well as nuclei in the target gas by applying an enhancement factor of 1.85 [71]. Note that models of the gamma-ray production via *pp* interactions have some uncertainty. Relative to the model adopted here, an alternative model of [72] predicts 30% less photon flux near 70 MeV; the two models agree with each other to better than 15% above 200 MeV. The proton spectra assume average gas densities of $n = 20$ cm^{-3} (IC 443) and $n = 100$ cm^{-3} (W44) and distances of 1.5 kpc (IC 443) and 2.9 kpc (W44)."

Chapter 3

TEV GAMMA-RAY ASTRONOMY

3.1 Very High Energy Gamma-Ray Production in Astrophysical Sources

Gamma rays are the highest energy photons. Although the term "gamma ray" is not strictly defined, it is generally used to describe photons with energies above ∼100 keV. This regime is further divided into medium energy gamma rays (∼100 keV to 30 MeV), high energy (HE) gamma rays (∼30 MeV to 100 GeV), very high energy (VHE) gamma rays (∼100 GeV to 100 TeV), and ultra high evergy gamma rays (above ∼100 TeV) [73]. Gamma rays comprise over 10 decades in energy, which is as much as the rest of the electromagnetic spectrum combined. Note also that the divisions within the gamma-ray portion of the spectrum are somewhat arbirtary and are not stringent; other sources may define them slightly differently. The divisions are based as much on the physics of current detectors as they are on the physics of gamma-ray production. This thesis will focus mainly on VHE gamma rays, with some discussion of HE gamma rays. Earth's atmosphere is opaque to gamma rays, so direct observation of these photons must be done from space. However, through indirect means, VHE gamma rays can be detected from ground level. This process will be discussed more in Section 3.3 of this chapter, and the detectors will be described in detail in Chapter 4.

VHE gamma rays can only be produced through non-thermal processes. In other words, they are produced by populations of accelerated particles with a non-Maxwellian distribution of velocities. In the environments present in SNRs, there are three main modes of production: accelerated leptons undergoing inverse Compton scattering, accelerated hadrons interacting with target material to produce neutral pions, and bremsstrahlung.

3.1.1 Leptonic Gamma-Ray Production

3.1.1.1 Inverse Compton Scattering

VHE gamma rays are produced when relativistic electrons interact with an ambient photon field. Often, this is the cosmic microwave background, but starlight or other local photons produced by a given source can also serve. An energetic electron collides with a low-energy photon and transfers some of its energy to the photon, upscattering it to the VHE regime. This process is called inverse Compton (IC) scattering, since it is the inverse of the Compton scattering process through which high-energy photons interact with matter and transfer some of their energy to the constituent electrons, which then escape the target material. For photons with an initial energy E_o undergoing IC scattering, the average final energy will be $E = \frac{4}{3}\gamma^2 E_o$, where $\gamma = \frac{1}{\sqrt{1-(\frac{v}{c})^2}}$ (see, e.g., [74]).

3.1.1.2 Bremsstrahlung

Electrons accelerating in an electrostatic field produce "braking radiation," more commonly referred to by its German name, bremsstrahlung. The electrostatic fields are produced by the ions and nuclei that compose the material through which the electron is traveling. In an astrophysical context, this process is notable because electrons with a power-law energy spectrum undergoing bremsstrahlung will produce gamma rays with a power-law spectrum of the same spectral index [74].

3.1.2 Hadronic Gamma-Ray Production

Populations of accelerated hadrons (mainly protons) can also lead to the production of VHE gamma rays. When accelerated protons collide with other protons or nucleons in the ambient medium, they produce a collection of secondary particles including kaons, hyperons, and pions. If the kinetic energy of the originating proton is sufficient ($\approx$ 280 MeV), a neutral pion, π^0, can be produced. This π^0 decays very quickly into two gamma rays. The mean lifetime of a π^0 is 8.4×10^{-17} s [74].

Gamma radiation of this type is more likely to occur with a dense medium present to interact with (e.g., a molecular cloud). A signature of π^0-decay gamma rays is a maximum in the gamma-ray number spectrum occuring at $\frac{m_{\pi^0}c^2}{2} \simeq 67.5$ MeV [67]. This "70 MeV bump" occurs regardless of the energy distribution of the parent particle population [74].

3.2 Gamma-Ray Absorption in Space

Once a gamma-ray photon is created in an astrophysical source, it must travel through space to Earth before we can observe it. On its journey, there is some chance it will be absorbed through one of several processes. The most likely cause for absorption is photon-photon pair production. This occurs when a high energy photon collides with a lower energy photon and the center-of-mass energy of the photons is greater than twice the rest energy of the electron, squared. The two photons will annihilate, producing an electron-positron pair:

$$\gamma + \gamma \rightarrow e^+ + e^-$$

The cross-section of this process reaches a maximum when

$$E_\gamma h\nu(1 - cos\theta) \simeq 2(m_e c^2)^2$$

where E_γ is the energy of the higher energy photon, $h\nu$ is the energy of the lower energy photon, θ is the collision angle between the two photons' paths, and $m_e c^2$ is the rest energy of the electron [73].

Thus, different energy gamma rays will interact most strongly with different lower-energy photon fields. For a 1 TeV gamma ray, the maximum interaction will occur with photons of energy 0.5 eV ($\lambda = 2\mu$m) [73]. These photons fall into the near infrared (IR) portion of the electromagnetic spectrum. For pair production to cause significant absorption of gamma rays, the lower energy photon field must be fairly dense. Within the Galaxy there is no lack of stars, gas and dust to produce infrared

light, so its effect must be considered. Often it is negligible, if no strong source of photons of the appropriate energy lies between Earth and the gamma-ray source under consideration. When studying extragalactic sources, the greater distances involved make it more likely that a gamma-ray photon will encounter a lower-energy photon of the appropriate energy, so again, absorption must be considered. The study of the density of these photon fields in intergalactic space, generally known as extragalactic background light (EBL), is one of the areas of active research in VHE astronomy. Generally, pair production off EBL constrains VHE observations to targets with a redshift $z \lesssim 0.5$ [75].

In recent years, the first measurements of the EBL through studies of the gamma-ray spectra of blazars have been made (see Section 3.4.2.1 of this chapter for a detailed discussion of blazars). If no intrinsic break in the spectrum is assumed for blazars with $z \gtrsim 0.5$, then any attenuation of the flux from the source due to EBL can be detected as an "imprint" on the spectrum. The specific imprint is dependent on both energy and redshift, and many models exist to describe it (see, e.g., [76], [77] and references therein). In 2012, *Fermi*-LAT data between 1 and 500 GeV on 150 BL Lacertae-type blazars were used to derive the optical depth of EBL photons in the optical to ultraviolet (UV) range [76]. They found that, for $z \simeq 1$, the flux density of the UV EBL component is 3 ± 1 nW m^{-2} sr^{-1}. This result is in agreement with the estimate from galaxies individually resolved by the Hubble Space Telescope, and with the estimate of the average UV background from the proximity effect in quasar spectra (see [76] and references therein for details). In 2013, the H.E.S.S. collaboration published a study of the spectra between $\sim$ 100 GeV and 50 TeV of the seven brightest blazars they had detected [77]. In these spectra, they detect the imprint of the EBL at a statistical significance of 8.8σ, where σ is one standard deviation. They were able to study the EBL flux density between 0.3μm and 17μm (optical to IR wavelengths), and found a peak in the amplitude at 1.4μm. At that point, the EBL flux density was measured to be $15 \pm 2_{stat} \pm 3_{sys}$ nW m^{-2} sr^{-1} (see Figure 3.1).

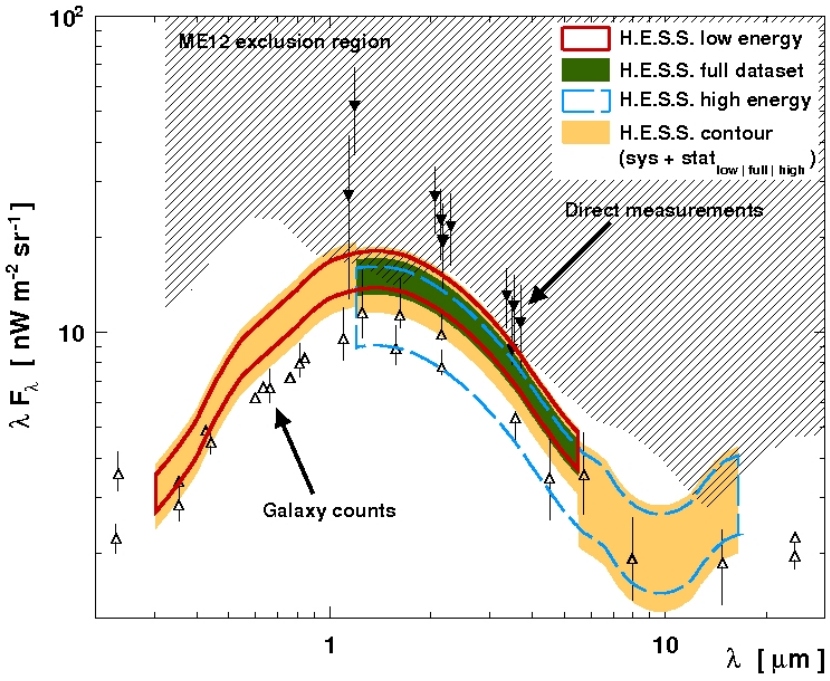

Figure 3.1: Figure 5 from [77]. Reproduced with permission ©ESO. "Flux density of the extragalactic background light versus wavelength. The 1σ (statistical) contours derived for several energy ranges are described in the top-right legend. The systematic uncertainty is added quadratically to the statistical one to derive the H.E.S.S. contour. Lower limits based on galaxy counts and direct measurements are repsectively shown with empty upward and filled downward poiting triangles (extracted from [78]). The region excluded by Meyer et al. [79] with VHE spectra is represented by the dashed area."

It is also possible for gamma rays to be absorbed through interactions with matter. In both interstellar and intergalactic space, the density of atoms is low enough that gamma-ray absorption through this mechanism is unlikely. However, in environments near to a source, the density of matter may be much greater, and this absorption can have an effect on the flux of gamma rays observed.

3.3 Atmospheric Air Showers & Cherenkov Radiation

Once gamma rays are produced by populations of accelerated, charged particles, they travel through space in straight lines. This is because, unlike the parent particles, the photons themselves are unaffected by interactions with magnetic fields in space. Thus, while populations of cosmic rays (CRs) cannot be directly observed to come from a given source, the gamma rays they produce can point the way to their sources.

Once they reach Earth, gamma rays and CRs alike decay upon interaction with Earth's atmosphere, producing a shower of secondary particles and photons. The details of the air showers produced by these two sources will be discussed below. In each case, Cherenkov radiation is produced by the air shower. Cerenkov radiation is produced by charged particles traveling faster than the speed of light within a medium (a velocity still less than c). As the charged particles pass through the medium, they polarize the surrounding molecules that comprise the medium, which then emit a brief electromagnetic pulse. These pulses interfere constructively to form a coherent wavefront, seen as a Cherenkov photon (see, e.g., [80]). This process is analogous to the shock wave produced by an object traveling faster than the speed of sound in a medium. The direction of travel of the photon with respect to the direction of travel of the originating charged particle is given by $\cos\theta = \frac{1}{\beta n}$, where $\beta = \frac{v}{c}$, v is the velocity of the originating particle, and n is the refractive index of the medium. In air, $n = 1.00029$ at sea level, and $\theta \simeq 1.3°$ [80]. These photons produce a spectrum which peaks between 300 and 500 nm, in the blue to ultraviolet portion of the electromagnetic spectrum [74].

This Cherenkov radiation is what is actually observed from the ground. From properties of the images taken of the air showers, gamma-ray-induced air showers can be separated from CR-induced air showers (see, e.g., [81]). Then, for the gamma-ray initiated showers, the energy and path of the initial gamma ray can be reconstructed. The detectors used to observe the Cherenkov radiation will be described in detail in Chapter 4, and the process of analyzing the resultant images will be discussed in detail in Chapter 5.

3.3.1 Gamma Ray Air Showers

After entering the atmosphere, a gamma ray proceeds, on average, for one radiation length before interacting with an atmospheric nucleus. A radiation length is defined as the distance in a given medium over which an electron loses $\frac{1}{e}$ of its energy through radiation. This can be calculated from the following formula [80]:

$$\frac{1}{X_o} = 4\alpha\left(\frac{N}{A}\right)Z^2{r_e}^2 ln(183Z^{-\frac{1}{3}})$$

where α is the fine structure constant, N is Avogadro's number, A is the atomic weight of the substance comprising the medium, Z is the atomic number of the substance comprising the medium, and r_e is the classical electron radius. For a medium comprised of several substances, the effective radiation length can be computed as follows [80]:

$$\frac{1}{X_{eff}} = \frac{p_1}{X_1} + \frac{p_2}{X_2} + ...$$

where p_1, p_2, etc. are the fractions by weight of each element in the medium.

In Earth's atmosphere, a radiation length is 37.1 g/cm^2, and the first interaction occurs at an altitude of ∼20 km [73]. This interaction results in the production of an electron/positron pair, with each particle having half the energy of the initial gamma ray. In general, the energy of a particle within the air shower is given by $E = \frac{E_o}{2^n}$, where E_o is the energy of the initial photon and n is the number of radiation lengths the shower has traversed [80]. Note that these electrons and positrons are traveling faster than

the local speed of light, and so are emitting Cherenkov radiation. The electron and positron will each undergo bremsstrahlung, and after another radiation length will emit a secondary gamma-ray photon, which then after another radiation length produces another electron/positron pair, and so on (see Figure 3.2). This process continues until the average energy of the shower particles reaches a critical value, defined as the point at which ionization losses equal radiative losses. The energy at which this occurs is referred to as the *critical energy*, and can be approximated by the following expression [82]: $E_{crit} = \frac{800MeV}{Z+1.2}$, where Z is the atomic number of the medium under consideration. For nitrogen (Z = 7), which composes most of Earth's atmosphere, this is ∼98 MeV. The point where the critical energy is reached is known as the shower maximum, and represents the point at which the number of particles in the shower has reached its maximum. After this point, the number of particles in the shower decreases, and hence so does the amount of Cherenkov light emitted by the particles. Therefore, it is beneficial to position one's detector as close to shower maximum altitude as possible, to maximize the number of Cherenkov photons available to detect (although ideally, the entire shower would be observable for purposes of shower reconstruction). The precise altitude of shower maximum depends on the energy of the initial gamma ray; see Table 3.1 for a selection of energies and their assorted parameters.

As an air shower travels through the atmosphere, the Cherenkov angle broadens slightly with decreasing altitude. This is due to small changes in the refractive index of air, n, with changes in atmospheric density. Because of this effect, the light from the shower is focused on the ground to form an annulus of radius ∼120 m. Additionally, the light from the top of the shower arrives on the ground at the same time (within ∼1 ns) as the light from the bottom of the shower. This is because the photons are moving through the atmosphere with speed c/n (slightly slower than c), while the particles are moving with a speed closer to c. Thus, the time it takes for a photon from higher up in the shower to reach the ground is equal to the time it takes for a particle to travel to a point lower in the shower and decay, plus the time it takes for the resulting lower photon to reach the ground. The particle and photon generated

Energy, E_γ	X_{max}, g cm^{-2}	h_{max}, km	N_{max}	N_{sl}	N_{mt}	ρ_{sl}, photon m^{-2}	ρ_{mt}, photon m^{-2}
10 GeV	175	12.8	1.6×10^1	4×10^{-4}	2×10^{-2}	2.7×10^{-1}	3.6×10^{-1}
100 GeV	261	10.3	1.3×10^2	4.0×10^{-2}	1.4×10^0	4.6×10^0	7.6×10^0
1 TeV	346	8.4	1.1×10^3	3×10^0	6.0×10^1	7.4×10^1	1.3×10^2
10 TeV	431	6.8	1.0×10^4	1.3×10^2	1.7×10^3	1.1×10^3	1.7×10^3
100 TeV	517	5.5	9.3×10^4	4.5×10^3	3.6×10^4	1.6×10^4	1.9×10^4
1 PeV	602	4.4	8.6×10^5	1.15×10^5	5.7×10^5	1.9×10^5	1.9×10^5

Table 3.1: Gamma-ray shower parameters as a function of energy, from [73], who acknowledges simulations by A.M. Hillas. X_{max} is the maximum shower thickness traversed, h_{max} is the altitude of shower maximum, N_{max} is the maximum number of electrons, N_{sl} is the number of surviving particles at sea level, N_{mt} is the number of surviving particles at mountain altitude (2.3 km), ρ_{sl} is the density of Cherenkov photons at sea level, and ρ_{mt} is the density of Cherenkov photons at mountain altitude.

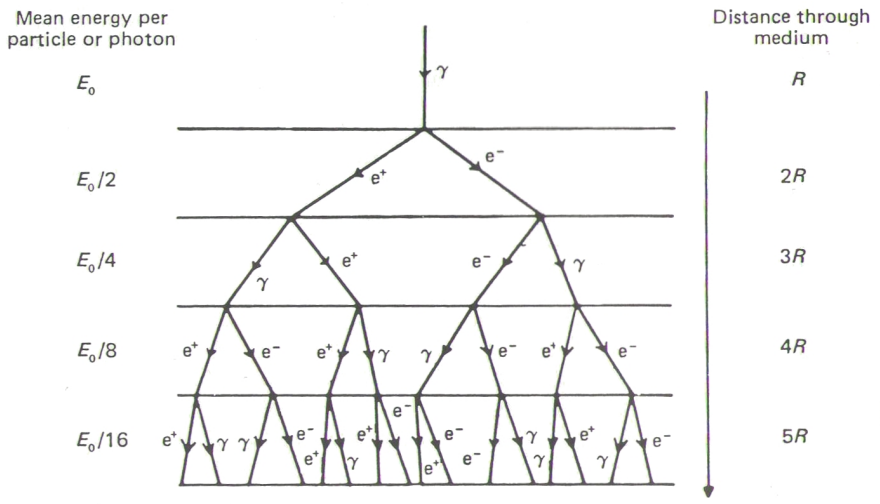

Figure 3.2: Figure 4.17 from [83]. ©2011 Malcolm S. Longair. Reprinted with the permission of Cambridge University Press. "A simple model for an electromagnetic shower." Here, R is a radiation length, and E_o is again the energy of the initial photon.

lower in the shower have a longer geometric path to travel to reach the same point, but the particle's greater speed makes up the difference in time [73].

3.3.2 Cosmic Ray Air Showers

Air showers are also produced by CRs entering Earth's atmosphere. In these showers, the primary particle again interacts with an atmospheric nucleus, this time producing a hadronic shower consisting of secondary nucleons, kaons, and pions. This process is known as *pionization*. The nucleonic cascade forms the core of the hadronic shower, and the resultant particles continue to interact and produce further particles until the average energy per particle is less than ∼1 GeV, which is insufficient to produce multiple pions [83]. An illustration of a hadronic air shower is shown in Figure 3.3.

The pions themselves that are created by this process undergo their own development, leading to electromagnetic cascades like those described in the previous section. Neutral pions (π^0) decay directly to gamma rays, as discussed in Section 3.1.2

of this chapter. These gamma rays go on to produce electromagnetic cascades with accompanying Cherenkov radiation. Charged pions decay into charged muons and muon neutrinos in the following reactions, with a mean lifetime of 2.551×10^{-8} s [83]:

$$\pi^+ \rightarrow \mu^+ + \nu_\mu$$

$$\pi^- \rightarrow \mu^- + \bar{\nu}_\mu$$

While high energy muons can reach the surface of the Earth because of time dilation, low energy muons have enough time in flight to decay into electrons and positrons, electron neutrinos, and additional muon neutrinos via the following reactions, with a mean lifetime of 2.2001×10^{-6} s [83]:

$$\mu^+ \rightarrow e^+ + \nu_e + \bar{\nu}_\mu$$

$$\mu^- \rightarrow e^- + \bar{\nu}_e + \nu_\mu$$

These electrons and positrons then produce additional electromagnetic cascades, and more Cherenkov radiation [83]. It is important to note that hadronic air showers are much less tightly focused than electromagnetic cascades, with some particles landing hundreds of meters from the shower axis. This occurs because the secondary particles that are emitted in a hadronic air shower carry momentum in directions other than the direction of travel of the shower primary [33]. Additionally, the lateral profile of the Cherenkov light emitted by the two showers has a different profile (see Figure 3.4). Because of this lateral spreading effect, it is possible to analyze the Cherenkov radiation from a given shower and determine whether its origin was due to a gamma ray or a CR. Again, the process of image analysis will be discussed in greater detail in Chapter 5.

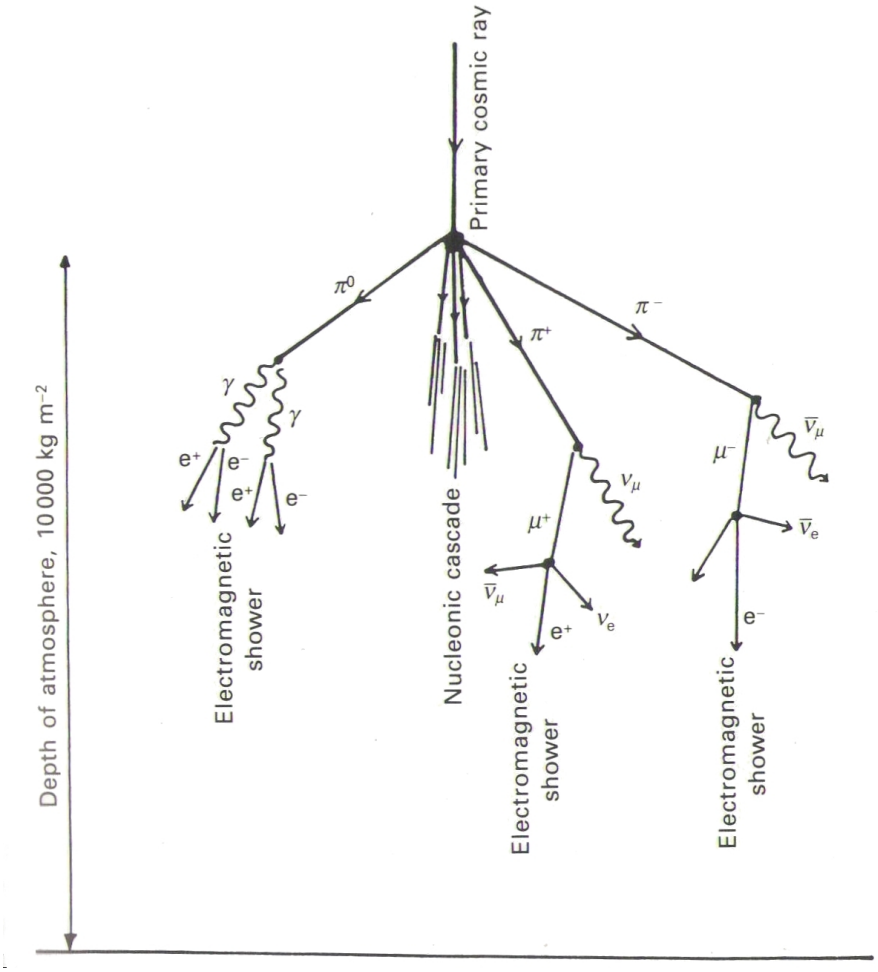

Figure 3.3: Figure 5.11 from [83]. ©2011 Malcolm S. Longair. Reprinted with the permission of Cambridge University Press. "A schematic diagram showing the development of a nucleonic cascade in the atmosphere."

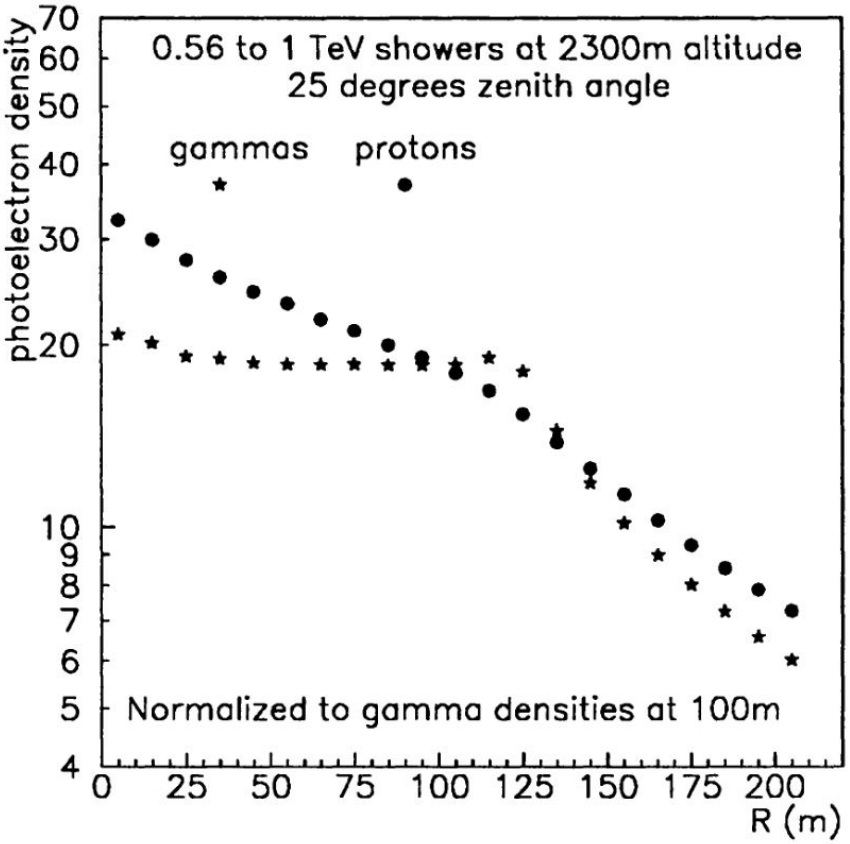

Figure 3.4: Figure 2 from [84]. "Average lateral distributions of Cherenkov light at about 700 GeV."

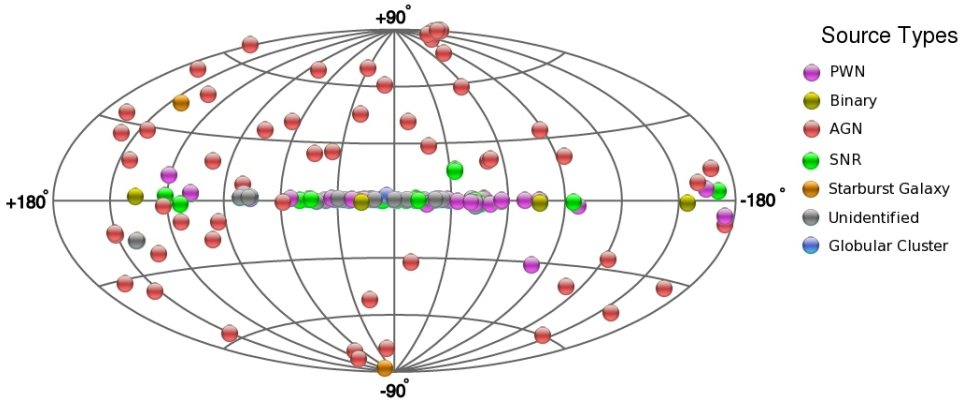

Figure 3.5: Sky map in Galactic coordinates of all currently known TeV gamma-ray sources, as provided by *TeVCat*, an online catalog of TeV gamma-ray sources [86].

3.4 TeV Source Classes

It has already been established that astrophysical gamma rays are produced by populations of accelerated particles. As such, they are emitted by the more extreme, energetic, and often violent environments in the universe. The two most common acceleration mechanisms are shock waves and jets, but other scenarios can also produce gamma-ray emission. The following discussion will divide observed and strongly suspected TeV gamma-ray source types into Galactic and extragalactic classes, with a brief discussion of the gamma-ray production mechanism for each source type. Considering that the first statistically significant detection of TeV gamma rays from an astrophysical source was in 1989 [85], this field has grown quite rapidly, especially in recent years. This is due mostly to the improvements in instrumentation, which will be discussed in Chapter 4.

3.4.1 Galactic Sources

Of the ∼150 TeV sources cataloged at the time of this writing [**?**], ∼100 of them lie along the galactic plane (see Figure 3.5). A few of these are extragalactic sources whose position happens to lie along the Galactic plane from our perspective, but the

vast majority are sources in the Milky Way.

3.4.1.1 Pulsar Wind Nebulae

The most populous class of Galactic TeV sources is pulsar wind nebulae (PWNe), sometimes referred to as plerions. Pulsars, or rapidly rotating neutron stars with strong magnetic fields, produce an ultrarelativistic outflow of electrons and positrons (see, e.g., [87] for a review). This particle wind can interact with the environment surrounding the pulsar to produce a luminous nebula, known as a PWN. Since pulsars are born in supernova explosions, some systems will show a composite structure with a SNR shell and a PWN interior, but shell-less systems are also observed. In recent years, a few PWN have been observed demonstrating bow shock morphologies as the associated pulsars travel through interstellar space at supersonic velocities [87].

The electrons and positrons comprising PWNe produce synchrotron radiation in the radio through X-ray portions of the electromagnetic spectrum [87] (see Chapter 2, Section 2.2.1 for a discussion of synchrotron radiation). This synchrotron radiation, in turn, undergoes inverse Compton scattering off the particles that produced it to emit TeV photons (see Section 3.1.1.1 of this chapter for a discussion of inverse Compton scattering). Such emission is referred to as synchrotron self-Compton (SSC) radiation. In this scenario, it is possible to model the magnetic field strength based on the observed spectral energy distribution. The Crab Nebula is the best example of clearly observed SSC radiation, with the synchrotron and inverse Compton components of the spectrum clearly identifiable (see Figure 3.6).

TeV emission has also been observed in PWNe with relatively low synchrotron luminosity. In such cases, it is thought that the TeV photons are produced by inverse Compton scattering of cosmic microwave background photons, thermal radiation from local dust, or starlight, rather than synchrotron radiation [87].

The size of the TeV nebula is often several orders of magnitude larger than the X-ray nebula of a given pulsar, and the TeV nebula typically grows with time while the X-ray nebula shrinks. This is because the electrons producing the TeV emission are

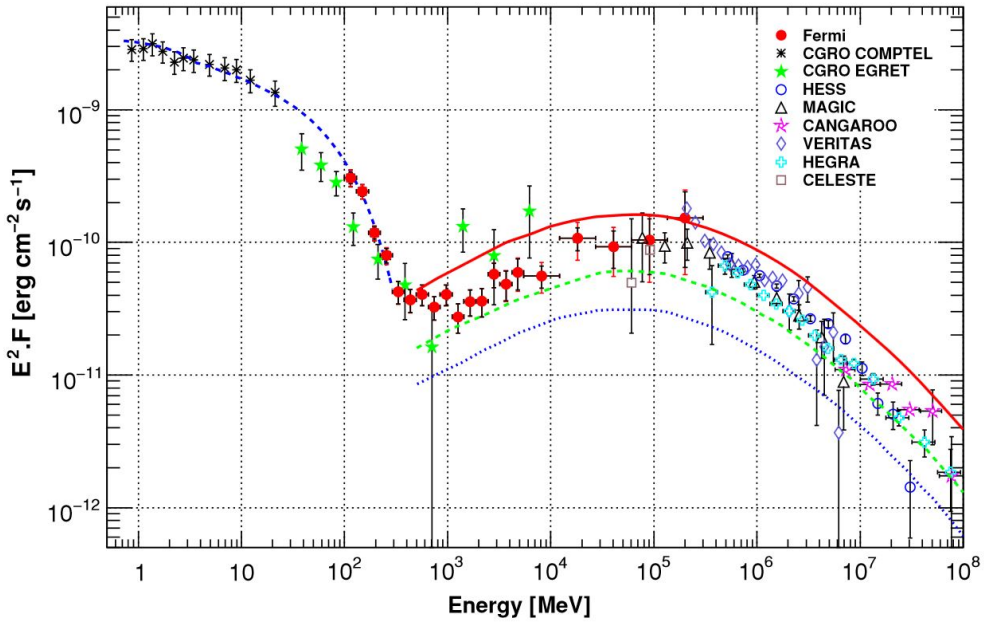

Figure 3.6: Figure 9 from [88]. ©AAS. Reproduced with permission. "Spectral energy distribution of the Crab Nebula from soft to very high energy γ-rays. The Whipple spectrum above 500 GeV [89] is also consistent with these measurements. The fit of the synchrotron component, using COMPTEL and LAT data (blue dashed line), is overlaid. The predicted IC spectra from [90] are overlaid for three different values of the mean magnetic field: 100 G (solid red line), 200 G (dashed green line), and the canonical equipartition field of the Crab Nebula 300 G (dotted blue line). References: CGRO COMPTEL and EGRET, [91]; MAGIC, [92]; H.E.S.S., [93]; CANGAROO, [94]; VERITAS, [95]; HEGRA, [96]; CELESTE, [97]."

lower energy than those producing the synchrotron emission (recall that the electrons lose energy when the synchrotron emission is produced). These lower energy electrons cool more slowly than those producing the X-ray emission, allowing the TeV nebula to continue radiating through more of the particles' lifetime than the X-ray nebula, which is produced only by newly-accelerated particles. As a result, the TeV nebula illuminates the history of particle propagation in the PWN, and the spectrum of TeV emission varies with distance from the pulsar (age of the particles) (see Figure 3.7 for an example). While many PWNe have demonstrated this effect, others, such as Vela X, show no spectral variability across the nebula, leaving open the question of the role of electron cooling in producing the observed emission [75].

3.4.1.2 Pulsars

Pulsars are rapidly rotating neutron stars. The strong magnetic field of the neutron star results in beams of radiation being produced at the magnetic poles. Often, the magnetic axis is not aligned with the axis of rotation, so as the pulsar spins the beam does also. As we observe these systems from our fixed perspective here on Earth, the beam sweeps by, similar to a beam from a lighthouse. Thus, we observe a pulse of emission with every passage of the beam.

The first detection of pulsed emission >10 GeV was in 2008. The MAGIC collaboration detected pulsed emission above 25 GeV from the pulsar in the Crab Nebula [99]. Two pulses are observed in the pulse profile: a pulse coincident with the radio ephemeris, and a stronger interpulse occurring at phase ∼0.3. Initially, the VHE spectral measurements were consistent with an exponential cutoff, as expected in models of curvature radiation. However, subsequent observations by VERITAS [100] and MAGIC [101] [102] observe emission above 100 GeV, ruling out the possibility of an exponential cutoff, and MAGIC has also detected statistically significant "bridge" emission between the pulse and the interpulse [103]. *Fermi*-LAT has also detected pulsed emission from the Crab pulsar, with a spectral break occurring at ∼6 GeV [88]. Figure 3.8 shows the combined *Fermi*-LAT and VERITAS/MAGIC spectral points.

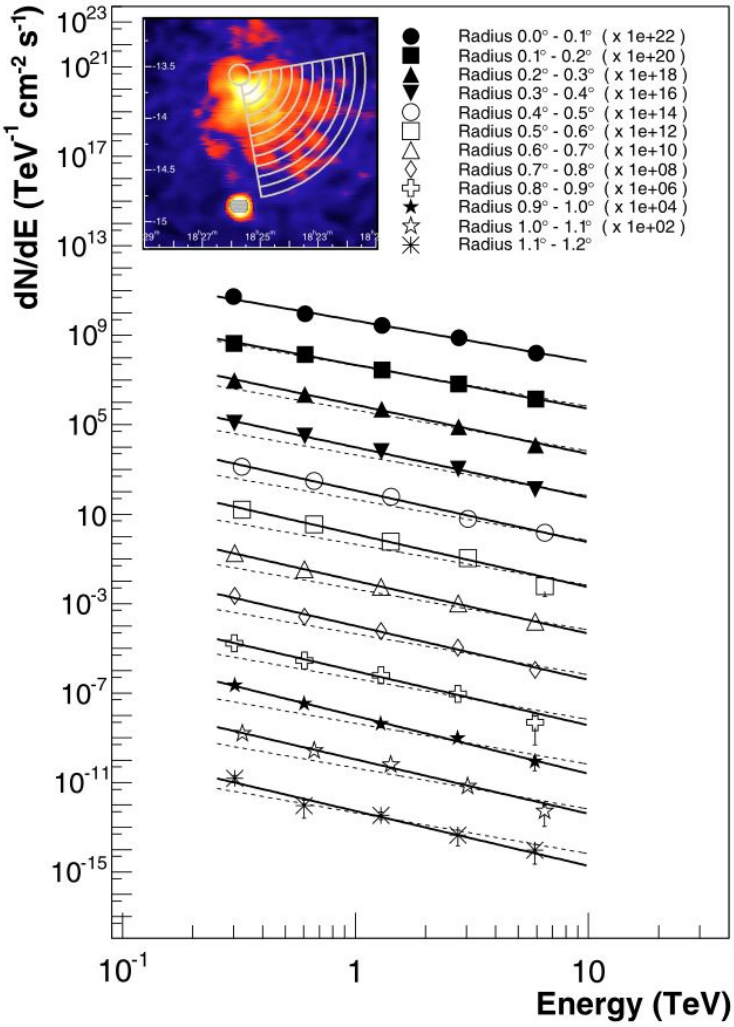

Figure 3.7: Figure 4 from [98], illustrating the energy-dependent morphology seen in H.E.S.S. PWN J1825-137. Reproduced with permission ©ESO. "Energy spectra in radial bins. Inset: H.E.S.S. excess map as shown in Figure 1 [of [98]]. The wedges show the radial regions with radii in steps of 0.1° in which the energy spectra were determined. The innermost region is centered on the pulsar PSR J1826-1334. Main figure: differential energy spectra for the regions illustrated in the inset, scaled by powers of 10 for the purpose of viewing. The spectrum for the analysis at the pulsar position is shown as a reference along with the other spectra as dashed line. For all regions the energy spectrum has been determined as described in [[98]] and has been fitted by a power-law in a restricted energy range between 0.25 and 10 TeV."

Currently, there is no satisfactory explanation for the VHE emission. Opacity requires that the VHE emission is produced much further from the pulsar than models can explain, and the observed MeV-GeV cutoff with no evidence of a TeV cutoff suggests the possibility that two different mechanisms may be responsible for the emission in the two energy bands [75].

Thanks mainly to *Fermi*-LAT, there is also a growing population of radio-quiet, gamma-ray-emitting pulsars (see, e.g., [104]). While radio-quiet pulsars were known before *Fermi*, the mission has greatly increased the known population. These pulsars are firmly identifiable in HE gamma rays, but are dark in other portions of the electromagnetic spectrum. The mechanism responsible for this pattern of emission is still unknown.

3.4.1.3 Supernova Remnants

When a star's life ends in a massive explosion referred to as a supernova, it leaves behind a rapidly expanding cloud of the gas and dust that composed the star. This is called a supernova remnant (SNR). The most noteworthy feature of SNRs is the shock wave which expands into the surrounding environment ahead of the gas and dust. The specific morphology of a SNR depends on the progenitor star and the surrounding environment, but generally there are shell-type SNRs, which exhibit a bright X-ray shell and fainter interior emission, and composite SNRs, which both exhibit a shell and contain within them a PWN.

Since the 1930s, SNRs have been thought to be the most likely source of the Galactic CR population [36] (see Chapter 2, Section 2.1 for a detailed discussion of this topic). It is thought that particles are accelerated via multiple crossings of the SNR shock front, a process known as diffusive shock acceleration. If this is true, gamma-ray emission from the interaction of accelerated hadrons (CRs) with molecules in the surrounding environment, leading to π^0 decay, should be visible from many SNRs. However, it has been difficult to definitively determine this; while many SNRs are gamma-ray sources, there are very few where the emission can be firmly identified as

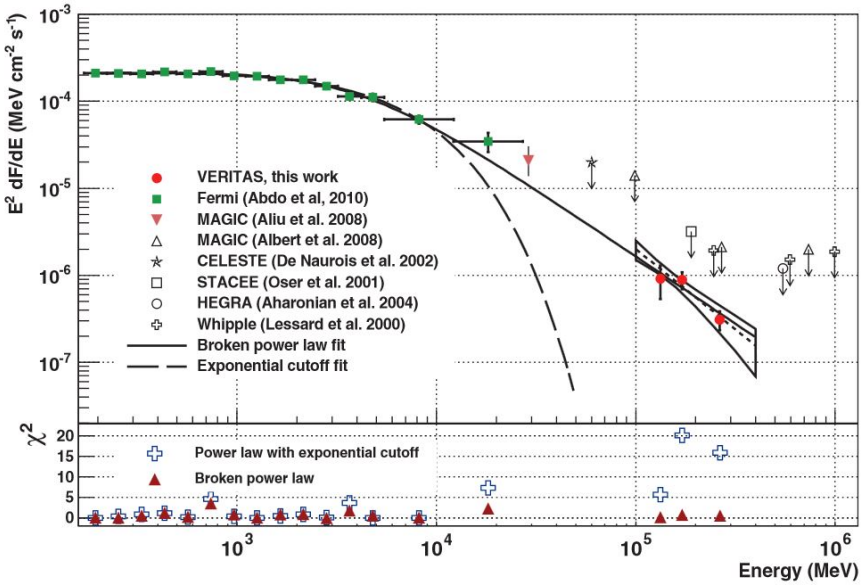

Figure 3.8: Figure 2 from [100]. "Spectral energy distribution (SED) of the Crab pulsar in gamma rays. VERITAS flux measurements are shown by the bowtie. The dotted line enclosed by the bow tie gives the best-fit power-law spectrum and the statistical uncertainties, respectively, for the VERITAS data using a forward-folding method. The solid red circles show VERITAS flux measurements using a different spectral reconstruction method (SOM). Fermi-LAT data [88] are given by green sqaures, and the MAGIC flux point [99] by the solid reddish triangle. The open symbols are upper limits from the CErenkov Low-Energy Sampling and Timing Experiment (CELESTE) [105], the High-Energy-Gamma-Ray Astronomy (HEGRA) experiment [96], MAGIC [92], Solar Tower Atmospheric Cherenkov Effect Expermient (STACEE) [106], and Whipple [107]. The result of a fit of the VERITAS and Fermi-LAT data with a broken power law is given by the solid line, and the result of a fit with a power-law spectrum multiplied with an exponential cutoff is given by the dashed line. Below the SED, we plot χ^2 values to visualize the deviations of the best-fit parameterization from the Fermi-LAT and VERITAS flux measurements."

hadronic in origin. More often, models of either hadronic (via π^0 decay) or leptonic (via inverse Compton scattering) emission can be fit to the observed data. There are several approaches being taken to solve this problem: deeper exposures will reduce the size of statistical errors on measurements; tailored observation conditions and analyses can probe the highest and lowest energies visible to the current generation of telescopes, eventually hoping to cover continuous wavelengths; and sampling a larger population of SNRs will paint a more representative picture of this class of object. A number of individual examples of SNRs accelerating leptons, hadrons, and as-yet-unidentified particles are discussed in detail in Chapter 2, Section 2.2.

3.4.1.4 Stellar Winds and Superbubbles

Diffusive shock acceleration (DSA) of particles can occur anywhere there is a shock front. While SNRs are an obvious example of such an environment, massive stars in close proximity can also produce shocks capable of accelerating particles, and thereby producing gamma rays. Massive stars produce high velocity stellar winds, or outflows of gas from the upper atmosphere of the star. When two massive stars are in a binary system, the meeting of their stellar winds produces a shock front capable of supporting DSA [36].

Massive stars in a cluster can also accelerate particles, producing gamma rays. This occurs through a combination of two factors: stellar winds and SNRs. Massive stars evolve more rapidly than their less massive counterparts, meaning that their lives are shorter. Their mass also dictates that, when they die, they do so in a supernova, leaving behind a SNR. Thus, clusters of massive stars often have a higher density of SNRs than the typical Galactic average. The combination of SNR shocks and stellar winds in close proximity results in a net outflow from the cluster, creating a superbubble within the interstellar medium (ISM) (see Chapter 2, Section 2.1 for a more detailed discussion of superbubbles). The interaction of the superbubble with the ISM produces a shock front where particles can be accelerated and produce gamma-ray emission [75].

Although no massive star binaries or clusters have been firmly identified as counterparts for as-yet-unidentified gamma-ray sources, several suspected associations exist. Massive star clusters Westerlund 1 [108][109], Westerlund 2 [110][111], and W43 [110][112] have been associated with sources detected by *Fermi*-LAT and H.E.S.S., although in each case an ambiguity exists regarding the possible source of the observed emission. Additionally, H.E.S.S. has detected VHE emission positionally coincident with the star-forming region W49A, although the detection was of marginal statistical significance (4.4σ) [113]. The source HESS J1614-518 may be associated with the star-forming region Pismus 22 [114], although subsequent X-ray observations favor an association with a SNR [115]. Further observations, in both gamma-ray and lower energy regimes, may reveal suitable counterparts for some of these sources, although in some cases significant improvements in understanding are unlikely to be made without the next generation of instrumentation.

3.4.1.5 Globular Clusters

Globular clusters are gravitationally bound groups of stars orbiting a galaxy. It is thought that they may contain a high density of dark matter compared to typical interstellar values, making them a potential source of gamma rays (see Section 3.4.2.5 of this chapter for a discussion of gamma-ray emission from dark matter) [75]. Furthermore, TeV emission has been detected from a position coincident with the globular cluster Terzan 5 by the H.E.S.S. collaboration [116]. It has been suggested that the emission from this particular cluster could be due to a large population of millisecond pulsars within the cluster, producing accelerated electrons which then can undergo inverse Compton scattering to produce gamma rays [117]. While the observed TeV emission is extended and slightly offset from the center of the cluster, no other likely source lies within the emission region, and the probability of the positional coincidence being random is $\sim 10^{-4}$ [116].

3.4.1.6 Binaries

Four binary systems featuring at least one compact object (black hole or neutron star) have been observed to emit TeV gamma rays (PSR B1259/LS 2883, LS 5039, LS I+61°303, HESS J0632+057), and an additional TeV source (HESS J1018-589) is suspected to be associated with a known GeV binary (see, e.g., [75] and references therein). While this class of sources is not very populous, it remains one of the most intriguing and least well understood. Each system exhibits a different pattern of TeV emission, sometimes relating to the orbital period of the binary and sometimes not. In two of the systems, LS I+61°303 and HESS J0632+057, orbit-to-orbit variability has been observed [118][119] (see Figure 3.9). Four of the five systems (all except HESS J0632+057) exhibit GeV emission [120][121][122][123], but LS 5039 and LS I+61°303 demonstrate an exponential cutoff in the GeV spectrum, indicating that the GeV and TeV emission mechanisms differ. More data is needed to constrain models of emission from these systems, and the discovery of more systems exhibiting nonthermal radiation would improve understanding of this class of objects as a whole.

3.4.1.7 The Galactic Center

The region around the center of the Milky Way is complex in any waveband, but is particularly so in gamma rays. This portion of the sky is best viewed from the southern hemisphere, so the H.E.S.S. telescopes are best positioned to observe it, although CANGAROO-II, Whipple, and MAGIC have also published observations [127] [128] [129] [130]. H.E.S.S. observations first revealed the presence of a bright, steady, point-like gamma-ray source near the central supermassive black hole, Sgr A*. It remains unclear if the emission is from Sgr A* itself, or from a nearby PWN (G359.95-0.04)[127]. In addition to this central source, faint extended emission can be seen in either direction along the Galactic plane. This fainter emission corresponds in location to giant molecular clouds, and is likely due to the interaction of cosmic ray protons with the material in the clouds, leading to π^0-decay gamma rays. Searches for emission due to dark matter self-annihilation have also been performed in this region,

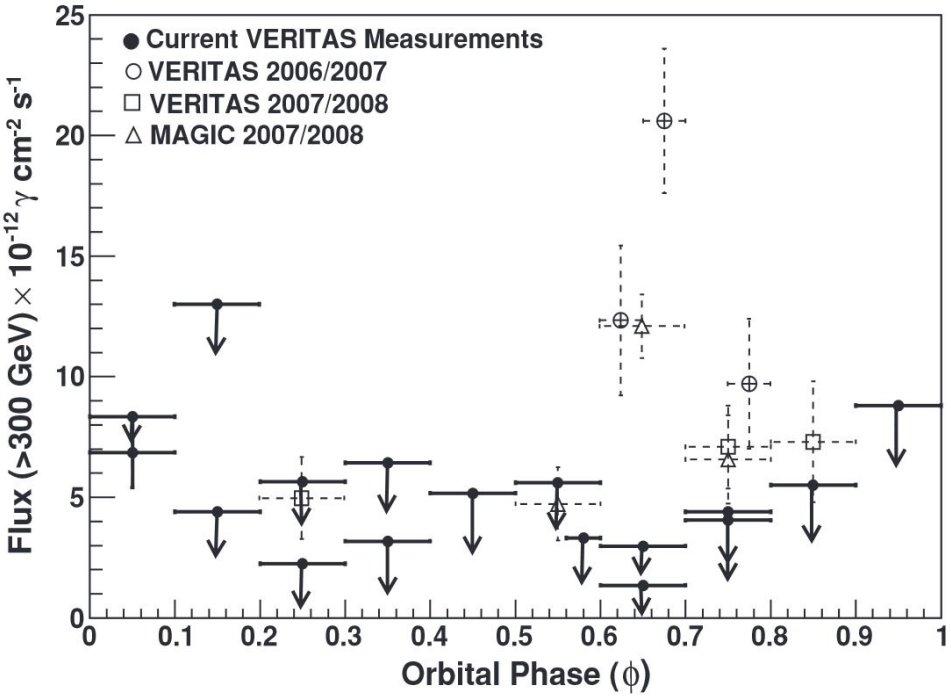

Figure 3.9: Figure 6 from [118], illustrating orbit-to-orbit variability in LS I+61°303. ©AAS. Reproduced with permission. "Observations presented in this paper (solid lines) along with previous observations (dashed lines) from Acciari et al. [124][125] and Albert et al. [126]. Only detections at a significance larger than 3σ are shown from previous observations."

but the analysis is difficult because of the number of astrophysical sources present, and no signal has been detected [131] (see Section 3.4.2.5 of this chapter for a discussion of gamma-ray emission from dark matter).

3.4.1.8 Unidentified Objects

There are a number of TeV sources whose counterparts at other wavelengths remain unidentified. This is more of a problem within the Galactic plane than for extragalactic sources; a higher concentration of sources, as well as diffuse emission, can make source identification difficult within the Galaxy. Approximately a third of detected Galactic TeV sources remain unidentified [75].

Many of these unidentified sources are probably PWNe, since the TeV emission from these sources can be offset from the originating pulsar or X-ray PWN. Several PWNe have been discovered first at TeV energies, with later radio, X-ray, and GeV gamma-ray observations revealing the previously unknown energetic pulsar. Two such sources are MGRO J2019+37 and MGRO J2031+41, both discovered as TeV sources by the Milagro collaboration (see Chapter 4, Section 4.3.1 for a description of Milagro), with associated pulsars later detected by the *Fermi*-LAT Collaboration [132], although it is worth noting that the observed TeV flux from MGRO J2019+37 may contain contributions from multiple unresolved sources [133]. One still-unidentified TeV source is TeV J2032+4130. This was the first detected TeV source with no known multiwavelength counterpart (see Figure 3.10). Current interpretations favor the PWN scenario for this source, although other explanations could also describe the data [134].

3.4.2 Extragalactic Sources

3.4.2.1 Active Galactic Nuclei: Blazars, Flat Spectrum Radio Quasars, and Radio Galaxies

Most of the ∼50 extragalactic TeV sources now known are active galactic nuclei (AGN) [36]. An AGN is defined by having a very luminous galactic core, and ∼10%

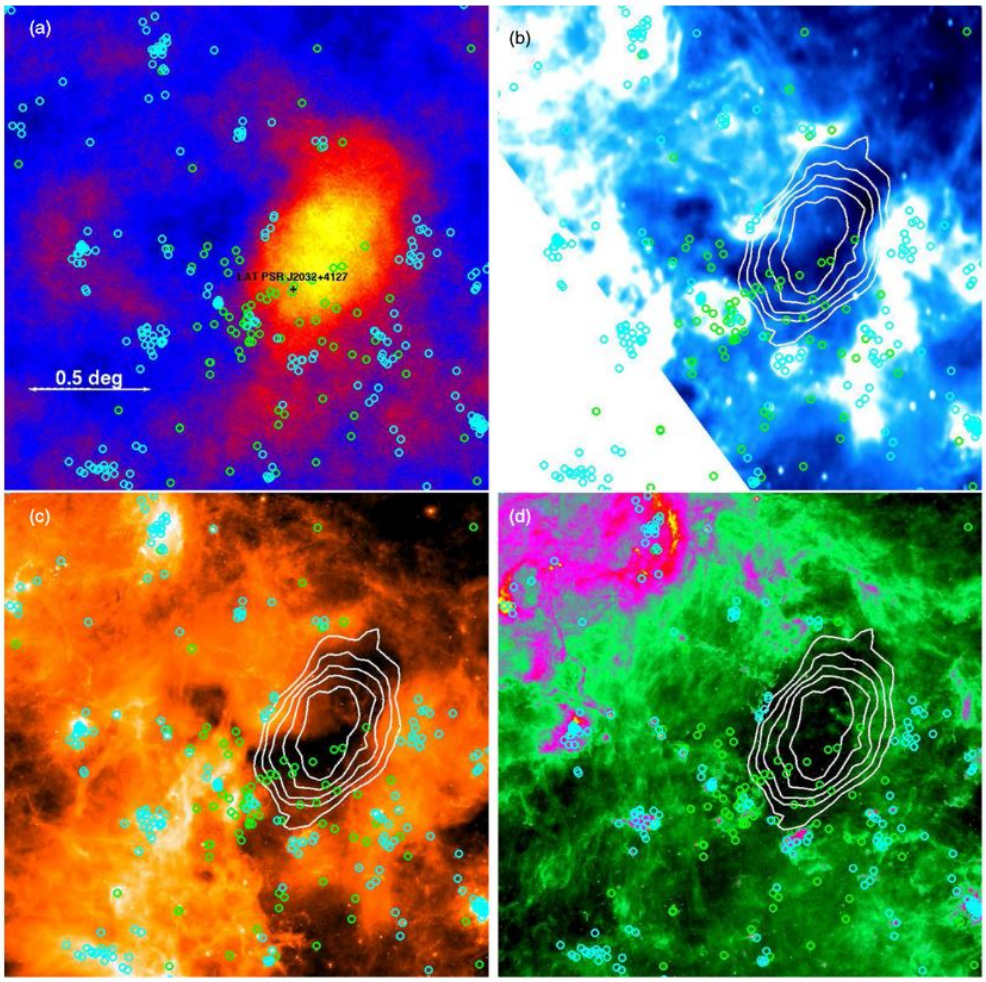

Figure 3.10: Figure 5 from [134], showing multiwavelength observations of TeV J2032+4130. ©AAS. Reproduced with permission. "VER J2031+415 and its vicinity at different wavelengths. (a) VERITAS significance map with the position of *Fermi*-LAT PSR J2032+4127 indicated by a black cross. (b) 1.4 GHz image from the Canadian Galactic Plane Survey (CGPS; [135]). (c) Spitzer MIPS 24 μm image from the MIPSGAL survey [136]. (d) Spitzer GLIMPSE 8 μm image [137] [138]. In images (b), (c), and (d) the VERITAS significance contours from 4-8 standard deviations are shown as white curves. Green circles are OB stars [139]. Cyan circles are star-forming regions [140]."

of AGN feature relativistic jets. The jets are thought to be powered through accretion onto a supermassive black hole in the galactic center [141].

Blazars, the most populous category of extragalactic gamma-ray sources, are AGN with the jets oriented near the line-of-sight to Earth. Due to their orientation, jets from blazars demonstrate relativistic beaming effects which drastically increase the energies and luminosities of observed photons, making them interesting gamma-ray sources. Blazars are also highly variable across the electromagnetic spectrum, flaring on timescales ranging from minutes to years, which allows constraints to be placed on the size of the emission region. Blazar spectral energy distributions (SEDs) exhibit a low energy peak due to synchrotron emission, and also a higher energy peak (see Figure 3.11). A sub-category of blazars are BL Lacertae objects, named for the first of such objects discovered. These are further categorized into high- ($> 10^{15}$ Hz), intermediate- (10^{14} - 10^{15} Hz), and low-frequency ($< 10^{14}$ Hz) peaked BL Lac objects, depending on the location of the high-energy peak in the SED [141].

The mechanism for producing the observed gamma-ray emission in these objects is still poorly understood. Models featuring synchrotron self-Compton emission from electrons accelerated in shocks in the jets are generally favored (see Section 3.4.1.1 of this chapter for a discussion of synchrotron self-Compton emission). These models are supported by the strong correlation observed between X-ray and TeV emission. However, models of hadronic emission do exist, wherein gamma rays are produced through interactions of hadrons with ambient matter or photon fields. A point against hadronic models is that they make rapid variability difficult to explain [36]. The exception to this is the possibility of proton synchrotron emission, where high energy protons interact with strong magnetic fields within the jet [142].

Flat Spectrum Radio Quasars (FSRQs) are another class of AGN. FSRQs are defined by bright ultraviolet (UV) emission from their central accretion disk, broad emission lines in the optical portion of their spectra, and infrared (IR) emission from a dusty torus. TeV emission from these objects is thought to be due to inverse Compton scattering of electrons accelerated in shocks within the jets [75]. To date, three FSRQs

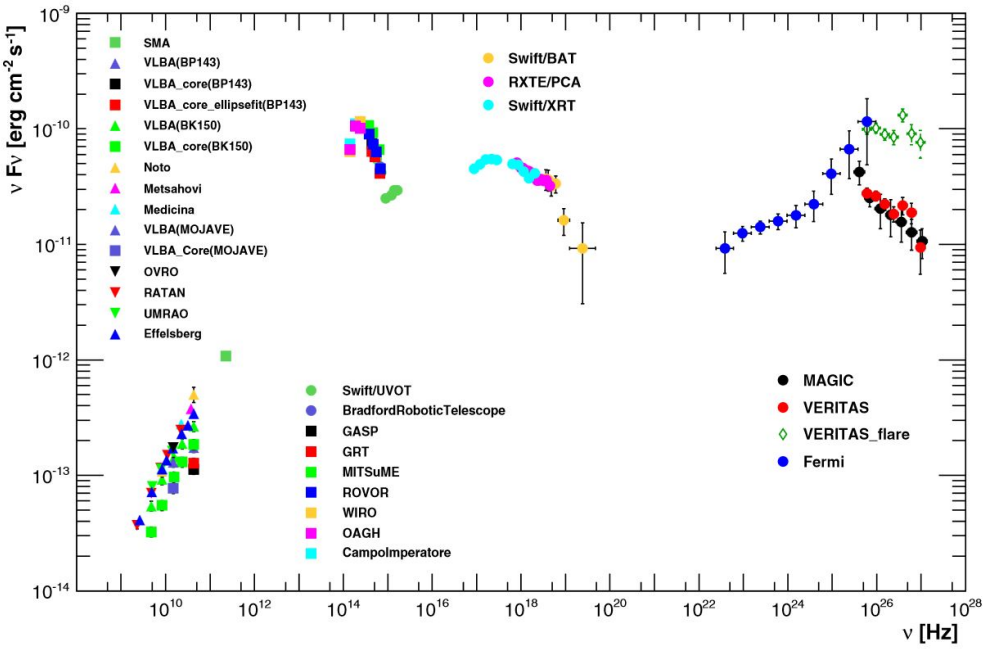

Figure 3.11: Figure 8 from [143]. ©AAS. Reproduced with permission. "SED for Mrk 501 averaged over all observations taken during the multifrequency campaign performed between 2009 March 15 (MJD 54905) and 2009 August 1 (MJD 55044). The legend reports the correspondence between the instruments and the measured fluxes. Further details about the instruments are given in Section 5.1 [of [143]]. The optical and X-ray data have been corrected for Galactic extinction, but the host galaxy (which is clearly visible at the IR/optical frequencies) has not been subtracted. The TeV data from MAGIC and VERITAS have been corrected for the absorption in the EBL using the model reported in [144]. The VERITAS data from the time interval MJD 54952.9-54955.9 were removed from the data set used to compute the average spectrum, and are depicted separately in the SED plot (in green diamonds)."

have been observed to produce TeV gamma rays: PKS 1222+21 [145], PKS 1510-089 [146], and 3C279 [147].

Radio galaxies are also AGN with jets, but their jets are not oriented towards Earth. This provides the opportunity to resolve the jet in its entirety from radio through X-ray wavebands. Thus, variations observed in the gamma-ray emission, which can be emitted at large angles from the jet, can potentially be correlated with changes observed in the jet at other wavelengths [36]. Like other AGN, these sources are highly variable, but the acceleration site (and therefore the site of gamma-ray emission) within the structure remains elusive. VHE flares have been observed to correlate with changes both in the jet and, separately, in the core region surrounding the central supermassive black hole, leaving open both possibilities as the site of emission. Currently three radio galaxies have been confirmed to exhibit TeV emission: M87 [148] [149] [150] [151], Centaurus A [152], and NGC 1275 [153]. A fourth radio galaxy, 3C 66B, may have been detected at TeV energies [154], but there is some ambiguity as to the source of the emission because of the small angular separation (6') from known blazar 3C 66A. Note that these galaxies are all nearby, with redshifts of $\leq$0.02; were they farther away, they would be too dim to detect in gamma rays.

3.4.2.2 Starburst Galaxies

Starburst galaxies are galaxies with higher rates of star formation, and hence a higher population of massive stars which eventually become supernovae, than our own Milky Way. So far, two starburst galaxies have been observed to emit high-energy gamma rays: M82 [155] (see Figure 3.12) and NGC253 [156]. There are two explanations currently proposed to explain the observed emission. SNRs, especially in relatively close proximity, provide dense gas as a target material for interactions with accelerated hadrons. And, it is thought that hadrons are accelerated by SNR shock fronts. Thus, accelerated hadrons interact with the gas and produce π^0, which decay into gamma rays. The other explanation is that the high SN rate produces a large population of PWNe. These PWNe produce gamma rays individually as discussed in

Section 3.4.1.1 of this chapter, but their overall combined luminosity is consistent with the observed diffuse emission. More data will permit better measurements of the TeV spectra of these objects, which will help in discriminating between models [75].

3.4.2.3 The Large Magellenic Cloud

Although the flux of gamma rays from discrete sources within galaxies other than the Milky Way is generally too low to be detected with current instrumentation, H.E.S.S. has detected a TeV source in the Large Magellenic Cloud, one of two satellite galaxies orbiting the Milky Way. The source is positionally coincident with the pulsar PSR J0357-6910, the most powerful pulsar currently known. The most likely mechanism for generating the observed TeV emission is electrons from the associated PWN interacting with ambient IR photons to produce inverse Compton emission [158].

3.4.2.4 Gamma-Ray Bursts

Gamma-ray bursts (GRBs) are one of the most elusive phenomena in modern astronomy. First discovered serendipitously in the late 1960s by the Vela 4 military satellites [159], they fall observationally into two categories: long- and short-duration bursts. When they occur, these bursts far surpass in luminosity every other gamma-ray source in the sky, for a short period of time. It is thought from the distribution of types of originating host galaxies and their stellar populations that long- and short-duration bursts arise from different progenitor systems. Long bursts are suspected to be associated with stellar collapse events which create black holes, and short bursts are thought to be due to compact object mergers (e.g., two neutron stars) [160]. It is certain that these events are occurring at cosmological distances, providing a glimpse of a younger, more violent universe. GRBs are first detected in soft gamma rays or hard X-rays by survey instruments, with a lower energy afterglow to follow; the small field-of-view of ground-based VHE telescopes (Imaging Atmospheric Cherenkov Telescopes, or IACTs) means that rapid repointing is usually required once an alert is received. Although IACTs now regularly begin observations of burst locations less

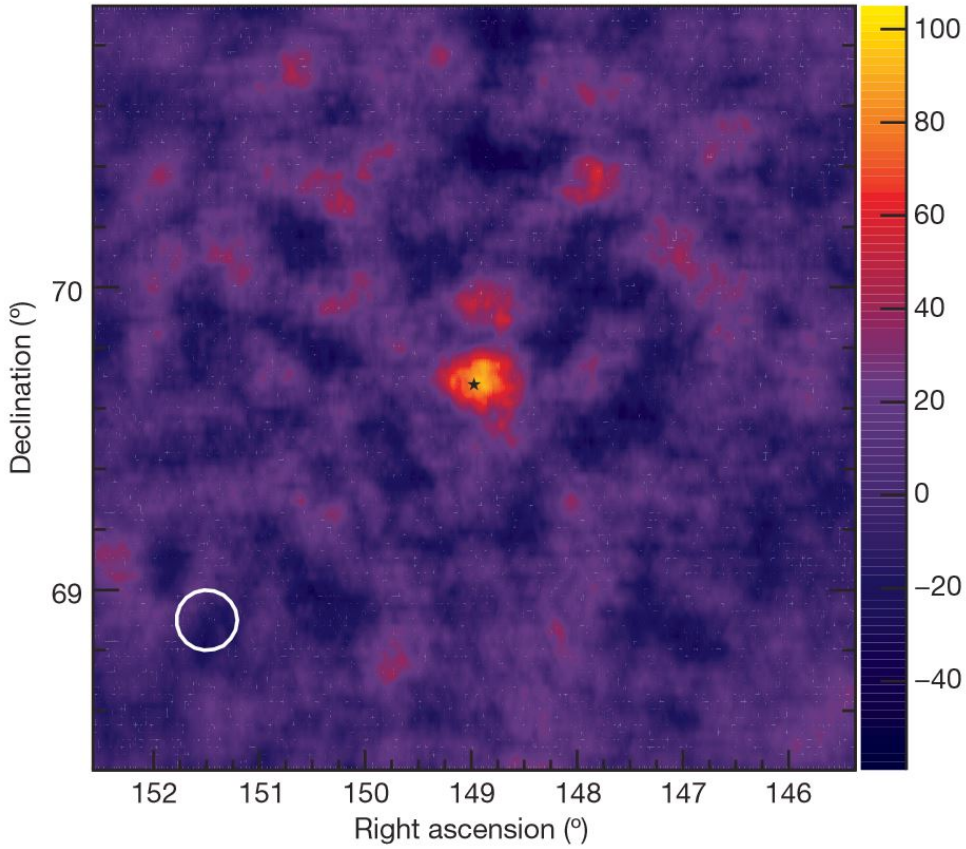

Figure 3.12: Figure 1 from [155]. "VHE image of the M82 region. The sky map shows the measured excess (colour scale) of γ-ray-like events above the estimated background from a region centred on M82. Each pixel contains the excess in a circular region of radius 0.1°. The map is oversampled; neighbouring pixels are thus correlated. The background for each point is estimated using an annulus centred on its position (the ring method [157]). The spatial distribution of the observed excess is consistent with that expected from a point-like source located near the core of M82. The white circle represents the VERITAS point spread function (68% containment) for individual γ-rays. The uncertainty in the source localization is much smaller. The black star denotes the location of the core of M82. The coordinates are for the J2000 epoch."

than 100 seconds after an alert is received, there has yet to be a statistically significant detection of >100 GeV emission from a gamma-ray burst. It is uncertain if this is due to timing (VHE emission may be over by the time the telescope slews to the location of interest), or because the expected VHE flux is at the edge of sensitivity for the current generation of instruments. Models predicting TeV emission from these events feature a variety of mechanisms, including both inverse Compton emission of electrons accelerated in shocks [161] and ultrarelativistic protons interacting with background radiation or plasma to produce neutral pions which decay to gamma rays [162].

3.4.2.5 Dark Matter

Dark matter, or matter that can only interact with the visible universe gravitationally or via the nuclear weak force, remains on the cutting edge of physics research. There are several models describing dark matter, one of which features Weakly Interacting Massive Particles (WIMPs). WIMPs are expected to either decay or self-annihilate, producing a variety of observable subatomic particles and gamma-ray photons [163]. Dwarf spheriodal galaxies, which have a high concentration of dark matter and a low concentration of astrophysical TeV sources, are good candidates to detect any gamma rays produced by WIMPs. Thus far, despite deep exposures on several dwarf galaxies, no VHE gamma-ray signal has been detected, but upper limits on the velocity-weighted annihilation cross section are constrained to within 2 orders of magnitude of the canonical value (see, e.g., [164], [165]). It is possible that the predicted sensitivity necessary will be achieved with the next generation of IACTs [162].

Chapter 4

INSTRUMENTATION FOR OBSERVING GAMMA RAYS

4.1 Imaging Atmospheric Cherenkov Telescopes

The Imaging Atmospheric Cherenkov Telescope (IACT) is the workhorse of modern VHE gamma-ray astronomy. These telescopes are cleverly designed, using Earth's atmosphere as a key part of the detector. Since gamma rays are not directly observable from ground level, these telescopes actually detect the Cherenkov light produced by gamma rays (and cosmic rays) interacting with the atmosphere. The crucial elements of an IACT are a mirrored surface for light collection, a photodetector to which the light is focused, and electronics to process the signals produced by the detector.

4.1.1 Historical Instruments

The first experiment showing that flashes of Cherenkov light in the night sky were indeed detectable with a photomultiplier tube was published in 1953 by Galbraith and Jelley [166]. The first telescope to attempt to make use of the Cherenkov light produced by gamma rays was operated by the Lebedev Institute in the Crimea from 1960-1964 (see Figure 4.1) [73]. Although this telescope did not detect any sources during its operation, it pioneered the atmospheric Cherenkov technique and showed that it was a feasible method.

The first telescope designed specifically for gamma-ray observations was the 10-meter Whipple telescope, built on Mount Hopkins, Arizona in 1968 (see Figure 4.2). It incorporated a much larger reflecting area, with a diameter of 10 m, allowing for the detection of lower energy photons [73]. It was not until 1989, however, that the Whipple

telescope made the first statistically significant detection of a steady celestial gamma-ray source: the Crab Nebula [85]. This discovery marked the beginning of ground-based gammma-ray astronomy as a recognized discipline within the astronomical community.

In 1997, the High Energy Gamma Ray Astronomy (HEGRA) telescope began operations on La Palma, in the Canary Islands. Comprised of five 3.3-meter diameter telescopes [167], this was the first gamma-ray instrument to succesfully make use of an array of telescopes. Combining images from multiple telescopes gives better angular resolution, and also better discrimination of gamma-ray events from cosmic ray events.

Several other Cherenkov telescopes were operational from the mid-1990s into the early 2000s, and indeed, some of these continue to operate today. They are summarized in Table 4.1. In addition, there were several solar research facilities whose light-collecting infrastructure was used to collect Cherenkov light from low energy

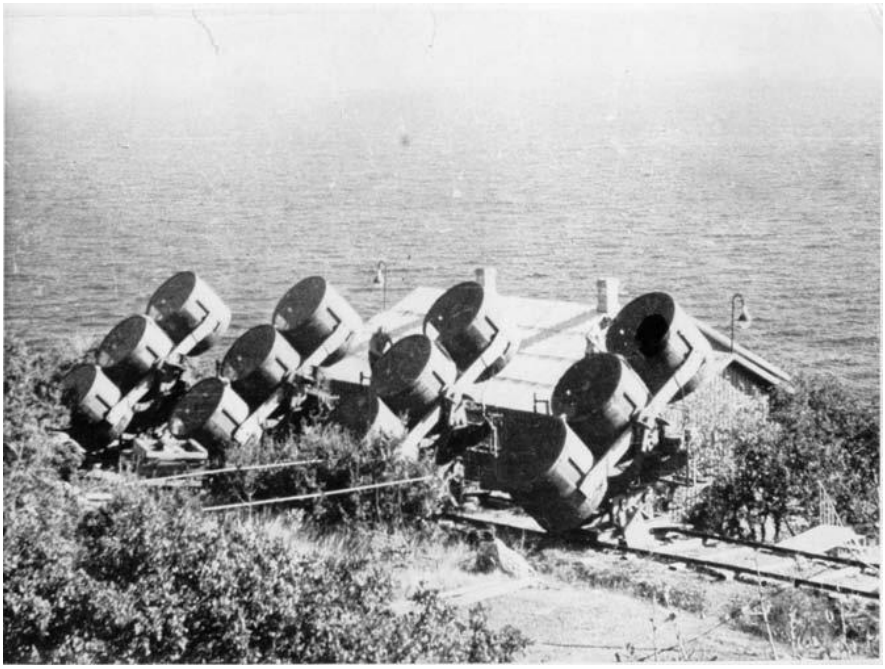

Figure 4.1: Figure 1.2 from [73]. "The Lebedev Institute experiment that operated in the Crimea, *c.* 1960-1964. This was the first major VHE telescope. (Photo: N.A. Porter.)"

Figure 4.2: Figure 1.3 from [73]. The Whipple 10 m gamma-ray telescope.

air showers during nighttime hours. The two best known of these experiments were STACEE (see, e.g., [168]) and CELESTE (see, e.g., [169]) (see also, e.g., [170] for a review of other solar array experiments). These instruments were sensitive to gamma rays between ∼50-500 GeV, and so were complementary to IACTs.

4.1.2 Modern IACTs

Modern IACTs are very similar in design to the Whipple and HEGRA telescopes. They consist of a large dish (10-30 m diameter) surfaced with mirror facets, focused to a camera comprised of photomultiplier tubes. Of course, modern instruments benefit from developments in photomultiplier tube quantum efficiency, and in digital signal processing. There are three major IACTs currently in operation: the High Energy Stereoscopic System (H.E.S.S.) in Namibia, the Very Energetic Radiation

Experiment	Location	No. of Detectors	Mirror Area (m^2)	PMTs/Camera	Elevation (km)	Energy Threshold (GeV)	Began Operations	References
GT-48	Crimea, Ukraine	2	27	37	0.6	1000	1989	[171], [172]
CANGAROO	Woomera, Australia	1	75	256	0.2	400	1992	[173]
SHALON	Tien-Shan, Russia	1	10	144	3.3	1000	1992	[174], [175]
U. of Durham Mark 6	Narrabri, Australia	3	126	109[a]	0.26	150	1995	[176], [177]
CAT	Pyrenees, France	1	18	600	1.6	250	1996	[178]
TACTIC	Mt. Abu, India	4	10	349	1.3	500	1997	[179], [180]
CANGAROO-II [b]	Woomera, Australia	1	38.5/78.5	552	0.2	200/100	1999/2000	[181]

Table 4.1: A selection of atmospheric Cherenkov telescopes prior to the current generation. Table adapted from [73].

[a] Central detector only; cameras for left and right detectors each have 19 PMTs used mainly for instrument triggering.

[b] CANGAROO was upgraded to a 7-m diameter telescope in March 1999, and was then further upgraded to a 10-m diameter telescope in February 2000

Imaging Telescope Array System (VERITAS) in Arizona, USA, and the Major Atmospheric Gamma-ray Imaging Cherenkov (MAGIC) telescope on La Palma, Canary Islands. Additionally, the Collaboration of Australia and Nippon for a GAmma Ray Observatory in the Outback (CANGAROO-III) operated in Australia from 2004 until ∼2009 [182]. Of these, VERITAS, H.E.S.S., and CANGAROO-III were designed as arrays. MAGIC was a single dish until 2009, when a second telescope was added [183]. H.E.S.S. was an array of four telescopes until 2012, when a fifth, larger telescope was added [184]. This telescope, with an area equivalent to a 28 m circular dish, is the largest Cherenkov telescope built to date. These instruments are further characterized in Table 4.2. The observations that led to the discovery of VHE emission from Tycho were conducted using VERITAS, so I will focus on this instrument.

4.1.3 VERITAS

VERITAS is located at the basecamp of Fred Lawrence Whipple Observatory (FLWO) in Amado, Arizona (31°40'30" N, 110°57'07" W, 1268 m above sea level). The instrument is composed of four, 12 m diameter telescopes. Each telescope has a camera comprised of 499 photomultiplier tubes, with a field of view of 3.5° [185].

In 2003, the first VERITAS telescope was installed at the FLWO basecamp as a prototype. Afterwards, it was decided to construct the full array at the site, resulting in uneven baseline lengths between telescopes. From 2007-2009, VERITAS was fully operational in this original configuration. In summer 2009, telescope T1 was moved to a different location to provide more even baselines (see Figure 4.3). This improved the sensitivity of the array by ∼30% [188].

4.1.3.1 Observing Constraints

VERITAS typically operates from early September through late June or early July. Arizona experiences a monsoon season during the summer, and not only does rainy weather make for terrible sky viewing, but operating during high humidity and lightning storms risks damaging the instrument. Originally, VERITAS did not observe

Experiment	Location	No. of Detectors	Mirror Area (m^2)	PMTs/Camera	Field of View (°)	Elevation (km)	Energy Threshold (GeV)	Began Operations	References
VERITAS	Amado, Arizona	4	424	499	3.5	1.3	100	2007	[185]
MAGIC/MAGIC-II	La Palma, Canary Islands	1/2	241/488	576/1615[a]	3.6/3.5[b]	2.2	60	2004/2009	[186], [183]
H.E.S.S./H.E.S.S.-II	Khomas Highlands, Namibia	4/5	428/1028	960/2048[c]	5/3.5[d]	1.8	30	2003/2012	[187], [184]

Table 4.2: A summary of the current generation of IACTs.

[a] total number of PMTs in MAGIC-II

[b] MAGIC telescope/MAGIC-II telescope

[c] 960 PMTs per camera in H.E.S.S.; additional telescope alone in H.E.S.S.-II has 2048 PMTs

[d] original H.E.S.S. telescopes have a 5° FOV; additional telescope in H.E.S.S.-II has a 3.5° FOV

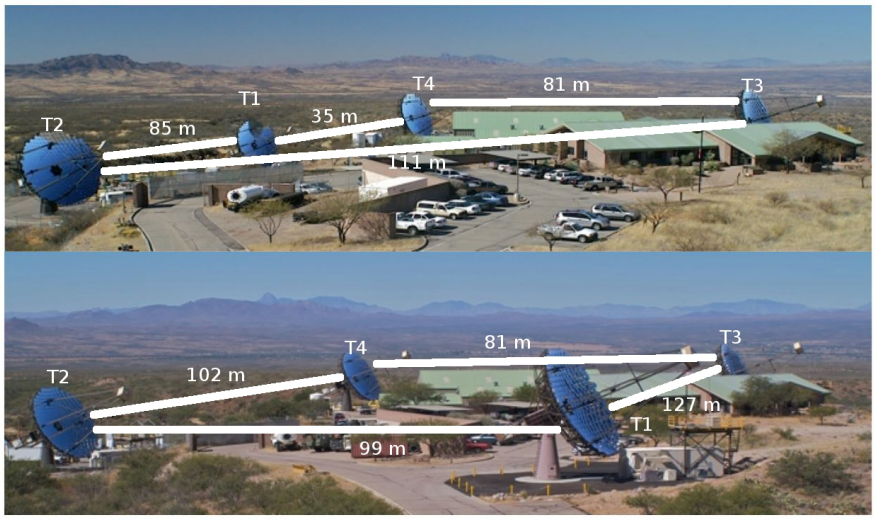

Figure 4.3: Adapted from Figure 1 of [189]. The VERITAS array. The array configuration from 2007-summer 2009 is shown in the top panel, and the configuration from summer 2009-present is shown in the bottom panel. Note especially the very short distance between telescopes T1 and T4 in the original layout.

while the moon (in any phase) was up because of the concern that the ambient light would be too bright and risk damaging the cameras. Later, this condition was relaxed somewhat, and until the 2011-2012 observing season VERITAS conducted observations during partial moonlight with the telescopes pointing away from the moon; observations were ceased only for a few nights surrounding each full moon. However, in Spring 2012 it was decided after testing that using a combination of ultraviolet filters installed on the cameras and reducing the high voltage to the cameras would create safe conditions for observing during bright moonlight. Even with these precautions, observers must carefully monitor currents in the cameras during moonlight observations, and must select sources as close to 90° from the moon as possible (this is the darkest portion of the sky). Even with these precautions, observations are still not conducted on the night of each full moon and the nights immediately preceeding and following it.

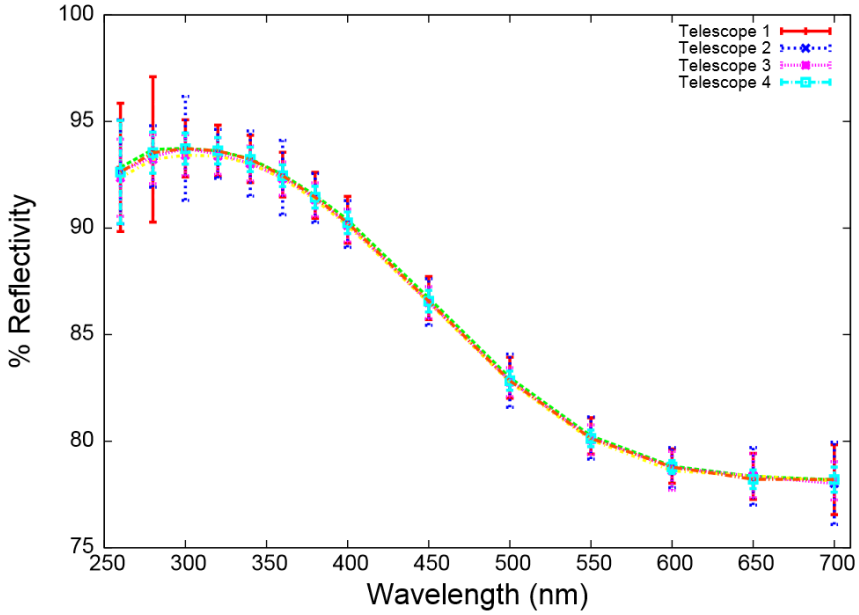

Figure 4.4: Figure 2 from [191]. "VERITAS telescope mirror reflectivity versus wavelength broken down by telescope. The design specified reflectivties of 90% at 320 nm and 85% between 280 nm and 450 nm."

4.1.3.2 Optics

Each of the four VERITAS telescopes is an altitude-azimuth mounted Davies-Cotton design [190], with 345 hexagonal spherical mirrors. The mirrors are 60.96±0.3 cm across the flat sides, and have a radius of curvature of 24 m ± 1%, giving a focal length of 12 m. They have a reflectivity better than 90% at 320 nm (within the wavelength regime for Cherenkov radiation; see Figure 4.4) and, once aligned on the telescope, focus to within a 0.06° point spread function [191]. The total mirror area on each telescope is ∼106 m^2 [188].

4.1.3.3 Camera

The camera is the heart of any IACT. The four VERITAS cameras are each comprised of 499 photomultiplier tubes (PMTs), each of which acts as a pixel in the

camera. During the era of VERITAS's lifetime when the data in this work were collected, the PMTs were 28 mm Photonis XP2970 phototubes [188]. In Summer 2012, all of the PMTs were replaced with 25.4 mm Hamamatsu R10560 phototubes. These PMTs contain superbialkili photocathodes, which have a higher quantum efficiency than traditional bialkili photocathodes (see Figure 4.5). At the time of writing, the new PMTs have been installed and detailed studies of the improvements are being performed. The upgrade has resulted in a lower energy threshold and higher sensitivity. Each of the four cameras has a total field of view of $\sim 3.5^{\circ}$, with each individual PMT viewing $\sim 0.14^{\circ}$.

During operations, each PMT has a voltage applied to it, typically in the range of 800-1000 volts. The calibration of the voltage value for each PMT will be discussed in Chapter 5, Section 5.2.1. With the high voltage on, if a photon contacts the face of the PMT, the photocathode emits an electron, which produces a current across the voltage gap. More photons result in a higher current. The current is monitored in real time by the observers during operations, and any PMT generating too large a current is automatically shut down by the high voltage control software to avoid damaging the PMT. This may occur because the voltage setting is incorrect and needs to be recalibrated, because a bright star aligns with a particular PMT during a particular pointing, or because the PMT is broken.

The currents generated in each PMT are AC-coupled and converted to voltages by a pre-amplifier located physically at the base of each PMT. These serve to amplify the signals with a gain of 6.66 [193], minimizing loss due to attenuation in the coaxial cables connecting the PMTs to the signal-processing electronics. The pre-amplifiers also provide a direct DC output to the current monitoring system; it is these live-time readouts of the current in each PMT that are monitored by the observers, and in which fluctuations above a pre-defined threshold cause the high voltage software to shut down a given PMT. Also housed in the camera box is the charge injection system, in which a programmable pulse generator is connected to the current monitor boards. This allows for artificial pulses to be sent from selected PMTs, which is useful when testing the

data acquisition system during daylight or other conditions not suitable for the PMTs [194].

4.1.3.4 Tracking and Pointing

The telescopes are each driven by altitude-azimuth positioners. These have a pointing accuracy of $\leq 0.005°$, and can achieve drive speeds as quick as 1° per second [195]. The ability to slew quickly not only minimizes the loss of observing time when changing sources during the course of normal observing, but also allows for fast

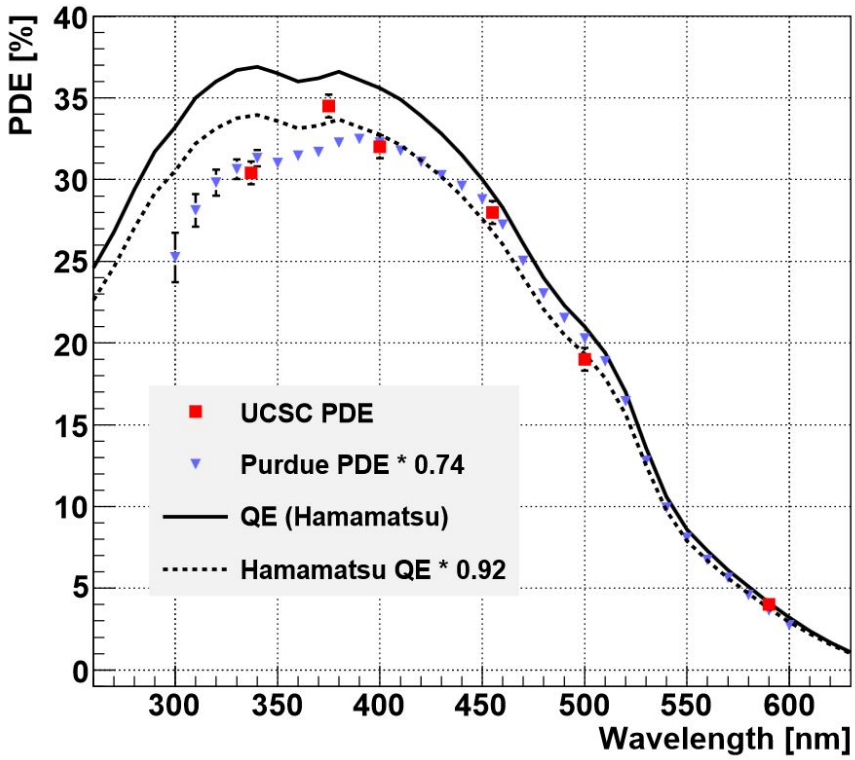

Figure 4.5: Figure 6 from [192]. "Photon detection efficiency, Hamamatsu QE and PDE we measured." The photon detection efficiency (PDE) of several models of PMT was tested by VERITAS collaborators at the University of California, Santa Cruz (UCSC) and at Purdue University. From this value, the quantum efficiency (QE) of the PMT can be determined. These results are shown for the PMTs which were selected for use in the VERITAS upgrade. Also shown is the reported QE of these PMTs from the manufacturer, Hamamatsu.

responses to gamma-ray burst (GRB) alerts (see Chapter 3, Section 3.4.2.4 for a discussion of GRBs).

Immediately in front of the cameras are mounted a set of light cones. These reflective cones fill in the gaps between photomultiplier tubes (PMTs) that comprise the camera, directing photons into the PMTs that might otherwise fall between them. On the edges of the plates supporting the light cones are four red light emitting diodes (LEDs), which are used in monitoring the telescope's pointing accuracy. The VERITAS Pointing Monitor (VPM) consists of two charge-coupled device (CCD) cameras and a set of four LEDs for each telescope [196]. One CCD camera (the "sky camera") is mounted to the frame of the telescope, aligned with the telescope's optical axis, and pointed at the sky. The other CCD camera (the "focal plane camera") is pointed at the telescope's PMT camera. The four LEDs allow for accurate measurement of the actual light cone positions (and therefore camera position) in the images taken by the focal plane camera. Approximately once a month, calibration measurements are taken wherein a white screen is placed over the PMTs and the telescope is pointed at a series of bright stars at various elevations. The observers record the centroid position of the star in both the sky and focal plane cameras, and through comparison are able to determine which PMT actually corresponds to the telescope's optical axis. Ideally, this is the central PMT in the camera, but any known offset can then be corrected for. A study performed using Crab Nebula data from 2009 and 2010 revealed that the typical pointing offset is $\sim$20". In analyzed data, this results in a source localization uncertainty of $\sim$25".

4.1.3.5 Trigger System

VERITAS data consists of flashes of Cherenkov light, referred to as *events*, reflected from each telescope to the camera. To determine if light in the PMTs qualifies as an event (as opposed to random background light) and is recorded, a three-level triggering system is used. The first level, L1, selects for the amount of light in an individual PMT. This helps to select relatively bright flashes of Cherenkov light from

general night sky background light. This task is accomplished with the use of constant fraction discriminators (CFDs). These differ from simple threshold discriminators in that the trigger always occurs after the same time delay from the beginning of the event, no matter the input pulse's shape or amplitude [197]. The threshold at which a PMT triggers the L1 system is measured in mV, corresponding to the number of photoelectrons produced by the PMT. This is a value which is set experimentally by measuring bias curves. Bias curves are taken by pointing the telescopes at a dark patch of sky, setting the CFD threshold to a relatively high value, and successively reducing that value. As the CFD threshold is reduced, night sky background events will trigger the system more and more frequently, and will eventually dominate any Cherenkov signal. The goal is to set the threshold at a level where triggering night sky background events, along with deadtime for reading out the electronics, are minimized, but as many low-energy gamma-ray events as possible are kept. For the data in this work, a 50 mV CFD threshold (corresponding to ~ 20 photoelectrons) was used, which was the standard operating threshold for dark sky observations at the time. Figure 4.6 shows an example bias curve.

The second level trigger, L2, requires that several adjacent pixels trigger the L1 system within a given length of time. This eliminates background light triggering only a single pixel, and also imposes the requirement that all the triggering light comes from the same place on the sky (hence adjacent pixels, not simply any coincidentally triggering pixels). Currently, as well as during the era when the data on Tycho were recorded, the L2 trigger requires a minimum of 3 adjacent PMTs to trigger L1 within 6 ns.

The third level trigger, L3, ensures that only events triggering two or more telescopes within a given time window (currently 50 ns) are recorded. The L2 signals are sent to the L3 computer, which inserts a pre-defined delay for each telescope into the signal to account for the different cable path lengths from each telescope and the differences in Cherenkov light arrival time to each telescope due to physical location and pointing, and then searches for coincident signals. The L3 trigger helps to eliminate

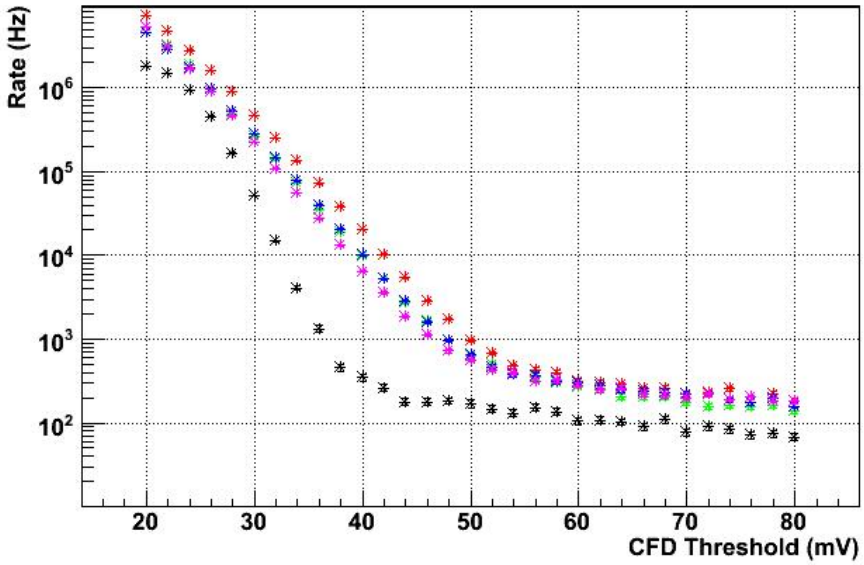

Figure 4.6: Example bias curve, taken June 17, 2012. The red, green, blue, and purple stars indicate the L2 rates from T1, T2, T3, and T4, respectively. The black stars indicate the L3 rate for the array.

background light produced by muons, which are created in air showers and can be relativistic, thus producing Cherenkov light. If a muon travels straight down the axis of a telescope, its Cherenkov light cone will produce a ring in the camera. If instead a muon impacts a telescope at an angle, a full ring will be produced, but will be offset and will not be fully contained within the camera (see Figure 4.7). But, if the muon lands near a telescope instead of on it, only a partial ring will be produced. Small ring fragments can trigger only a few adjacent pixels, looking like a gamma ray. However, the Cherenkov light cones from muons are too small to be seen by more than one telescope at a time, so the array-level L3 trigger can effectively remove these background events.

4.1.3.6 Data Acquisition and Recording

Each PMT is connected via a 140-foot-long [194], 75 Ω coaxial cable [193] to a channel on a Flash Analog-to-Digital Converter (FADC) board. The FADC samples

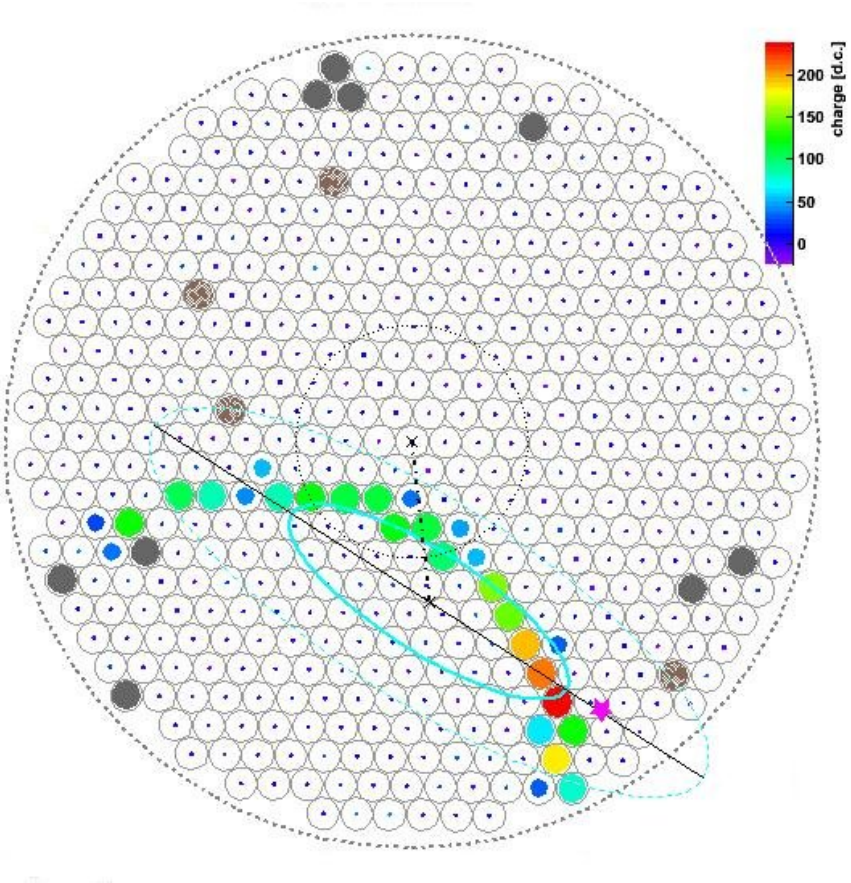

Figure 4.7: Example of a full, but offset, muon ring seen in one of the cameras.

each PMT signal at a rate of 500 MHz (every 2 ns) to produce a digitized version of the signal containing both pulse shape and timing information (see Figure 4.8). The digitized pulse has 8-bit resolution in its standard mode, the high gain mode. If the amplitude of a pulse exceeds the range provided by the high gain mode, the signal is instead processed through a low gain path, where the gain is reduced by a factor of 6. The amplitude of the pulse is measured in digital counts (dc), which is correlated to the number of photoelectrons (pe) originating from that PMT. VERITAS operates with 1 pe = 5.3 dc, such that the signal from a single photoelectron is just measureable by the FADC system (see Chapter 5, Section 5.2.3 for a detailed description of this calibration measurement). A single photoelectron produces a pulse of height 2.4 mV

[194].

When an L3 signal is generated, it is sent back to the FADCs, signalling a busy state for the boards during which a buffer segment is read out. The entirety of the buffer is 64 μs. The location of the segment within the buffer is determined by the externally-dictated lookback time, and the length of the buffer segment is also externally determined to be long enough to contain the entire pulse (20 samples, or 40 ns, for the Tycho data, as with all standard VERITAS data). Only the buffer segment containing the pulse is read out, in order to minimize deadtime during which the FADCs are in a busy state. These buffer segments are sent to the "Eventbuilder" in each telescope, at which point the busy signal in the FADCs is turned off and buffering begins again. The Eventbuilders are computers, one for each telescope, which run software to combine the signals from each FADC crate into a single event. Each

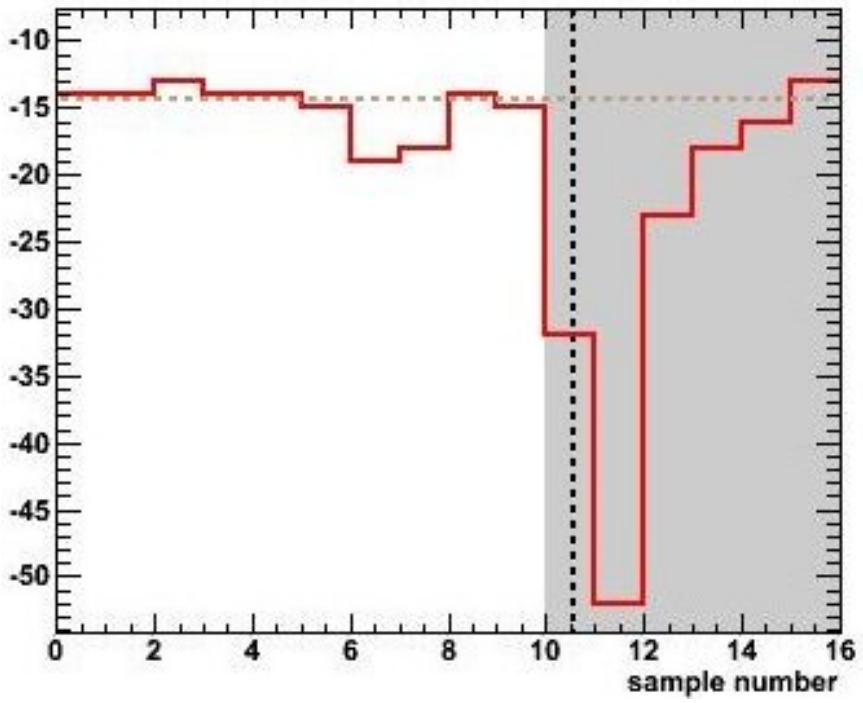

Figure 4.8: An example of an event FADC trace. The y-axis is given in digital counts, which can be converted to a number of photoelectrons (1 pe = 5.3 dc), and the x-axis is given in FADC samples (1 sample = 2 ns).

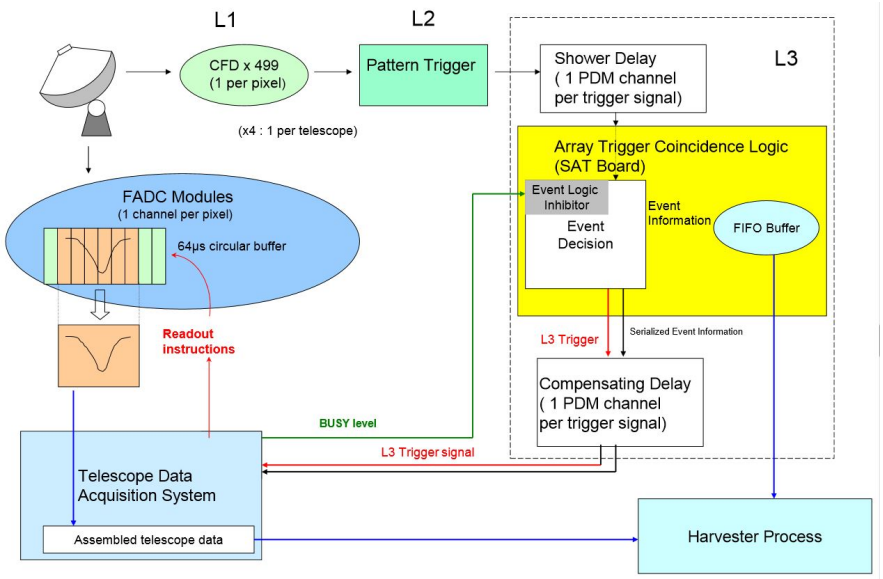

Figure 4.9: Figure 1 from [198]. "Illustration of the trigger system's operation and interface with data acquisition." Acronyms are defined as follows: CFD - Constant Fraction Discriminator; FADC - Flash Analog-to-Digital Converter; PDM - Pulse Delay Module; SAT - SubArray Trigger; FIFO - First In, First Out

Eventbuilder then passes on its signals to the array-level "Harvester". The Harvester, a single computer getting signals from each telescope in the array, is responsible for generating a file for each data run, containing the shapes and timing of all events from all telescopes. The files are a customized data format, known as VERITAS bank format files (.vbf). These files are compressed and stored on a secure server, where they are available for download to VERITAS collaboration members. Each compressed file for a 20-minute data run is ∼5.5-8.5 GB; in a night where, e.g., 10 hours are spent observing, ∼200 GB of data are generated. A schematic of the telescope electronics is shown in Figure 4.9.

4.2 Gamma-Ray Satellites

In Chapter 2, I briefly discussed the opacity of Earth's atmosphere to gamma rays. Because of this, satellite-based telescopes are a natural tool to use when studying

gamma rays. Space-based gamma-ray telescopes are sensitive to gamma rays in the HE regime. In principle, a space-borne detector could be used to observe VHE gamma rays, but the low flux of such photons combined with the small collection area available on launched instruments makes the prospect impractical. To illustrate this, consider the Crab Nebula, the brightest steady gamma-ray source in the Northern Hemisphere sky. Its flux above 1 TeV is on the order of 10^{-11} photons/cm^2/s. The effective collection area of the satellite-based *Fermi*-LAT telescope is $\sim$8000 cm^2 (the *Fermi*-LAT instrument will be discussed in detail momentarily). This results in an anticipated collection of fewer than 10 photons per year. Most known sources of VHE gamma rays emit less than 10% of the flux of the Crab Nebula, so our hypothetical satellite-based VHE instrument could expect to detect less than one photon per year from these sources.

Historically, there have been two types of satellite gamma-ray detectors: spark chamber detectors and scintillator detectors. Spark chambers, first used in balloon-borne CR detectors, appeared on the satellite carrying the instrument SAS-2 (1973), the satellite bearing the COS-B instrument (1975-1982), and the EGRET detector on the Compton Gamma Ray Observatory (CGRO) satellite (1991-2000). COMPTEL, also on the CGRO, was a scintillator detector [73].

A spark chamber detector consists of a tracker, a trigger, a calorimeter, and an anticoincidence detector. The tracker is made up of stacked metal plates inside a closed, gas-filled chamber, alternately electrically connected with one set grounded. The other set has high voltage applied when a charged particle enters the chamber, as happens when a gamma ray interacts with the plates and produces an electron/positron pair. The ionization caused by the passing charged particles produces a spark discharge between the plates, and thus the paths of the particles can be tracked. The trigger is responsible for initiating the high voltage in the tracker plates, and is activated by an electron emerging from the spark chamber. A high voltage difference cannot be maintained in the spark chamber because spontaneous discharges would occur, invalidating the purpose of the chamber. The trigger consists of two plates separated by

a distance sufficient to reject upward-traveling particles. The calorimeter is present to completely absorb electrons from the spark chamber in order to measure their energy. Lastly, the anticoincidence detector surrounds the rest of the instrumentation, and while it registers the arrival of a charged particle, it has a very small interaction cross-section for neutral gamma rays. This allows free charged particles entering the detector to be distinguished from charged particles created inside the detector by the decay of a gamma ray [73]. Most modern space-based gamma-ray telescopes are based on this design.

The basic components of a scintillator detector are a material which emits light when it interacts with charged particles via either Compton scattering or the photo-electric effect, and a PMT. They are commonly used in Compton telescopes, where two scintillators are present. A gamma ray enters the first scintillator, where it undergoes Compton scattering. In the second scintillator, which is surrounded by an anti-coincidence detector, it is absorbed [73].

Currently operating gamma-ray satellites include INTEGRAL (launched 2002), which is sensitive to photons from 15 keV to 10 MeV [199], AGILE (launched 2007), which is sensitive to photons from 50 MeV to 30 GeV [200], and *Fermi* (launched 2008, formerly known as GLAST), which is sensitive to photons from 20 MeV to 300 GeV [201]. Swift, an X-ray/UV telescope launched in 2004, carries the Burst Alert Transient (BAT) instrument, designed to quickly detect and precisely locate gamma-ray bursts (GRBs), as well as the X-Ray Telescope (XRT) and Ultraviolet/Optical Telescope (UVOT), used for follow-up observations of GRBs [202, 203].

Since *Fermi* is the major operating gamma-ray satellite at the time of this writing, I will discuss it in more detail. *Fermi* carries two instruments: the Large Area Telescope (LAT), and the Gamma-ray Burst Monitor (GBM). The LAT is the main instrument, observing the entire sky once every $\sim$3 hours with a field of view covering 2.4 steradians. At 1 GeV, the effective area is $\sim$8000 cm^2, the angular resolution is $\sim0.5^\circ$, and the energy resolution is $\sim0.1^\circ$ (see Figure 4.10). Similar to earlier spark

chamber detectors, the LAT is a pair-conversion telescope with an additional calorimeter and anti-coincidence detector; however, the LAT has a solid state particle tracker consisting of silicon strip detectors interwoven with tungsten as a converter material [201] (see Figure 4.11).

4.3 Ground-based Particle Detectors

4.3.1 Water Cherenkov Telescopes

A different method of observing VHE gamma rays is used by detectors like Milagro and its successor, the High Altitude Water Cherenkov observatory (HAWC). These detectors are water Cherenkov telescopes, which consist of large, deep pools or tanks filled with water and covered with light-tight material, with PMTs arrayed on their interiors. They are at high enough altitude that particles from air showers can penetrate directly into the tanks, where they then produce Cherenkov radiation which is detected by the PMTs. These are all-sky monitors rather than pointed instruments, and have a high duty cycle (>95%). Milagro, located in New Mexico at an altitude of 8600 ft (2.62 km), consisted of a 60 m x 80 m x 8 m pool surrounded by ∼170 cylindrical "outrigger" tanks of 2.4 m diameter and 0.91 m height [205]. It was operational from 1999 until 2008, and had a peak sensitivity near 1 TeV [206]. HAWC, currently under construction in Mexico at an altitude of 4.1 km, will consist of 300 cylindrical tanks of 7.3 m diameter and 4.5 m water height (see Figure 4.12). It is expected to be completed in 2014 [207].

Milagro was the first water Cherenkov telescope to succesfully detect sources. Although water detectors are significantly less sensitive than IACTs[1], and have much worse angular resolution[2], their light-tight design allows them to operate during daylight hours. This gives them a much better chance to see transient events (e.g. GRBs,

[1] The Crab Nebula, e.g., was visible to Milagro at a statistical significance of 5σ in ∼18 months [205], in comparison to ∼1 minute for VERITAS

[2] 0.75° [205] for Milagro vs. 0.1° for VERITAS [185]

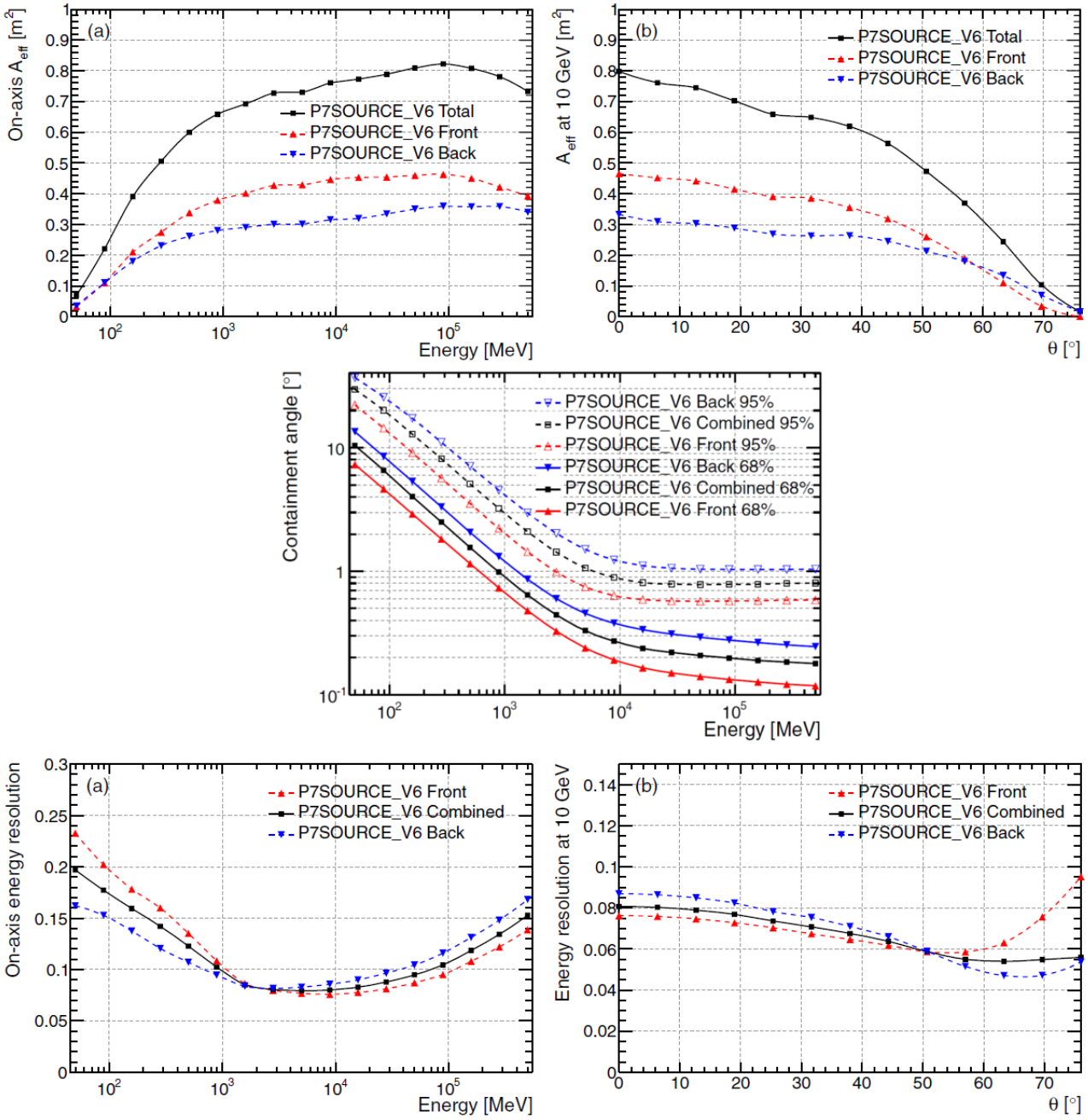

Figure 4.10: Figures 31, 57, and 69 from [204]. ©AAS. Reproduced with permission. Top: "On-axis effective area as a function of the energy (a) and angular dependence (b) of the effective area at 10 GeV for the P7SOURCE class." Center: "68% and 95% containment angles as a function of energy for the P7SOURCE_V6 event class." Bottom: "Energy resolution as a function of energy on-axis (a) and incidence angle at 10 GeV (b) for the P7SOURCE_V6 event class." P7SOURCE_V6 refers to the current version of the instrument response function.

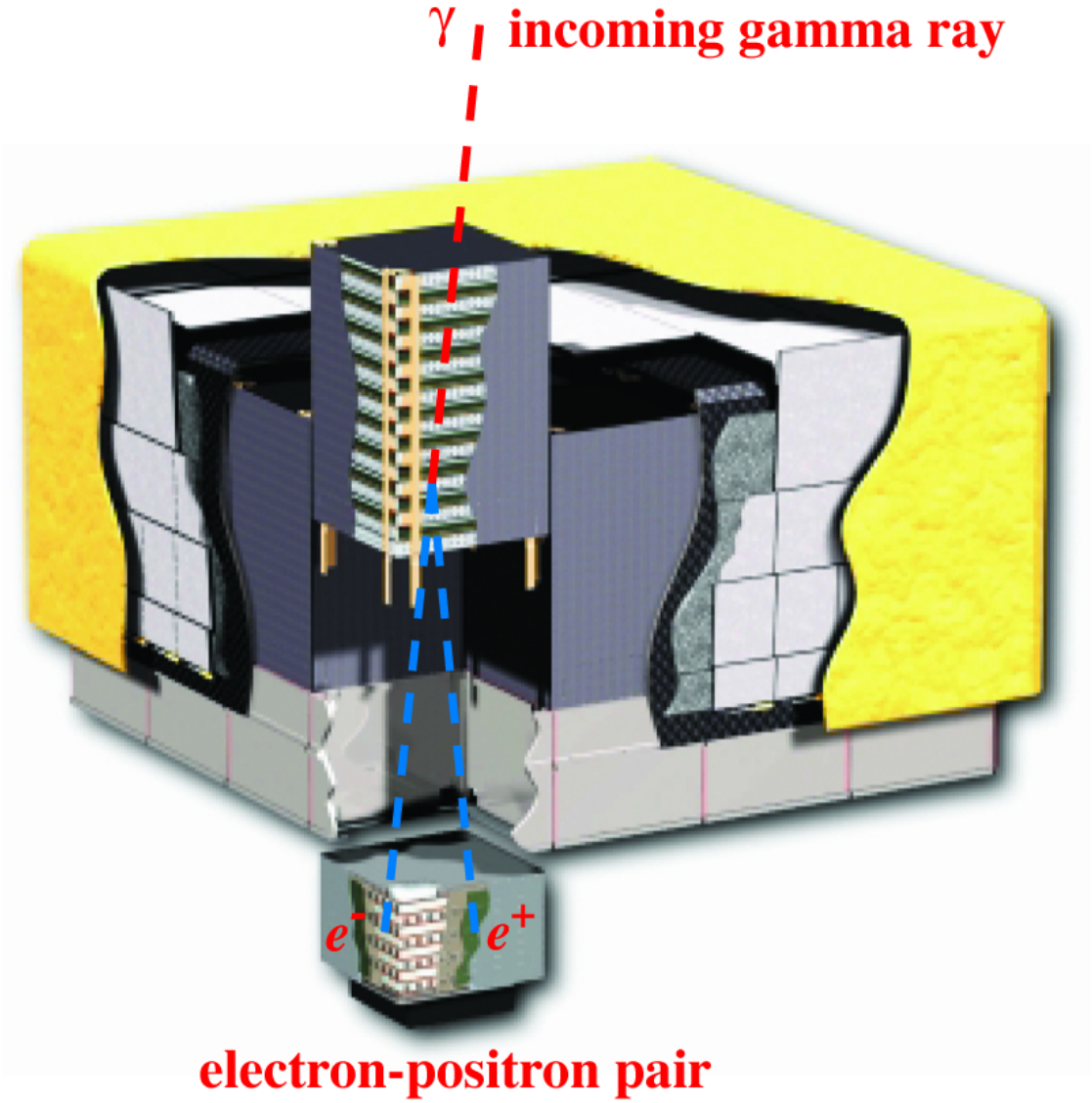

Figure 4.11: Figure 1 from [201]. ©AAS. Reproduced with permission. "Schematic diagram of the LAT. The telescope's dimensions are 1.8m × 1.8m × 0.72 m. The power required and the mass are 650 W and 2789 kg, respectively."

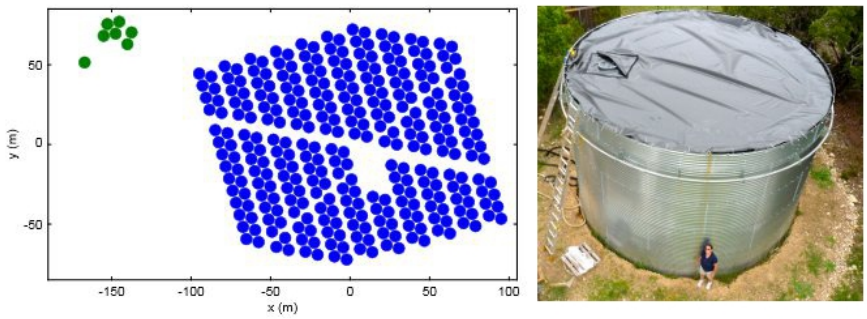

Figure 4.12: Left panel: Figure 1 from [207]. "HAWC layout. The 7 upper left tanks are part of the VAMOS test array," a preliminary array of water Cherenkov telescopes at the HAWC site. Right panel: from [208]. "Steel water-Cherenkov tank used in HAWC."

blazar flares) than dark-sky, pointed IACTs have. As the first all-sky instrument sensitive to TeV energies, Milagro also completed the first survey of the Galactic plane at these energies (see Figure 4.13). This provided a good list of possible targets for follow-up observations at higher angular resolution with next-generation IACTs.

4.3.2 Extensive Air Shower Arrays

The ARGO-YBJ (Astrophysical Radiation with Ground-based Observatory at YangBaJing) air shower array is located at the Yangbajing Cosmic Ray Laboratory in Tibet, China, at an altitude of 4300 m a.s.l. This detector consists of a central carpet of Resistive Plate Counters (RPCs) covering an area of 5772 m^2. This central carpet is surrounded by a guard ring of RPCs partially covering an additional area of 5228 m^2 [210]. It has an energy threshold of ∼100 GeV, and an angular resolution on the order of 1° [211]. This instrument is primarily suited to the study of air showers from cosmic rays [210], although a full sky survey of gamma-ray sources is also achievable. Note, however, that ARGO-YBJ has much lower sensitivity to gamma-ray sources than modern IACTS; in five years of observations, they detected six sources with statistical significance greater than 5σ [212].

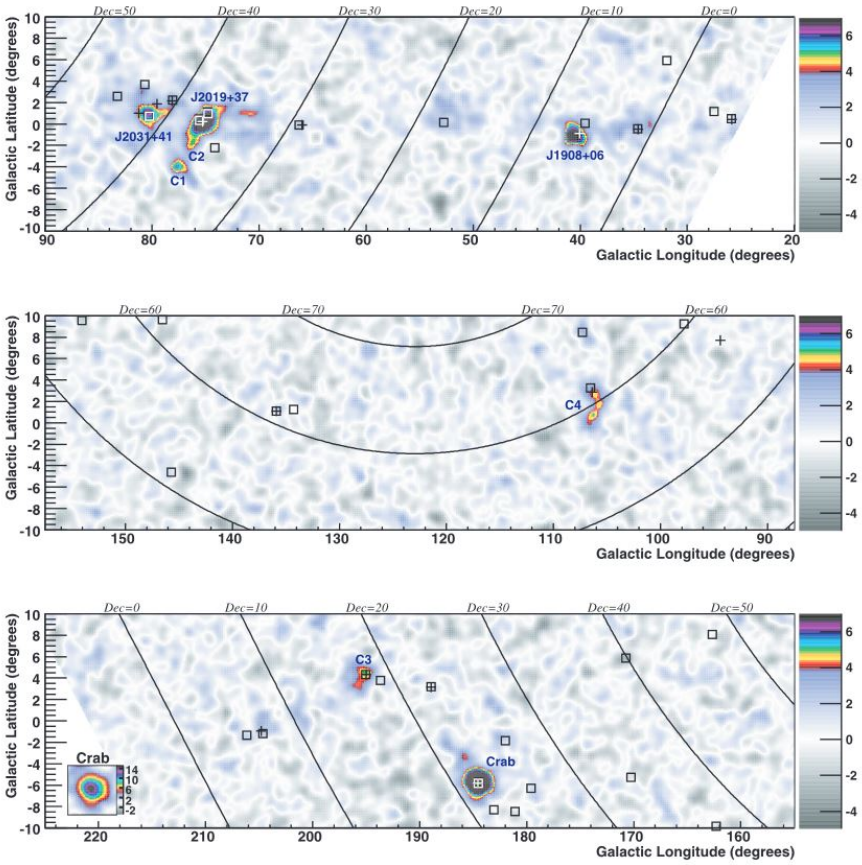

Figure 4.13: Figure 1 from [209]. ©AAS. Reproduced with permission. "Significance map of the Galactic plane. The color code shows the pretrial significance in this PSF-smoothed map. The maximum positive value of the color code saturates at 7σ, although three of the gamma-ray sources are detected with much higher statistical significance. The Crab image is inset with the same x- and y-scale in the bottom left, as an indication of the PSF. Boxes (crosses) indicate the locations of the EGRET 3EG (GeV) sources."

The Tibet-III air shower array also operates at Yangbajing. Since 1999, it has been operating with 533 scintillation detectors covering an area of 22,050 m^2. In 2000-2003, the detection area was increased to 36,900 m^2 with the addition of 256 PMTs to the interior of the array [213][214]. The energy threshold of this array is $\sim$1.5 TeV for protons and $\sim$1.0 TeV for gamma rays [215], with sensitivity extending past 10^{17} eV [213], and the angular resolution is $\sim 1^\circ$ at 3 TeV [215]. This instrument also is well-suited to studying the cosmic ray spectrum, especially in the vicinity of the knee, and serves as a full-sky survey instrument for gamma rays. Tibet-III is also far less sensitive to gamma rays than current IACTs; in $\sim$3.5 years of observations, they detect the Crab Nebula at a statistical significance of 6.3σ [214].

Chapter 5

CHERENKOV TELESCOPE DATA ANALYSIS

As clever and complex as the detection technique and hardware are for a Cherenkov telescope array, they are meaningless unless the data that is collected can be analyzed. To achieve this, VERITAS maintains two independent software analysis packages which are coded differently and use slightly different calculation methods. In order for a result to be published, the collaboration requires agreement (within errors) between the two analyses. The analysts discuss beforehand what data to analyze, and which cuts to apply to the data (this will be explained in Sections 3 and 4 of this chapter), and then carry out their analyses independently. This chapter will explain what data analysis consists of. It is important to keep in mind during the following discussion that the cosmic ray (CR) flux observed is thousands of times greater than the flux of gamma rays, so the analysis is designed to remove as many CRs as possible while simultaneously keeping as many probable gamma rays as possible.

5.1 Data Quality Selection

During standard operations, VERITAS collects data in increments of a set time length. Each of these increments is referred to as a *run*. During the era the data in this work was collected, the standard length of a run was 20 minutes; it has since been increased to 30 minutes to reduce the time spent slewing the telescopes to different locations on the sky.

Once a list of all the data on a particular source during a particular timeframe has been compiled, any runs with significant problems are rejected. These include hardware issues affecting multiple telescopes, poor weather, or any other issue that

renders the data unusable. For many studies, data taken with three of the four VERITAS telescopes still has sufficient accuracy in the reconstruction of the air shower to be useful (air shower reconstruction will be explained in Section 3 of this chapter). For some studies, such as analysis of very weak sources or complex fields with many bright stars or multiple gamma-ray sources, only four-telescope data is desirable; in this case, runs with issues affecting any telescope are rejected. Generally, runs taken with only one or two telescopes fully functional do not have high enough shower reconstruction accuracy to draw strong conclusions about the source, so they are not used (and, in fact, are only very rarely taken; more than 90% of runs are taken with 4 telescopes, and more than 99% are taken with ≥ 3 telescopes). If some significant portion, but not all, of a run is usable, the analyst may choose to apply time cuts to the data during the analysis (e.g., if clouds moved through the field of view during 2 minutes of an otherwise fine 20 minute run).

Evaluation of what constitutes poor weather for our purposes is actually a rather difficult task. VERITAS approaches this in several ways. First, for each run taken, the observers on site assign a subjective letter grade to the weather (ABCDF). Second, VERITAS uses a system of three far infrared (FIR) cameras to monitor cloud cover via changes in temperature. Two of these are mounted directly on two of the telescopes, so their field of view overlays the pointing direction of each observing run, and the third, with a wider field of view, is fixed on zenith. These cameras are particularly useful in identifying runs where thin, high clouds that are difficult to see with the naked eye are present. Figure 5.1 shows examples of good weather and poor weather FIR data. Note that the letter grades assigned by the observers, while qualitative, are still extremely useful; a smooth FIR trace may indicate continuous cloud cover, not clear skies. In addition to the FIR data, VERITAS also has a LIght Detection And Ranging (LIDAR) system to measure atmospheric temperature, and an all-sky optical telescope for viewing cloud cover. Lastly, although not intended for the purpose, the L3 trigger rates (which are comprised almost entirely of CR background events) taken in context with other weather information may also provide some indication of sky conditions;

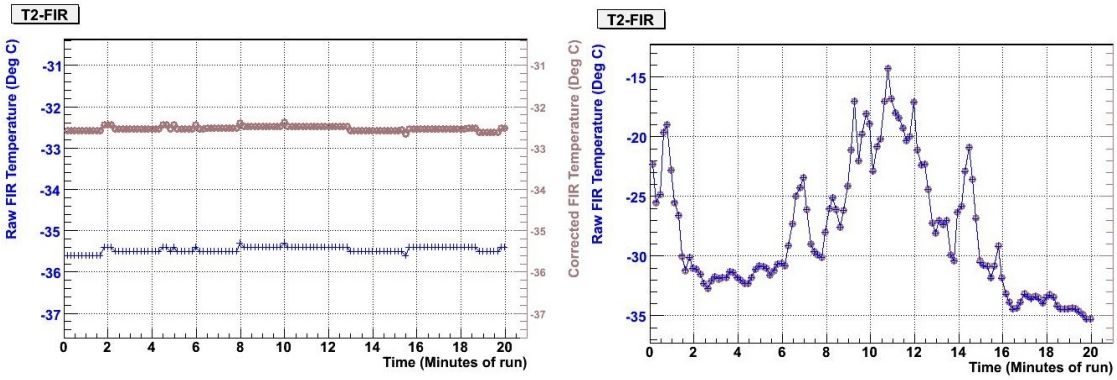

Figure 5.1: Left panel: FIR data taken during clear sky conditions. Right panel: FIR data taken while clouds moved through the field of view. The corrected FIR values represent the same dataset as it would be at 90° elevation and 20° C ambient temperature.

clouds result in lower and unstable L3 rates, so a large deviation from clear-sky rates for the source in question would be an indication that the data quality for a given run may not be good.

5.2 Calibration

5.2.1 Flat-Fielding

VERITAS requires calibration data to be taken each night of observing, analogous to flat-fielding for an optical telescope. This is currently accomplished by means of a light emitting diode (LED) flasher mounted on each telescope frame in front of the camera. The flasher contains seven LED bulbs, and has a diffuser attached to produce even, near-simultaneous illumination for each PMT in the camera, allowing for measurements of pulse heights and response timing, which vary by individual pixel[1]. With this information, the voltage for each PMT can be adjusted to produce uniform average pulse heights, and timing adjustments calibrated between pixels. Typically, a

[1] The voltage in each PMT is different, and so the transit times in the PMTs vary. Additionally, the lengths of the cables connecting the PMTs to the Flash Analog-to-Digital Converters (FADCs) are not identical, so timing and attenuation differences are introduced.

5-minute flasher run is taken each night, during which the flasher is pulsed at 300 Hz, although both the frequency and the duration of the flasher run can be controlled by the observers.

The LEDs are housed in modified Maglite flashlight cases with an opal diffuser replacing the flashlight lens. The peak of the LED light is at 465 nm, each light pulse is about 10 ns long, and the flasher cycles through eight intensity levels (0 LED bulbs illuminated, 1 bulb illuminated, etc.), providing calibration data for both the high- and low-gain FADC signal paths (see Chapter 4, Section 4.1.3.6 for a description of high- and low-gain paths) [216]. After adjusting the voltage on each PMT, the distribution of relative gains over all 499 PMTs in the camera for each telescope has a root mean square (RMS) value of ∼0.05-0.07. As can be seen in Figure 5.2, the distribution of relative gains for each telescope is quite narrow. Figure 5.3 shows an example of the distribution of charge, the mean of which is the relative gain, in one PMT as determined from a flasher run.

Until September 2010, a 337 nm nitrogen laser was used for calibration measurements instead of the flasher. The single laser signal was split and sent to each telescope via fiber optic cables with diffusers on the ends. This introduced variation in the intensity of light seen by each telescope due to the different length cables required to reach each telescope. This effect was accounted for in the analysis. Much of the data in this work was taken while the laser was the standard calibration tool.

5.2.2 Pedestals

Even in a remote part of Arizona, VERITAS is still affected by general night sky background (NSB) light. This is produced by natural sources, like the moon and ambient starlight, and by light pollution from artificial sources. To complicate things further, the amount of NSB varies with time and with telescope pointing location. At the VERITAS site, the average NSB photon flux above 60° elevation was measured to be $\sim 3 - 4 \times 10^{12}$ photons/s/sr/m^2 [217].

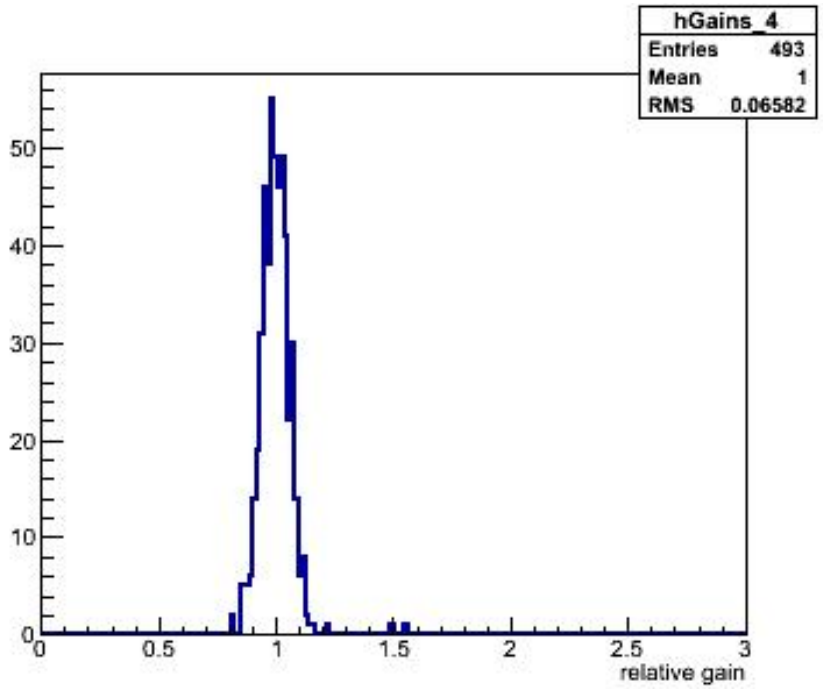

Figure 5.2: An example of a relative high-gain distribution for one telescope, T4 (see Chapter 4, Section 4.1.3.6 for a discussion of high and low gain). The histogram measures the number of PMTs along the y-axis, and relative gain along the x-axis. During this particular run, 6 PMTs on T4 were disabled, so only 493 PMTs were included in the histogram.

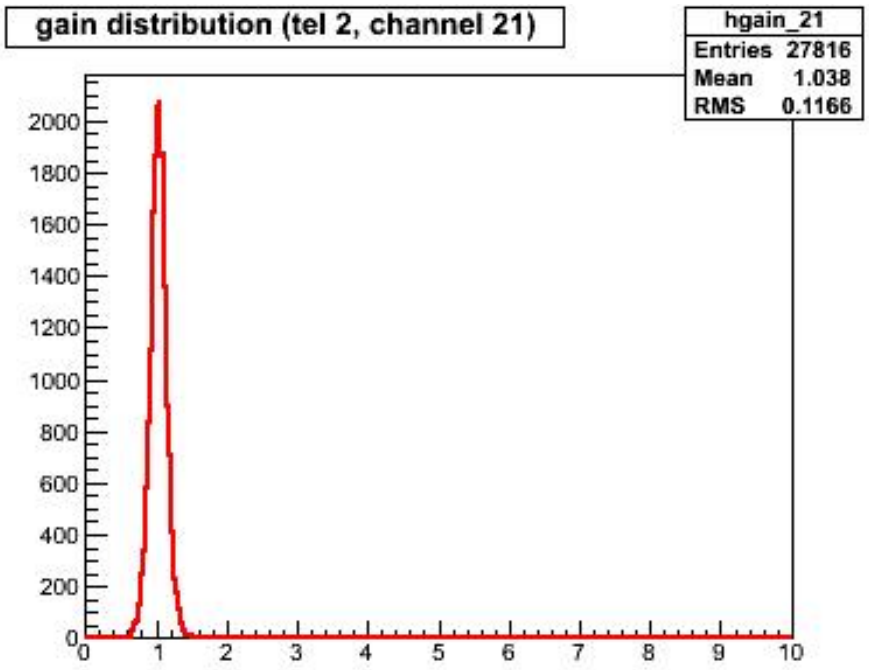

Figure 5.3: An example of the distribution of charges measured in a single PMT during a flasher run. The voltage of each PMT is adjusted to produce a relative gain (ratio of a single flasher pulse's charge in that PMT to the average charge from all flasher pulses in that PMT) centered at 1. The y-axis on this histogram denotes number of flasher pulses, and the x-axis is the charge produced by each pulse.

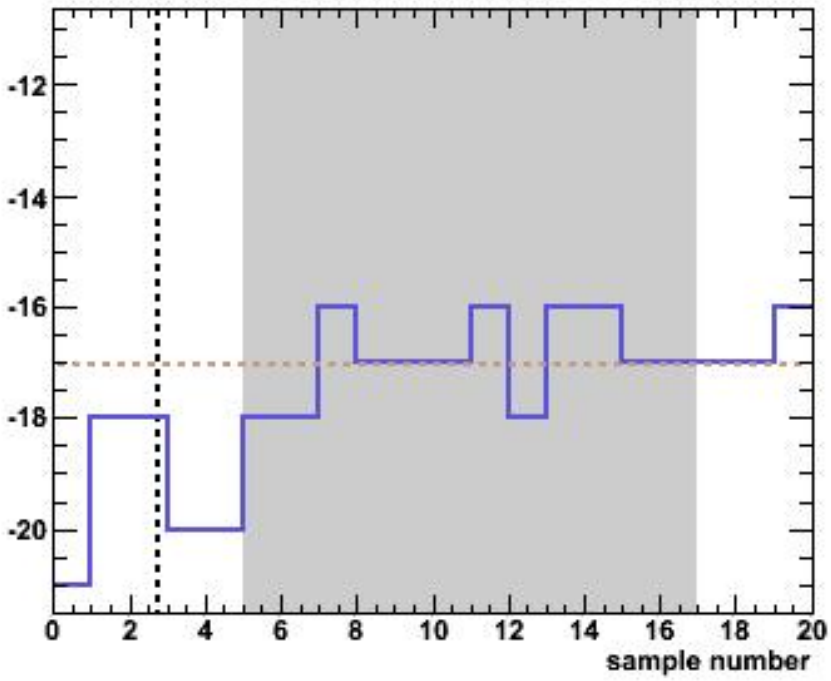

Figure 5.4: An example of a pedestal event FADC trace. The y-axis is given in digital counts, which can be converted to a number of photoelectrons, and the x-axis is given in FADC samples.

To account for this fluctuating NSB light, a constant offset voltage (∼16 digital counts) is added to the PMT signal. This allows both positive and negative fluctuations around the artificial baseline (due to Poisson noise inherent in the measurement) to be measured when the only signal in the PMTs is from NSB (see Figures 5.4 and 5.5). The voltage in a PMT receiving only NSB light is known as the *pedestal*, and the standard deviation of the signal around the pedestal value is known as the *pedestal variance*, or *pedvar*. The PMT output pulses are in negative voltages, so the pedestal offset is also negative. To calculate the pedestal and *pedvar*, a 1 Hz artificial trigger is sent to all telescopes to read out (by definition, pedestal events do not trigger the system).

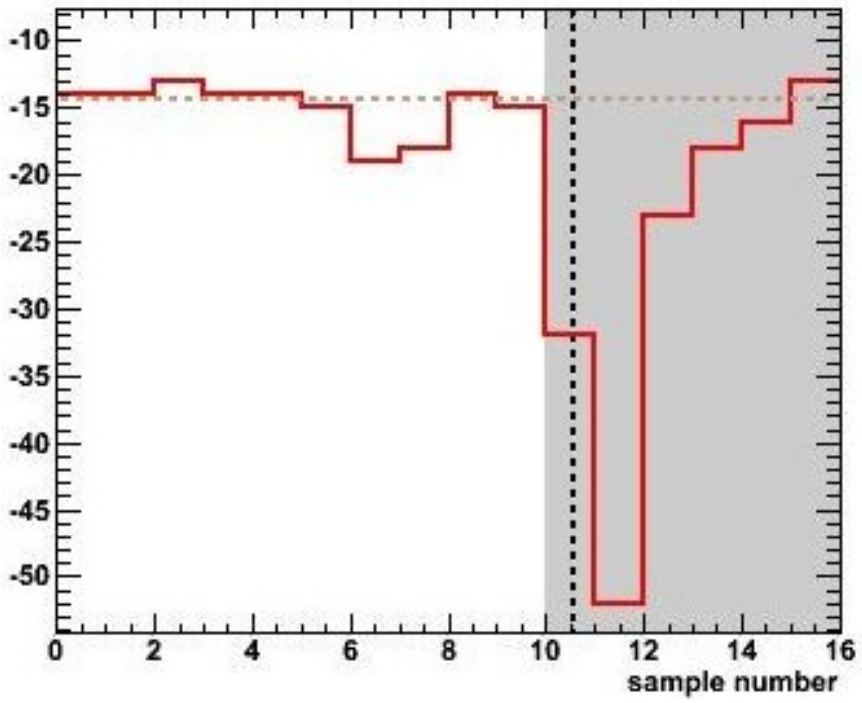

Figure 5.5: An example of a bright Cherenkov event FADC trace. Again, the y-axis is given in digital counts, which can be converted to a number of photoelectrons, and the x-axis is given in FADC samples.

5.2.3 Absolute Calibration

The flasher is also used to measure the response of the instrument to single photoelectrons (p.e.). This is how the absolute calibration of the instrument is determined. The number of p.e.s generated in the PMTs is proportional to the amount of Cherenkov light observed in an air shower, which, together with the impact distance to the shower, allows the energy of the initiating particle or photon to be determined. Thus, it is necessary to know the response of the FADCs to a single p.e. in order to quantify the relationship between the observed pulses and their physical causes.

To make this measurement, a plate perforated with tiny holes aligned with each PMT is placed over each camera to severely limit the amount of light entering the PMTs (see Figure 5.6), and a flasher run is taken. By comparing histograms of charges in each PMT for the dimmest flasher illumination levels, and fitting these histograms

with Gaussian distributions, the 0-p.e. (pedestal), 1-, 2-, 3-, and 4-p.e. peaks in the overall charge distribution can be extracted [216].

The above procedure is carried out twice, once with the cameras set to their nominal high voltage value, and once with them set to 110% of the nominal high voltage. At higher voltage, the single p.e. peaks are shifted further from the pedestal value, and are therefore easier to resolve and measure more precisely. In order to scale these values to their value under nominal high voltage for comparison, the voltage dependence of the gain of the PMT is used; for small changes in voltage, the gain can be described by [218]:

$$G = G_0\left(\frac{HV}{HV_0}\right)^{\alpha}$$

where G is the increased gain of the PMT, G_0 is the gain at nominal high voltage, HV is the increased high voltage, HV_0 is the nominal high voltage, and α is a constant determined from the below fitting procedure for each PMT. The gain of a PMT can be estimated from the charge distribution produced by the full 7-LED intensity level of the flasher; the gain at nominal high voltage, the nominal high voltage, and the increased high voltage values are known. Thus, a plot of these values demonstrates the power-law dependence, and provides a value for α. This value of α is then used to scale the single p.e. measurements taken at increased voltage to their values at nominal voltage; the two values at nominal voltage are then compared for verification.

Lastly, from these measurements of the positions of the 1-p.e., 2-p.e., etc. peaks, a correlation between digital counts (d.c.) and p.e. can be determined. This is how VERITAS is able to determine how many p.e. produced an observed pulse of a given size in the FADCs. The relationship is 1 p.e. = 5.3 d.c., which produces a pulse height of 2.4 mV after preamplification and signal propagation through the coax cable to the FADCs [194]. Note that these are average values over all PMTs; for an individual PMT, the pulse from a single p.e. may differ from this value significantly.

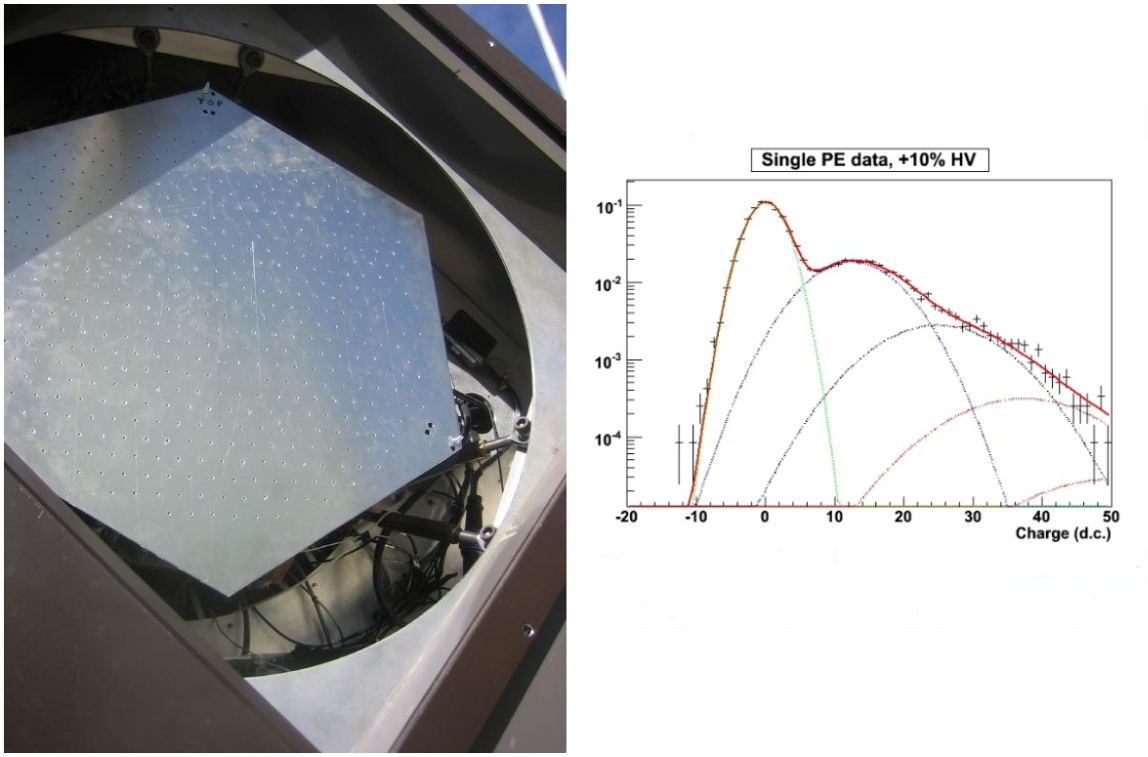

Figure 5.6: Left panel: the "holey plate" used for single photoelectron (p.e.) measurements, as installed on one of the VERITAS cameras. Right panel, adapted from [219]: histogram showing peaks for 0 (pedestal event), 1, 2, 3, and 4 p.e.'s. The overall function is shown as a solid red line, and the component functions are shown as dotted lines in green, blue, black, and red. The y-axis shows the number of events, normalized so the total area under the curve equals 1, and the x-axis is charge in digital counts.

5.2.4 Simulations

In order to determine if our understanding of the instrument and the data it produces is correct, we compare the real data to simulations. Every portion of an air shower's journey is modeled in these simulations, from the initiating particle's first interaction with the atmosphere through the responses of the telescope optics and electronics. The simulations' purpose is two-fold: if the physics we model describes the observations accurately, we can have greater confidence in our understanding of the processes at work; additionally, once we have confidence that the instrument is well-modeled, we can simulate either gamma rays or CRs to determine the instrument's response to them, and use the results to help us differentiate between gamma rays and CRs in real data.

In the VERITAS simulation studies, air showers are modeled using the KASCADE [220] and CORSIKA [221] shower generators. Multiple simulation packages are used to avoid systematic effects that may arise from a single package [222]. For the analysis of data on Tycho's SNR described in this work, CORSIKA simulations were used. KASCADE is a software package first produced in 1989 by current VERITAS collaborators M. Kertzman and G. Sembroski; however, it is a general-use (i.e., not specific to VERITAS) air shower simulator designed for IACT studies. It uses Monte Carlo models of air showers resulting from gamma rays and CRs. CORSIKA is a software package produced externally to VERITAS and used throughout the field of CR studies; it contains Monte Carlo simulations of several detailed models of air showers from various species of CR primary, as well as gamma-ray air showers. Both packages model the air showers' interactions with the atmosphere, including the Cherenkov light created in the process (see Chapter 3, Section 3.3 for a discussion of air showers).

Within CORSIKA, VERITAS uses the QGSJet interaction model for initiating particles with energies above 500 GeV, and the FLUKA model for energies below 500 GeV. We model air showers induced by gamma rays, protons, and helium nuclei from 50 GeV (30 GeV for protons) to 30 TeV at zenith angles ranging from 0° to 65°. Simulated showers are thrown randomly over a circular area of 600 m radius centered on the center

of the telescope array [222]. Measurements of the atmosphere at the VERITAS site are input to the air shower simulations. Until 2010, the U.S. standard atmospheric model was used to model the atmosphere; currently, we use winter and summer atmospheric profiles based on radiosonde data taken by the University of Arizona, Tucson ($\sim$ 60 km from the observatory).

The response of the instrument to the air showers is also modeled using multiple packages: ChiLa, KASCADE, and GrISUDet [223]. For the analysis of the data on Tycho's SNR described in this work, GrISUDet simulations were used. All of these packages include models of the telescope optics, the camera, and the trigger system. Within models of the optics, the mirrors' alignment accuracy and reflectivity are accounted for. To simulate signals in a PMT, real measurements of the system's response to single p.e.'s are input; simulated pulses are produced by summing recreated single p.e. pulses and applying the appropriate amplitude and time jitter. The quantum efficiencies of the PMTs are included in the model, as are the geometrical and collection efficiencies, the electronic noise, and the loss due to signal transmission. The simulated pulses are then digitized with 2 ns sampling to reproduce the sampling frequency of the real FADCs [222]. Night sky background light is also modeled in a range of brightnesses, spanning from 75-1000 p.e./ns/m^2/sr [223], and added to the simulated signal. Typical values for an extragalactic pointing are $\sim$150 p.e./ns/m^2/sr, and are 200-250 p.e./ns/m^2/sr for a pointing along the galactic plane; higher values reflect various levels of moonlight. Finally, the trigger system is simulated, with the performance parameters and requirements of the real system as input. Although a simplified model of the constant fraction discriminator (CFD) is used (see Chapter 4, Section 4.1.3.5 for a description of the CFD), the pattern trigger and array triggers are accurately represented [222]. The final output files from this simulation chain are .vbf files (see Chapter 4, Section 4.1.3.6), identical to the format for real data. The simulations can then be analyzed using the same software that is used for actual observations.

From simulated gamma rays and CRs, lookup tables can be produced. Lookup tables are histograms of the parameters of the images produced by gamma-ray-induced

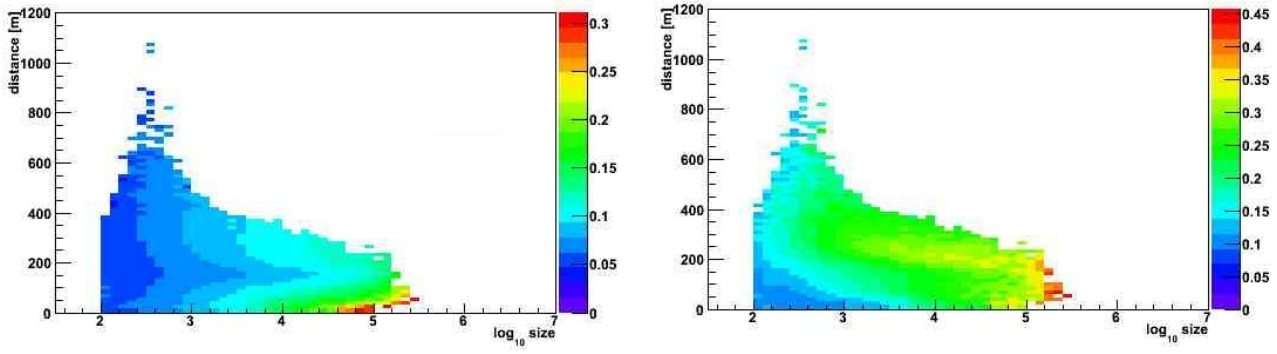

Figure 5.7: An example of lookup tables for Hillas parameters "width" (left) and "length" (right). The color scale indicates the median value of the parameter being shown, in degrees. The X-axis indicates the *size* of the image (shown on a $\log_{10}$ scale), and the Y-axis indicates the distance from the telescope to the shower impact point.

air showers of various zenith angles, impact distances, and energies (see Figure 5.7 for an example of lookup tables, and see Section 5.3.2 of this chapter for a discussion of image parameters). From these simulated gamma rays, and the simulated response of the instrument, one can determine values of various parameters below which mainly gamma rays survive, and above which mainly CRs can be cut. These values are optimized to keep the maximum number of gamma rays while simultaneously cutting the maximum number of CRs. These cuts, which will be described in the following section, are then applied to real data.

5.3 Shower Reconstruction

5.3.1 Image Cleaning

As discussed in Chapter 3, both gamma rays and cosmic rays (CRs) produce atmospheric air showers and Cherenkov radiation. Thus, gamma-ray astronomers must first identify which air showers are likely caused by gamma rays before proceeding with further data analysis. This is made more challenging by the fact that there are 10^3 - 10^4 times more CRs entering the atmosphere than gamma rays [73].

Fortunately, the images produced by gamma rays are generally smaller and more compact than those produced by CRs. As mentioned in Chapter 3, electromagnetic atmospheric air showers are more tightly bunched around the path of the initiating photon than CR air showers are around the path of the initiating particle. This is because the secondary particles created in a hadronic air shower are emitted at wider angles than Cherenkov photons are emitted from an electromagnetic air shower. Figure 5.8 illustrates this effect. Examples of camera images consistent with electromagnetic and hadronic air showers are shown in Figure 5.9. The image produced by a hadronic air shower is larger and more irregular than the one possibly produced by an electromagnetic air shower. The development of an air shower across the camera is illustrated in Figure 5.10.

Once events have been recorded, a process which was discussed in Chapter 4, cuts are applied to the data. These cuts primarily separate images likely produced by electromagnetic air showers from those likely produced by hadronic air showers, but also affect the energy threshold of reconstructed gamma rays. Standard VERITAS analysis cuts are optimized for a hypothetical source with a Crab Nebula-like spectrum (spectral index of ~ 2.5) and a flux 5% of that of the Crab (the Crab Nebula is the brightest steady gamma-ray source in the Northern hemisphere, and so is often used as a standard), but for sources expected *a priori* to differ significantly from this template, cuts can be optimized for other scenarios. The standard cuts require the following characteristics for an event to be considered as an image for analysis:

- At least 4 neighboring PMTs must contain non-pedestal FADC traces, defined as a signal at least 5 times the *pedvar* value. PMTs contiguous to these must contain a signal at least 2.5 times the *pedvar* to be considered part of the image.
- The *size* of an image, or the integrated charge over all the pixels which comprise the image, must be at least 500 digital counts. This correlates to the brightness of the image, and hence the energy of the initiating gamma ray or CR.
- The *loss*, or the fraction of the total integrated charge of the image occurring within pixels at the edge of the camera, must be no more than 20%. This prevents the inclusion of images where a large portion of the image is off the edge of the camera.

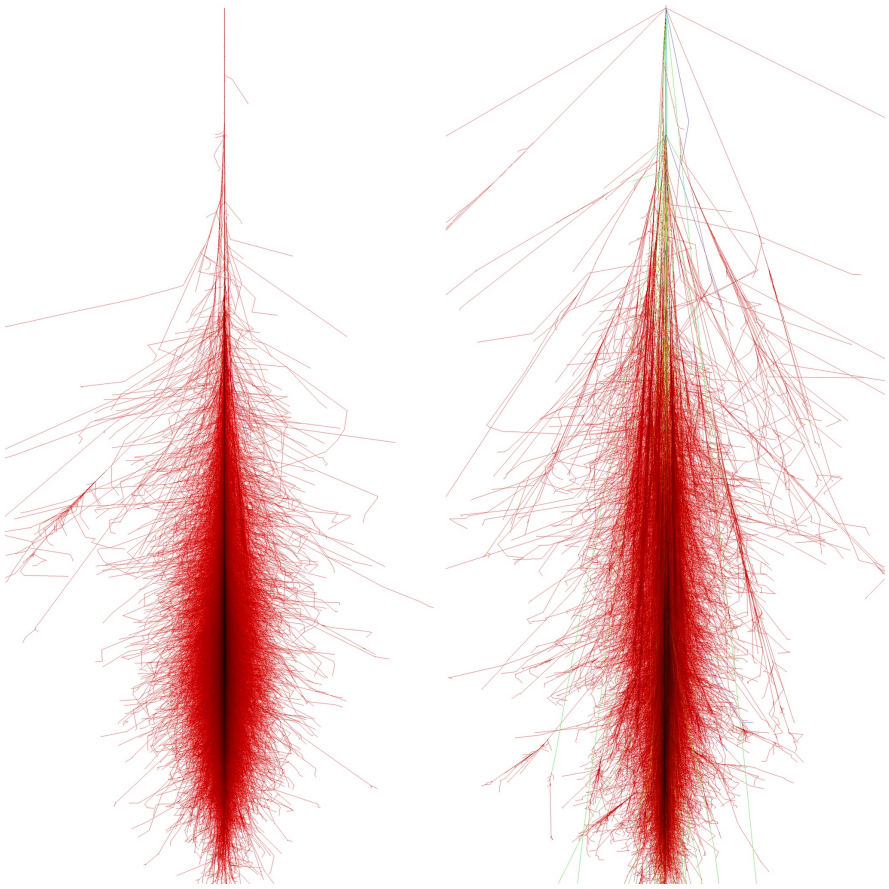

Figure 5.8: CORSIKA simulations illustrating a shower initiated by a 1 TeV photon, left, and a 1 TeV proton, right [224]. Red tracks indicate electrons, positrons, and gamma rays. Blue tracks indicate hadrons. Green tracks indicate muons. All showers simulated have a fixed first interaction altitude of 30 km. These images have a vertical axis ranging from 0 to 30.1 km, and a horizontal axis ranging ± 5 km from the shower core. For electrons, positrons, and gamma rays, a minimum energy of 0.1 MeV was required for plotting. For muons and hadrons, the threshold was 0.1 GeV.

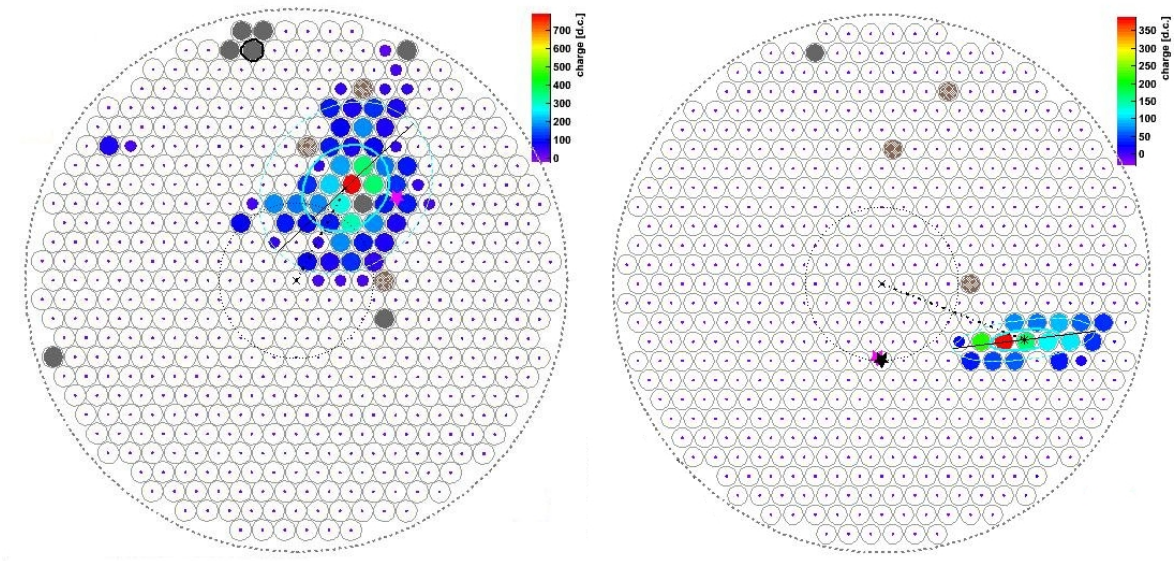

Figure 5.9: Example of an image produced by a hadronic (CR) air shower (left) and an image possibly produced by an electromagnetic (gamma-ray) air shower (right). The color scale indicates the charge contained in each PMT, measured in digital counts (d.c.).

- Lastly, to take advantage of the benefits of using an array of telescopes, it is required that at least 2 telescopes record a given event.

The charge in a PMT is determined by integrating over the pulse in the FADC window. In order to define the integration window, a double-pass method is employed. The first pass identifies the time T_0 at which the pulse reaches 50% of its maximum amplitude. The second pass places a pre-determined integration window over the pulse, usually either 7 or 12 samples wide (each sample is 2 ns). The starting position of this window is determined using the *time gradient* of the image; the T_0 of the pulse for each PMT along the major axis of the image (the major axis will be defined in the following section) is fit to a straight line, the slope of which is the *time gradient* for the image [225].

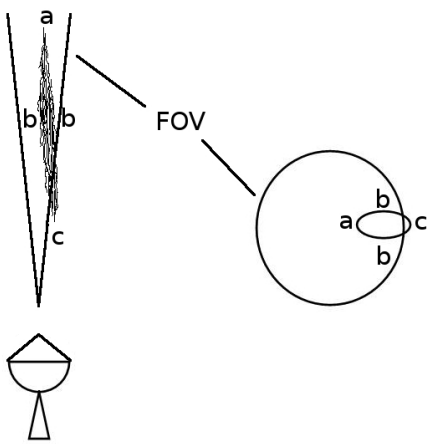

Figure 5.10: Reproduced from figure 2.7 of [73]. A cartoon illustrating the development of the air shower across the camera. "The geometry of the Cherenkov light images from an air shower (on left) as recorded by a camera on an atmospheric Cherenkov telescope (on right). The shower is parallel to the optic axis of the telescope and is inverted here. The light in the image comes from the top of the shower (a), from the middle (b) and from the bottom (c)." *FOV* indicates the field of view of the camera. Note that this illustration is not to scale; the placement of the ellipse in the camera does not accurately reflect the distance from the shower impact position to the telescope, nor does the size of the ellipse reflect the size of the shower.

5.3.2 Image Parameterization

Once an image has passed the applied quality selection cuts for image cleaning, one can identify the "Hillas parameters" for that image [81]. These parameters are then used to define a two-dimentional Gaussian distribution (the cross-section of which is an ellipse). The basic parameters, illustrated in Figure 5.11, are defined as follows:

- Length: RMS spread of light along the semi-major axis of the ellipse. Correlates to longitudinal shower development in the atmosphere.
- Width: RMS spread of light along the semi-minor axis of the ellipse. Correlates to lateral shower development in the atmosphere.
- Distance: Distance of the image centroid to the source position, in degrees.
- Alpha: Angle between the major axis of the ellipse and a line drawn from the image centroid to the source position.

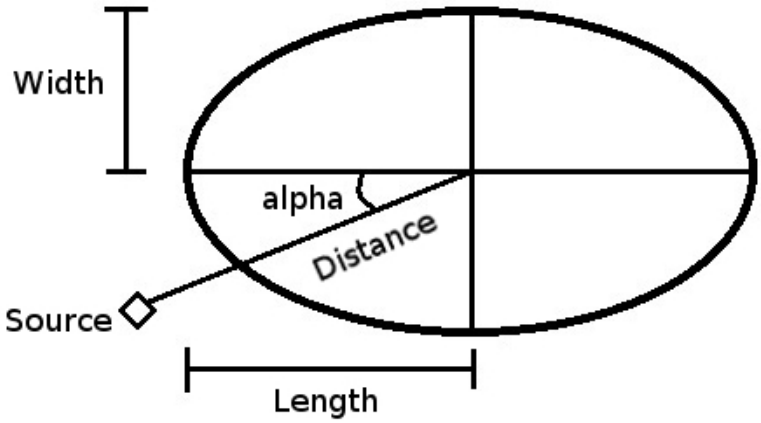

Figure 5.11: A cartoon illustrating the main Hillas parameters of an image. Modeled after figure 11 from [227].

Other parameters may also be calculated, but these are the most crucial to the analysis. Mathematically, the width and length are defined as follows [226]:

$$w = \sqrt{\frac{\sigma_{x^2}^2 + \sigma_{y^2}^2 - s}{2}}$$

$$l = \sqrt{\frac{\sigma_{x^2}^2 + \sigma_{y^2}^2 + s}{2}}$$

where $s^4 = t^4 + 4\sigma_{xy}^4$ and $t^2 = \sigma_{y^2}^2 - \sigma_{x^2}^2$. $\sigma_{x^2}^2$ and $\sigma_{y^2}^2$ are the variances of the image signal distribution in the camera in the x and y directions, respectively, and σ_{xy}^2 is the covariance. These calculations are of the form

$$\sigma_{ab}^2 = \langle ab \rangle - \langle a \rangle \cdot \langle b \rangle$$

where $\langle a \rangle$ is the mean value of a.

The orientation of the major axis of the ellipse is calculated according to the following:

$$\tan\phi = \frac{(t^2+s^2)\langle y\rangle + 2\sigma_{xy}^2\langle x\rangle}{2\sigma_{xy}^2\langle y\rangle - (t^2-s^2)\langle x\rangle}$$

This can then be used to reconstruct the shower impact location on the ground and the shower direction of origin on the sky. Figures 5.12 and 5.13 illustrate this concept. Since the air shower axis, and therefore the arrival direction of the incoming gamma ray or CR, is colinear with the major axis of the image ellipse, both the impact point of the shower on the ground and the source location on the sky will lie somewhere along the line defined by the major axis of the image ellipse.

To determine the shower's impact point on the ground, the images from each telescope can be projected onto the ground plane. By combining images from multiple telescopes, one can determine the intersection point of the image major axes on the ground (see Figure 5.13). This indicates the shower impact point on the ground. It is important to know the location of the shower's impact on the ground to accurately determine the energy of the initiating gamma ray; a shower closer to the telescopes will appear brighter than an identical shower farther away.

The direction of the shower's origin on the sky (i.e., the source of the shower-originating gamma ray) is determined through a similar process, this time by tracing the origin direction indicated by the major axis in the image (camera) plane. Again, views from multiple telescopes allow for more precise determination of this point; for a single telescope, the origin of an image could lie anywhere along the line defining the major axis.

Once an ellipse has been defined for an image and the impact distance of the shower from the telescope has been reconstructed, one can compare the values of the parameters length and width to lookup tables of these quantities generated from simulations. The cuts on these values are optimized to keep the maximum number of gamma rays while simultaneously cutting the maximum number of CRs (see Figure 5.14).

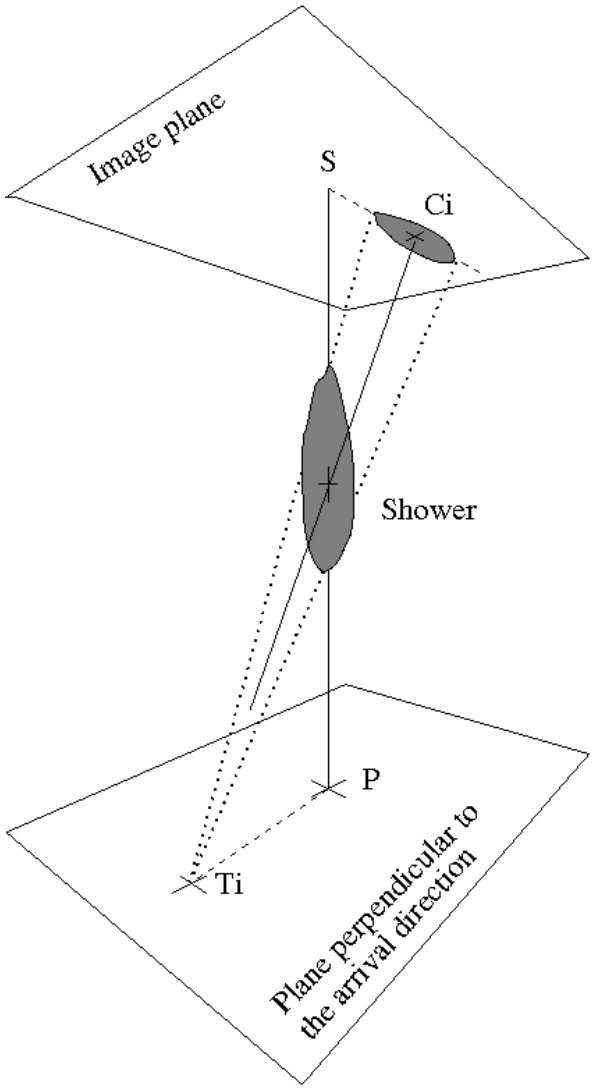

Figure 5.12: Figure 1 from [228]. A diagram showing the projection of an air shower onto the image plane of a telescope. P labels the impact point of the shower on the ground, T_i designates the i^{th} telescope in the array, S labels the source location, and C_i labels the centroid of the image appearing in the camera of T_i.

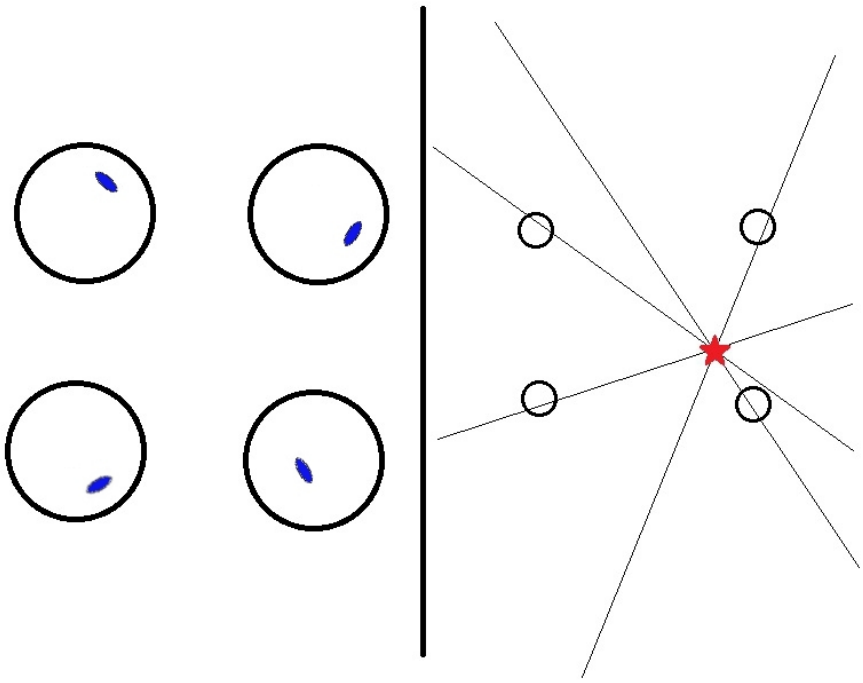

Figure 5.13: A cartoon of an event seen by all four VERITAS telescopes. The left panel shows the cameras of each telescope with the image ellipses. The right panel shows the "top down" view of the four telescopes and the shower location on the ground (red star)(the telescopes and their corresponding cameras are in the same relative arrangement). The orientation of the major axis of each fitted image ellipse indicates the direction to the location on the ground where the shower landed. By using multiple images (i.e., multiple telescopes), this location can be identified more accurately.

These cuts are known as Mean SCaled Width (MSCW) and Mean SCaled Length (MSCL) cuts. These are scaled cuts because the measured length and width of each ellipse is normalized to the mean length and width of simulated gamma rays of the appropriate impact distance and *size*:

$$SCW = \frac{w(S,D)}{w_S(S,D)}$$

$$SCL = \frac{l(S,D)}{l_S(S,D)}$$

where w is the width of an image (a function of *size*, S, and impact distance, D), w_S is the mean width of simulated images, l is the length of an image (also a function of S and D), and l_S is the mean length of simulated images.

Then, the Scaled width and length quantities are averaged over all the telescopes participating in that event, resulting in final values for MSCW and MSCL for each image.

$$MSCW = \frac{1}{n}\sum_{i}^{n}\frac{w_i - w_S(S,D)}{\sigma_w(S,D)}$$

$$MSCL = \frac{1}{n}\sum_{i}^{n}\frac{l_i - l_S(S,D)}{\sigma_l(S,D)}$$

where i is the number of telescopes participating in a given image, w_i (l_i) is the width (length) of the image for each telescope, w_S (l_S) is again the mean width (length) of simulated images, and $\sigma_w(S,D)$ ($\sigma_l(S,D)$) are the spread on the simulated width (length) values.

The energy of the initiating gamma ray is also determined through the use of lookup tables. As was previously described, simulated gamma rays of known energies can be used to generate histograms of length and width based on impact distance. Therefore, observed gamma rays can be compared to these same tables, and their associated energy determined by comparison to simulations, and interpolation from surrounding histogram bins.

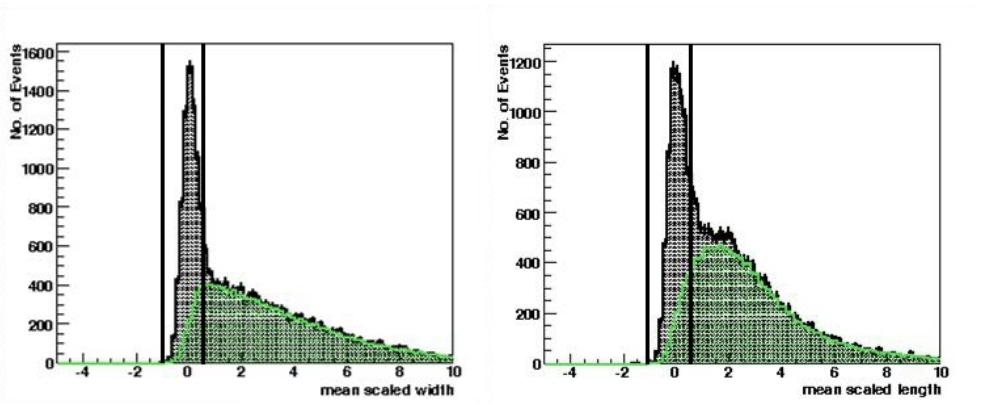

Figure 5.14: An example of distributions of mean scaled width (left) and mean scaled length (right). The black shaded region indicates signal from the region of the sky corresponding to the source position, and the green shaded region indicates signal from a region of the sky containing only background. Events with parameters falling between the two vertical lines in each plot are kept; this keeps most of the signal from the on-source region while cutting most of the background.

At the end of this process, one is left with only cleaned, gamma-ray-like images of known reconstructed energy and origin direction. These presumed gamma-ray images can then be used to construct a skymap and a spectral energy distribution of the source in question. Note that the images are gamma-ray-like, not necessarily gamma rays: CRs producing images that pass the applied cuts will survive to this stage.

5.4 Generating Skymaps

5.4.1 θ^2 Cut

In generating a skymap of a gamma-ray source, one additional cut is applied to the data. This is a cut on the parameter known as θ^2, where θ is the angle on the sky between the reconstructed origin direction of an event and the nominal source location. The reason for this cut is that CRs are isotropic, so any events passing the previous cuts but originating far from the nominal source position are presumed to be gamma-ray-like CRs.

The nominal source location for a previously undetected point source is determined *a priori* from observations in other wavebands. After analysis, the sky map will reveal whether or not the highest statistical significance of gamma rays is positioned at the nominal source location. For a source known to be extended in observations at other wavelengths, a nominal source location is selected based on where in the extended object one might expect gamma rays to be produced. Observations are wobbled around this nominal source location (wobbled observations will be described in Section 5.4.2 of this chapter), and it functions as the nominal source location when generating sky maps. Again, after analysis, a sky map will reveal whether the emission reaches its maximum statistical significance at the selected nominal source location, or elsewhere in the field of view. For follow-up observations of previously detected gamma-ray sources, both point and extended, observations are typically wobbled around the known location of the gamma-ray emission (or other point of interest in the gamma-ray map).

In order to actually generate a sky map, every position in the field of view is tested as a potential source of gamma rays, not just the nominal source position. This will be discussed further in the following section. This approach also makes it possible to detect gamma rays from an entirely unexpected location in the field of view; indeed, many as-yet-unidentified TeV sources are dark in other wavebands (see Chapter 3, Section 3.4.8.1).

At the time the VERITAS Tycho data were analyzed, the standard analysis for point sources cut events with θ^2 larger than $0.015^{\circ 2}$ (see Figure 5.15). After the relocation of telescope T1 (see Chapter 4, Section 4.1.3 for details), the angular resolution of the instrument improved, so this value was able to be reduced to $0.01^{\circ 2}$.

5.4.2 Background Signal Calculation

While the cuts discussed in the previous sections have reduced the amount of CR events in the data drastically, there will still be gamma-ray-like CRs that survive. So, in order to extract a potential gamma-ray signal, one must estimate the remaining CR background at the source location. Once estimated, this background can be subtracted

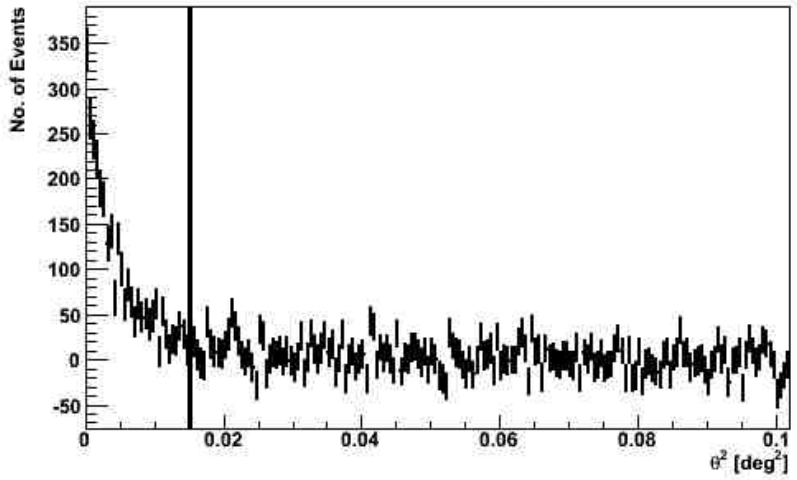

Figure 5.15: A histogram showing the θ^2 value of reconstructed events for a point source (in this case, the Crab Nebula). The x-axis designates the square of angular distance from the source position on the sky, and the y-axis indicates the number of reconstructed events. The vertical line shows the position of the cut value. As one considers positions further from the source, the number of events falls until it reaches a plateau consistent with the isotropic background CR signal. The θ^2 cut is designed to keep as many gamma rays as possible from the on-source region, while simultaneously cutting as much of the isotropic background as possible. An extended source will have a larger on-source region than a point source.

and the statistical significance of any remaining events at the source location can be calculated. It is general practice in the field of gamma-ray astronomy to require at least 5σ significance in order to claim a detection, where σ is one standard deviation above the norm. This is equivalent to a 99.9999% probability that the signal is not a random fluctuation. Note that non-detections can still provide valuable scientific information; upper limits for use in modeling can be derived.

There are three methods which are commonly used by VERITAS to determine the background signal, although others exist (see, e.g., [157]). Two of these methods, the reflected region background method and the ring background method, can be used with the same wobbled observations that contain the source in the field of view, making efficient use of observing time and minimizing systematic effects due to differences in zenith angle, weather, or hardware issues. The third method of background estimation, typically only used for very large extended sources where the source fills most of the field of view, requires separate observations of on-source and off-source regions. With these on/off observations, concerted effort must be made to minimize the systematic effects mentioned above.

The wobble method of observation, first developed by the Whipple collaboration [229], involves taking a series of observations of a source, each pointed at a designated offset distance from the source (typically 0.5° for point sources and 0.7° for extended sources) towards one of the four cardinal directions. The direction of the wobble cycles through the four cardinal directions with each observing run in an attempt to eliminate systematic effects related to background estimation. When the data set is complete, the number of observations with North wobble, South wobble, East wobble, and West wobble should be approximately equal.

In both the reflected region and ring methods of background signal estimation, one must designate a test on-source region potentially containing the source, and (an) off-source region(s) containing no gamma-ray signal. The number of events in the on-source region is N_{ON}, and the number of events in the off-source region(s) is N_{OFF}. A

third parameter, α, is the ratio between the geometrical areas of the on-source and off-source regions. It is necessary to calculate α in order to estimate the background signal in the on-source region. The ring background method, as is implied by its name, uses a ring surrounding the on-source region as the off-source region. The reflected region background method uses a number of circles each equal in area to the on-source region, offset from the camera center by the same distance as the on-source region (see Figure 5.16 for illustrations of each). The number of circles to use for the off-source region can be defined by the analyst, but usually is maximized while still avoiding exclusion regions in the camera for both the on-source region and bright stars (exclusion regions will be discussed in detail in Section 5.4.3). The off-source region is always chosen to be larger than the on-source region to provide values of $\alpha \ll 1$, improving the statistical significance of the signal by reducing the effects of background fluctuations [157]. There are several methods by which the statistical significance (S) of a signal in the on-source region can be calculated, but the one most commonly used in the field of gamma-ray astronomy is Equation 17 from a 1983 paper by Li and Ma [230]:

$$S = \sqrt{2}\left\{ N_{ON} \ln\left[\frac{1+\alpha}{\alpha}\left(\frac{N_{ON}}{N_{ON}+N_{OFF}}\right)\right] + N_{OFF} \ln\left[(1+\alpha)\left(\frac{N_{OFF}}{N_{ON}+N_{OFF}}\right)\right]\right\}^{\frac{1}{2}}$$

Once all cuts have been applied to the data, any surviving events are used to fill sky maps. Two varieties of map are produced: correlated and uncorrelated. In a correlated map, the standard binning is squares of 0.01° per side, and for an uncorrelated map, 0.05°. To produce an uncorrelated map, the reconstructed arrival directions of events are simply binned. A correlated map is created by filling each bin with all reconstructed events passing the θ^2 cut when that bin is the test "on" position. The bins are correlated because, at 0.01° on a side, they are smaller than the value of θ^2 ($0.015^{\circ 2}$) that is being used to fill them. Thus, the placement for each test "on" position also includes events falling into neighboring bins (see Figure 5.17). This allows for higher statistics at each test position, but also means that the morphology of the map is artificially smoothed from the correlation. So, correlated

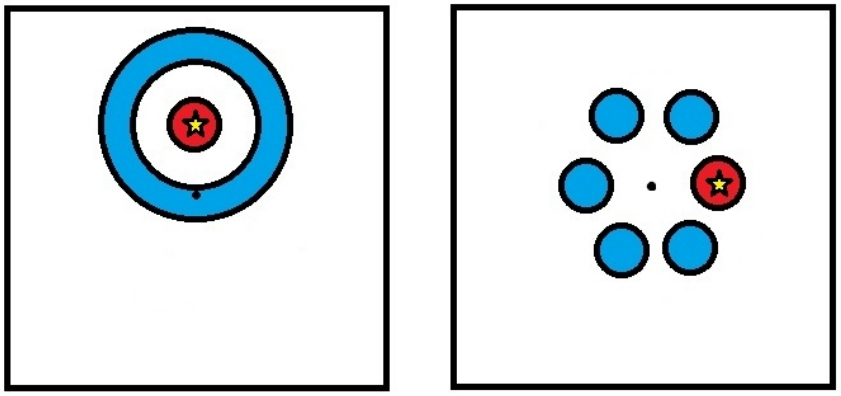

Figure 5.16: A cartoon illustrating the ring background model (left) and the reflected region background model (right). In each case the pointing direction is marked by a black dot (centered), the on-source region is shown in red, the nominal source position is marked by a yellow star, and the off-source region(s) is/are shown in blue. The ring background observation pictured is wobbled to the South, while the reflected region observation pictured is wobbled to the West.

maps are used for measurements of statistical significance, and uncorrelated maps are used for morphological studies.

Several varieties of correlated map, and several varieties of uncorrelated map, are produced. The most critical for producing final sky maps are *on* maps, *off* maps, and *difference* (*diff*) maps. In an *on* map, each bin contains the raw number of events calculated when that bin was the test "on" position, prior to background subtraction. In an *off* map, each bin contains the raw number of events calculated when that bin was part of the test "off" region. In a *diff* map, the contents of each bin are calculated using the formula $diff = on - \alpha \times off$; this removes the estimated background from each test "on" position. The correlated and uncorrelated *diff* maps are then used to conduct statistical significance and morphological studies.

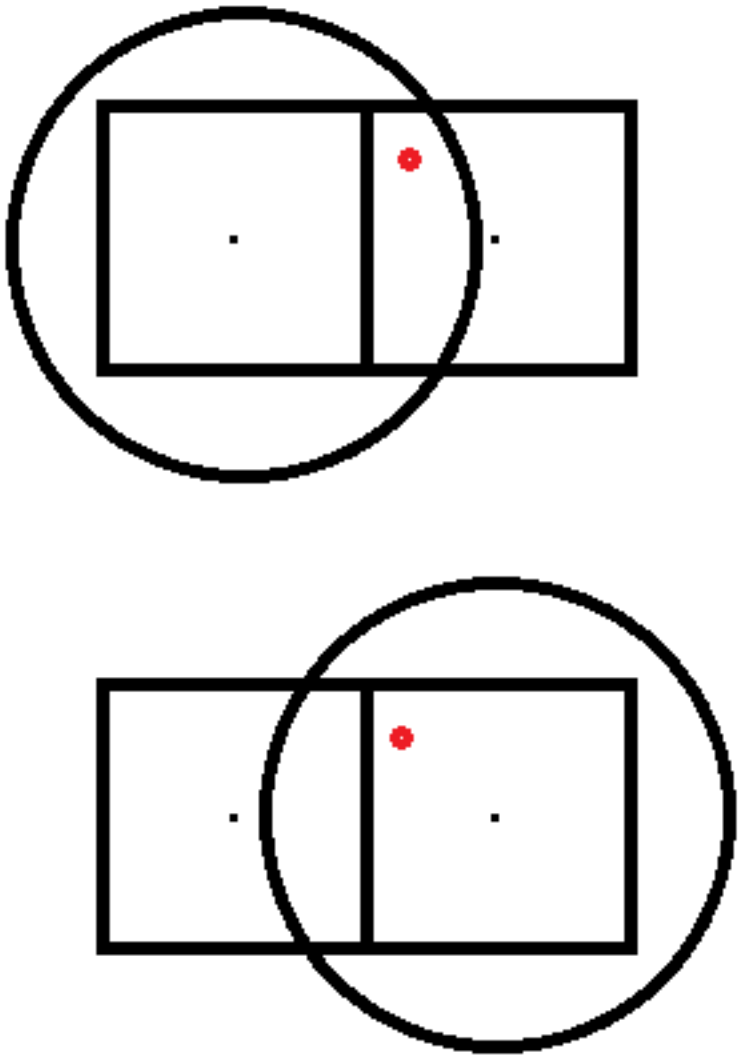

Figure 5.17: A cartoon illustrating how correlated sky maps are produced. When the test "on" position is located in the left-hand bin (top illustration), all events falling within the value of the θ^2 cut (black circle) from the position of the bin center (black dot) will be included in the bin, even if their reconstructed arrival direction places them outside the bin. The neighboring bin will be filled the same way (bottom illustration), and will therefore include some of the same events. One such "shared" event is illustrated by the red dot.

5.4.3 Camera Acceptance and Exclusion Regions

A topic closely related to background calculation is camera acceptance. Events falling near the edge of the camera have a higher likelihood of being only partial, truncated images. The cuts then applied to the data have the effect that the closer to the edge of the camera an event is, the less likely it is to pass the cuts. In order to determine how likely an image is to pass the cuts (with the exception of the θ^2 cut) based on its position in the camera, one can generate an *acceptance curve*, normalized to the acceptance at the camera center. An example is shown in Figure 5.18. The ring background model must take into account the acceptance curve. This is because the ring covers a range of distances from the camera center. The reflected region background model does not suffer this disadvantage, because each of the off-source regions is the same distance from the camera center and covers the same area as the on-source region. This makes the reflected region background model preferable when reconstructing energy spectra, although certainly the ring background model can be used.

Another factor which must be considered when generating skymaps are the effects of bright stars in the field of view. A bright star will produce photoelectrons, and therefore current, in the PMT aligned with it. If the current is high enough, the high voltage to that PMT will automatically shut off to avoid damage to the PMT. Even if the current does not exceed this threshold, the *pedvars*, or fluctuations in the average charge, will be very large in that PMT when compared to an average PMT. Both of these scenarios will distort any Cherenkov images that PMT participates in. To prevent these spurious pixels from influencing the final result, exclusion regions are defined around the positions of any stars brighter than a pre-defined magnitude. The standard analysis excludes stars brighter than 6^{th} magnitude with an exclusion radius of $0.15°$, although different exclusion radii can be defined by the analyst for especially bright stars (see Figure 5.19 for an example). Exclusion regions are excluded from being part of the off-source regions in background estimations; an artificially dim background due to the removal of events falling within the exclusion region will falsely increase the

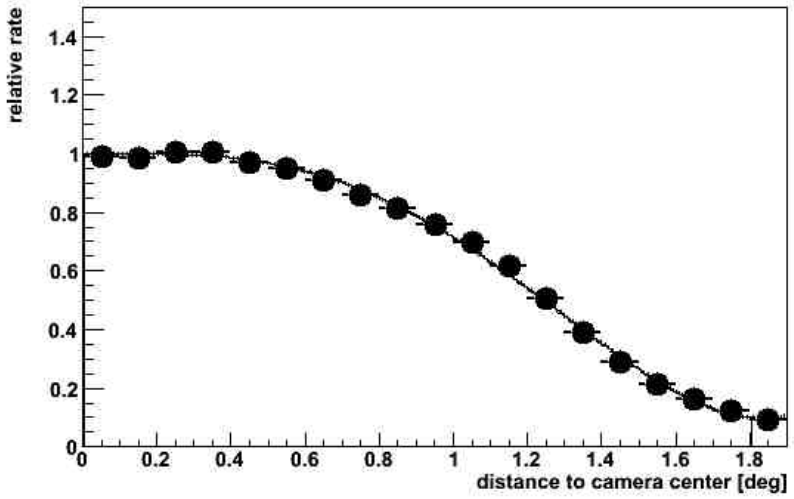

Figure 5.18: An example of an acceptance curve. The horizontal axis is measured in degrees from the camera center, while the vertical axis is the likelihood of an event passing the specified cuts (except for the θ^2 cut), normalized to the likelihood at the camera center. The solid line represents the best fit to the data.

statistical significance of any signal in the field of view. Also excluded are regions of strong gamma-ray excess, for similar reasons: were the gamma-ray signal to be included in the estimation of background, it would artificially brighten the background, falsely decreasing the statistical significance of a signal.

5.5 Generating Spectral Energy Distributions

If a gamma-ray source has been detected, a spectral energy distribution (SED) can be calculated for that source. The SED is a plot of energy vs. number of events per unit area per unit time per unit energy: $\frac{dN}{dAdtdE}$. The shape of the energy distribution of the source provides information about the physical processes producing the observed photons. With sufficiently small error bars on the data and detailed, well-informed models, identification of the parent particle population as hadronic or leptonic is possible.

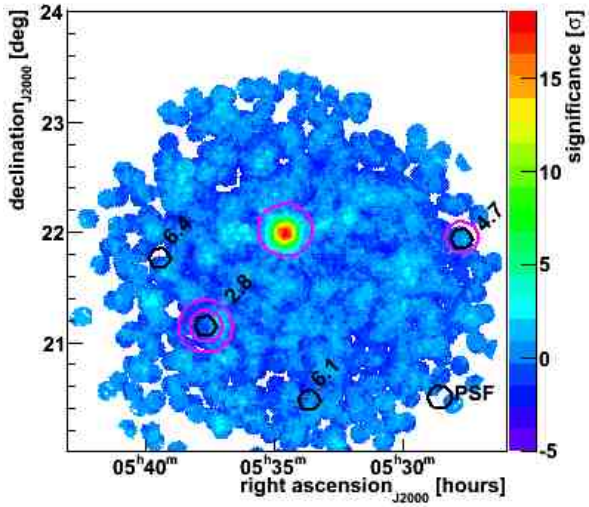

Figure 5.19: An example of a gamma-ray significance map (the Crab Nebula) showing bright stars in the field of view (black circles) and exclusion regions (magenta circles) around those brighter than 6^{th} magnitude. The magnitudes of the stars are labeled. The standard exclusion radius of 0.15° is shown for the star located at RA: 05h 27' 38.1", Dec: +21° 56' 13". Zeta Tau, located at RA: 05h 37' 38.7", Dec: +21° 08' 33", has an exclusion region of 0.25° defined, as does the Crab Nebula itself.

Determining the energy of a reconstructed photon was discussed previously in Section 5.3.2. However, in order to correctly graph a SED, the live-time and effective area of the observations must be accounted for. During observations, as events are read out from the FADC buffers, new events cannot simultaneously be read in. This readout time is known as dead-time, and constitutes $\sim 10\%$ of observing time in total. Live-time is simply the total observing time minus this dead-time.

The effective detection area of the array is not constant; it is actually a function of photon energy, zenith angle of observations, azimuth of the observations, angular distance between the incoming photon and the pointing position of the telescope, brightness of the night sky background light, number of telescopes in use for the data run, and cuts applied to the data. To calculate the effective area of a Cherenkov telescope array, Monte Carlo simulations are used. Simulated gamma rays covering a range of the listed parameters are thrown over a large area surrounding the simulated array, and the fraction of events of a given energy detected by this simulated array determines the effective area at that energy. The formula used to calculate this in a given energy bin is:

$$A(E) = A_0 \frac{n}{N}$$

where A_0 is the area the simulated gamma rays are thrown over, n is the number of gamma rays detected, and N is the number of gamma rays simulated. Figure 5.20 shows an example of an effective area curve. Figure 5.21 shows the spectrum of the Crab Nebula before and after the inclusion of the effective area curve. At low energies, the division of the spectral points by the effective area curve increases their value. At higher energies, where the effective area curve is nearly constant, it has little effect on the spectral points. The power-law demonstrated in the spectrum is only clearly visible after the inclusion of the effective area.

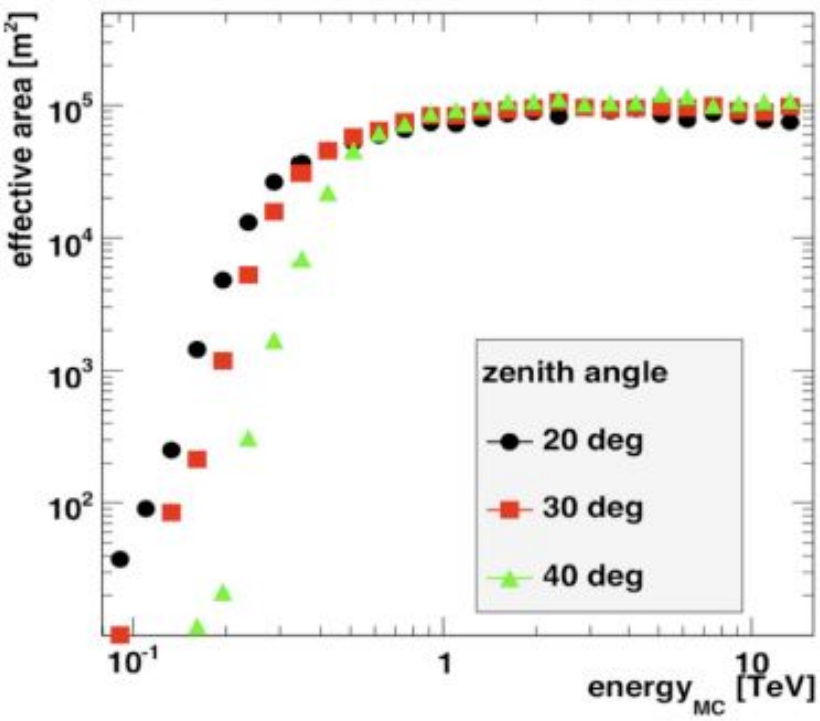

Figure 5.20: An example of an effective area curve at various zenith angles.

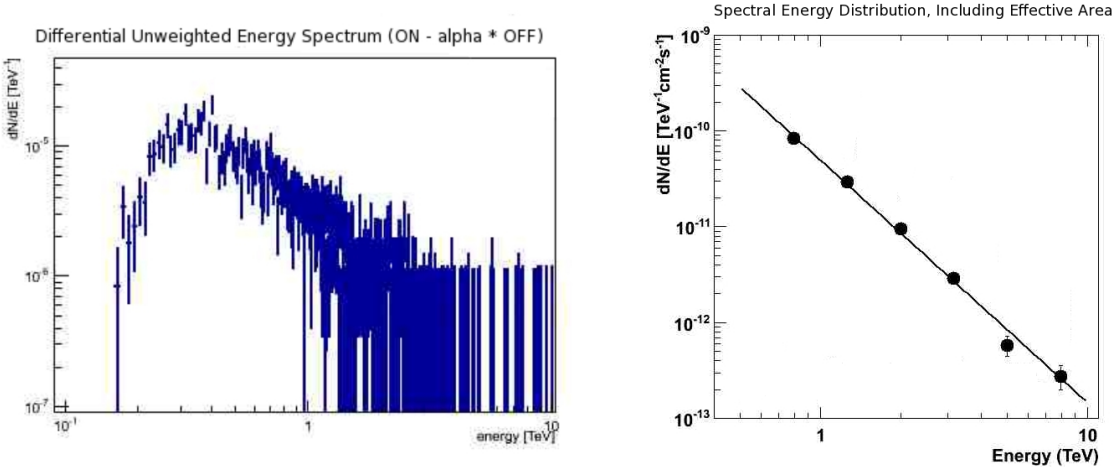

Figure 5.21: The spectrum of the Crab Nebula before (left) and after (right) the inclusion of the effective area curve.

Chapter 6

DETECTING GAMMA RAYS FROM TYCHO'S SUPERNOVA REMNANT

6.1 VERITAS Data on Tycho

6.1.1 Dataset

In April 2011, VERITAS published the first detection of gamma-ray photons from Tycho's SNR [29]. The detection was the result of 66.7 hours of observations spanning two years and two array arrangements.

The published data were taken during two observing seasons, between which telescope T1 was relocated to provide a more symmetric array layout, increasing the sensitivity of the array (see Chapter 4, Section 4.1.3 for details). During the first season, 21.9 hours of data were taken between October 2008 and January 2009, with a mean zenith angle of 35°. In the second season, 44.7 hours of data were taken between September 2009 and January 2010, with a mean zenith angle of 39°. At the location of the VERITAS telescopes, Tycho's SNR (RA: 00h 25' 15", Dec: +64° 8' 00" (J2000)) is only visible during the Fall and early Winter months, and culminates at an elevation of 58° (zenith angle of 32°); hence, all the observations are at relatively low elevation (large zenith angle). All data included in the analysis were taken under "A" weather conditions (see Chapter 5, Section 5.1 for a discussion of weather evaluation). The observations were all taken in "wobble mode" with an offset of 0.5° (see Chapter 5, Section 5.4.2 for an explanation of "wobble mode"). All of the 2008-2009 data were taken with 4 telescopes, as were all of the 2009-2010 data except for 80 minutes of 3-telescope data.

Between September 2010 and January 2011 an additional 22.4 hours of data were taken on Tycho's SNR. The mean zenith angle of these new, as-yet-unpublished

data is 38°. Again, the data are all taken under "A" weather conditions and with 0.5° wobble observations. The dataset includes 90 minutes of 3-telescope data, and the remainder is 4-telescope data. A summary of the dataset is provided in Table 6.1.

6.1.2 Analysis

In Spring 2009, the first analysis of the 2008-2009 VERITAS data on Tycho's SNR was completed. This was a relatively small data set, and at the time this source was undetected in TeV gamma rays, so all cuts had to be defined *a priori* to avoid unnecessary statistical trials (discussed below in Section 6.1.3.1 of this chapter). Given that this source is a SNR, the physics at work in this environment (i.e., acceleration of particles by the shock front) dictate that any emission will likely have a Crab-like or harder (more high energy photons) spectrum. Additionally, previous upper limits on Tycho dictated that any detected emission would be weak. Therefore, it was decided initially that the data should be analyzed with both "standard" cuts and "hard" cuts[1]. It was known from previous observations at radio and X-ray wavelengths that the diameter of the remnant is ∼8'=0.13°, which is approximately the same as the VERITAS point spread function (68% containment) of 0.11°, so the point source (rather than extended source) version of each set of cuts were applied. Additionally, analyses were run for both the ring background model and the reflected region background model (see Chapter 5, Section 5.4.2 for a discussion of background calculation); because the source was previously undetected, using two methods of calculating the background would reveal if any signal was an artifact of one of the methods.

The analyses using standard cuts showed no signal, but the analyses using hard cuts showed a signal $> 2\sigma$ at the nominal source position, and contained a bin slightly offset from the nominal source position with a signal $> 4\sigma$. Motivated by this intriguing result, at least 25 hours of observations of Tycho were awarded for the 2009-2010 VERITAS observing season, with possible additional data to be taken based on the

[1] In addition to being suited to hard-spectrum sources, hard cuts also remove more background than standard cuts, making them a suitable choice for weak sources.

Observing Season	Array Configuration	Total Amount of Data (hrs.)	3-telescope Data (hrs.)	4-telescope Data (hrs.)	Mean Zenith Angle (°)	Previously Published?
2008-2009	Original	21.9	0	21.9	35	Yes
2009-2010	T1 relocated	44.7	1.3	43.4	39	Yes
2010-2011	T1 relocated	22.4	1.5	20.9	38	No

Table 6.1: A summary of VERITAS observations of Tycho's SNR discussed in this work.

results from the initial time allotment. The analysis and results of the 2008-2010 data will be discussed in detail below.

While the published results from the 2008-2010 data are extremely interesting, questions remain about the source of the observed emission. The signal is relatively weak, so the error bars on spectral energy distribution (SED) data points are relatively large. Furthermore, the position of the signal made it ambiguous whether or not the emission was related to the nearby molecular cloud. Because of this, further observation time was awarded in 2010-2011. The analysis and results of those data will also be discussed below.

In 2011-2012, VERITAS did not collect any data on Tycho. Observing time was approved by the time allocation committee, but only after datasets on some other interesting targets near the same RA were completed. Exceptionally poor weather that Fall meant that those sources did not complete their allotted time, so Tycho did not receive any time. However, in 2012-2013 and 2013-2014, additional data on Tycho has been collected, and analysis of the complete data set to date is ongoing.

6.1.2.1 Cuts

Data from all three observing seasons were analyzed with the following (hard) cuts (see Chapter 5, Section 5.3.1 for descriptions of cut parameters):

- *Size* per image $>$ 1200 d.c. ($\simeq$ 226 photoelectrons, or p.e.)
- Minimum number of adjacent PMTs containing a signal at least 5 times the *pedvar* to be considered an image: 4
- Maximum value of *loss* for a given image: 20%
- -1.2 $<$ MSCW $<$ 0.5
- -1.2 $<$ MSCL $<$ 0.5

The standard cuts also used on the 2008-2009 data were identical, except for the *size* cut. Standard (as opposed to hard) cuts require a *size* per image $>$ 500 d.c..

Recall from Chapter 5 that MSCW and MSCL are calculated in the following way:

$$MSCW = \frac{1}{n}\sum_{i}^{n}\frac{w_i - w_S(S,D)}{\sigma_w(S,D)}$$

$$MSCL = \frac{1}{n}\sum_{i}^{n}\frac{l_i - l_S(S,D)}{\sigma_l(S,D)}$$

Thus, negative values for these quantities can occur if the width (length) of the image in question is smaller than the average value of width (length) from simulated gamma rays.

In the 2008-2009 data on Tycho, the value of θ^2 used was $0.015^{\circ 2}$. In the 2009-2010 and 2010-2011 data, the value of θ^2 used was $0.01^{\circ 2}$. This reduction in the value of the standard θ^2 cut reflects the improved angular resolution of the array due to the relocation of T1.

6.1.3 Skymaps and Morphological Studies

6.1.3.1 Statistical Trials

In any statistical analysis, there is a small chance that a high significance (several standard deviations above or below the norm) signal will appear due to random fluctuations. The more times the analysis is performed (e.g., the more sets of cuts applied to the data, or the larger the search area for a potential signal), the more likely it is that a high significance signal will be found purely randomly. As an analogy, if a die is rolled, the chance that a six will come up on one roll is 1:6. But, if the die is rolled a hundred times, the chance of getting a six on at least one of those rolls is much higher.

In order to account for this, one must include a statistical trials factor in the final result. In mapping gamma-ray data, this is calculated by tiling the search area for a potential signal with squares of appropriate size, and multiplying by the number of sets of cuts being applied. For Tycho, the extent of the radio remnant is 8'. In order to include any gamma rays resulting from possible interaction with the molecular cloud

in the field of view, a square was considered with sides twice this size, 16' = 0.267°. Then, the square was tiled with 0.04° square bins (see, e.g., [231]). This size bin ($\sim \frac{1}{3}$ the instrument point spread function) was selected in order to slightly oversample the signal, guaranteeing that the peak significance would not fall between bins. This procedure resulted in a trials factor of $(0.267°/0.04°)^2 = 44.5$. This was rounded to 50, to be conservative. Then, the factor of 50 was multiplied by 2 because two sets of cuts (standard and hard) were used with the initial 2008-2009 dataset. Thus, the total trials factor for the 2008-2010 data was 100. Note that statistical trials are only an issue for observations where it is unknown if a signal is present. Thus, for datasets including only data taken after 2010 (the 2008-2010 dataset comprising the initial detection), one need not consider trials when completing an analysis.

The trials factor is then used to adjust the statistical significance of the signal. The pre-trials statistical significance can be converted to a probability (p):

$$p = 1 - erf(\frac{\sigma_{pre}}{\sqrt{2}})$$

This probability can then be converted to a post-trials probability (P), using the trials factor (N) [232]:

$$P = 1 - (1 - p)^N$$

This overall probability can then be converted back to a post-trials significance:

$$\sigma_{post} = \sqrt{2} \times erf^{-1}(1 - P)$$

For the 2008-2010 Tycho data, the skymap bin containing the highest significance (note that this is not the nominal source position nor the best-fit position of the excess; more on this below) contained 5.84σ pre-trials. With a trials factor of 100, this becomes 5.02σ post-trials. In the 2008-2011 dataset, the skymap bin with the highest significance contained 5.94σ pre-trials. Because this dataset contains the original dataset (i.e., it is not an entirely new, independent analysis), the same trials factor is

applied, resulting in a post-trials significance of 5.13σ.

6.1.3.2 Exclusion Region

The 2° field of view in which Tycho's SNR sits contains one star brighter than 6th magnitude, the location of which was excluded from the analysis. It is a magnitude 4.3 star, located at RA: 00h 33' 00.0", Dec: 62° 55' 54.1". The exclusion radius around the star was 0.15°, which is the standard exclusion radius (see Chapter 5, Section 5.4.3 for a more general discussion of exclusion radii). This star was excluded from the analysis in this way for all three years of data. The distance from the position of Tycho's SNR to this star is 1.385°, and so the exclusion region affected neither the on-source nor off-source regions in the pre-defined search area.

6.1.3.3 Morphological Studies

When skymaps are generated, events are sorted by their reconstructed arrival direction into square bins on the map. Two kinds of skymap are generated: correlated and uncorrelated (see Chapter 5, Section 5.4.2 for a general discussion of correlated and uncorrelated maps). When performing morphological studies, the uncorrelated map should be used. Specifically, one should use the uncorrelated *difference* map (see Figure 6.1), where for each bin in the map, $diff = N_{ON}$ - $\alpha \times N_{OFF}$ (recall from Chapter 5, Section 5.4.2 that α is the weighting factor that accounts for the difference in area between the on-source region and the off-source region(s)).

Depending on the particular gamma-ray source under study and its surrounding environment, a gamma-ray signal may or may not appear at the nominal source position. If the emission region of maximum significance is offset from the nominal source position, one wants to know a) the best-fit centroid position for the emission, and b) the distance and direction of the offset from the nominal source position. In the case of extended emission, one also wants to know the quantitative extent of the extension.

The correlated skymap from 2008-2010 data on Tycho is shown below in Figure 6.2. Note that the area of maximum statistical significance (indicated by the black

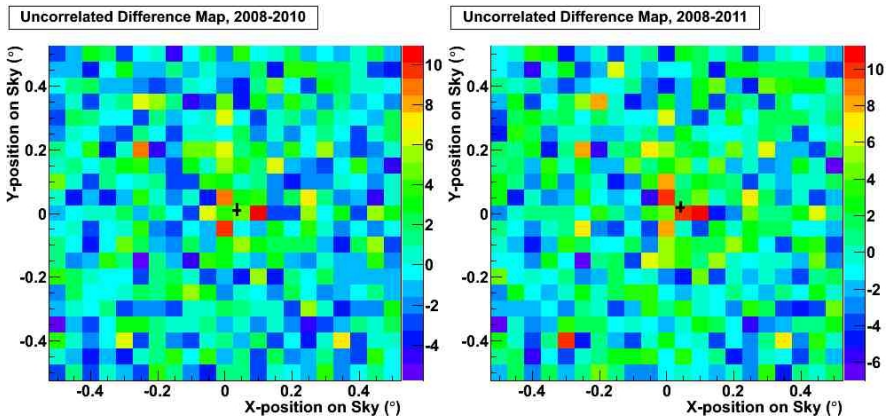

Figure 6.1: Left panel: uncorrelated *difference* map of VERITAS data on Tycho's SNR from 2008-2010. Right panel: uncorrelated *difference* map of VERITAS data on Tycho's SNR from 2008-2011. In each map, the color scale indicates the number of excess events after background subtraction, and the black cross indicates the best-fit position; the lengths of the arms indicate 1σ statistical errors. The maps are displayed in camera coordinates; here, North is up and East is to the left.

cross) is offset from the nominal source position (indicated by the black diamond). Qualitatively, this is an interesting result because the offset is towards the molecular cloud, implying that the gamma rays seen may have originated from SNR-accelerated CRs interacting with the molecular cloud. However, one must quantify the offset in order to determine whether or not it is significant, and one must consider the SED to determine the parent particles for the gamma rays. To quantify the offset, we fit a function to the emission and determine the errors on the fit.

6.1.3.4 Fitting a 2-D Gaussian Function to the Skymap

The simplest function that can be fit to the emission map is a symmetric 2-D Gaussian. However, gamma-ray emission from a point source is actually better fit by a combination of two Gaussians, one broad and one narrow. This is related to telescope multiplicity, or the number of telescopes detecting a particular event. Events triggering only two telescopes tend to have shower impact points on the ground outside of the

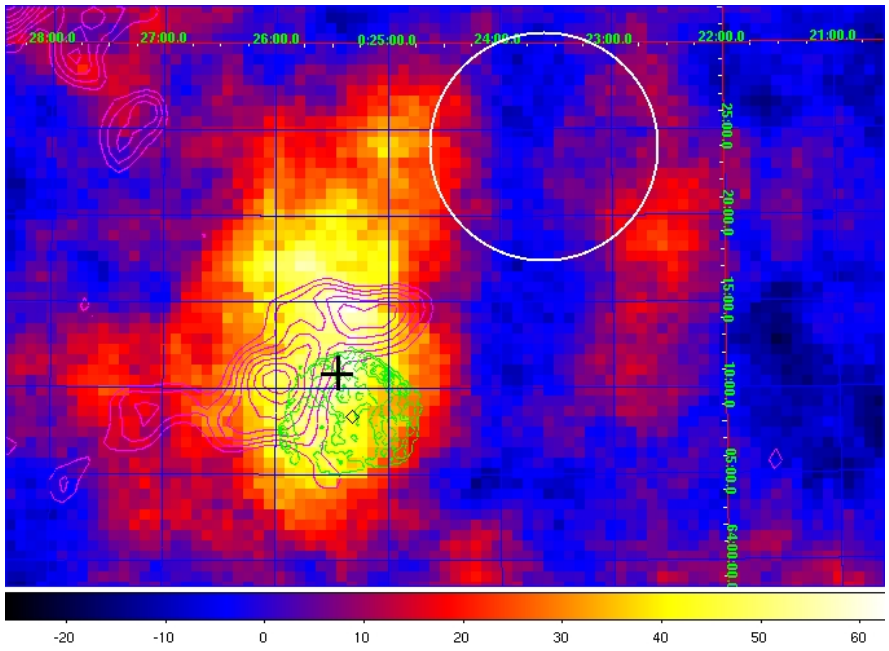

Figure 6.2: Color scale: map of excess events from VERITAS observations of Tycho's SNR from 2008-2010 after background subtraction. Green contours: extent of Tycho's SNR from *Chandra ACIS* observations [64]. Magenta contours: ^{12}CO ($J = 1 - 0$) emission from the *FCRAO* survey [233]. Black diamond: center-of-remnant position. Black cross: best-fit position of gamma-ray emission maximum; the lengths of the bars represent 1σ statistical errors on the position. White circle: VERITAS PSF (68% containment). The horizontal direction maps right ascension (J2000 coordinates), and the vertical direction maps declination.

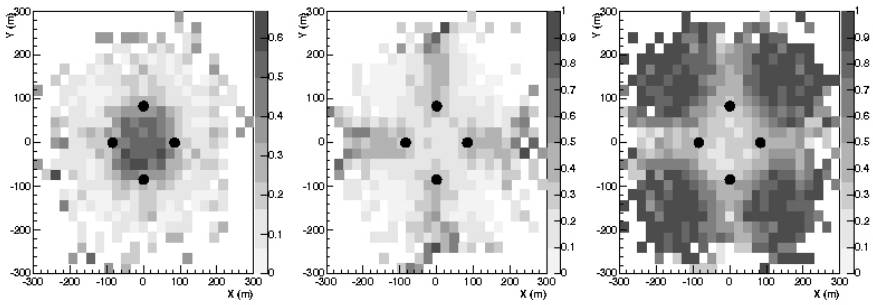

Figure 6.3: Figure 15 from [234]. "Fraction of vertical γ-ray showers triggering n_T telescopes as a function of the impact position (X and Y coordinates) on the ground. From left to right: $n_T = 4$, $n_T = 3$, $n_T = 2$. The γ-ray spectrum is a power law with a spectral index of 2.4. The black dots indicate the position of the H.E.S.S. telescopes." Although this figure specifically uses simulations designed for the H.E.S.S. array, the VERITAS array is similarly arranged and the same concept applies.

array, while events triggering four telescopes tend to impact nearer to the center of the array. This effect is illustrated in Figure 6.3. Since the higher multiplicity events (i.e., events impacting nearer to the array core) provide more views of the same event, they are reconstructed more accurately. This results in higher multiplicity events creating a "central spot" in the angular distribution of reconstructed gamma rays, while lower multiplicity events produce a "broad halo" around the central spot [234]. The θ^2 distribution of simulated gamma rays from zenith, shown in Figure 6.4, demonstrates the broadening of the reconstructed shower with decreasing telescope multiplicity.

In fitting the results from Tycho, we considered that a Gaussian with a width smaller than the PSF of the instrument is a non-physical result (the shape of the emission is inherently smeared out by the instrument PSF), so the instrument PSF was convolved with the combined 2-D Gaussian function to ensure a minimum width matching the PSF. The numerical value for the instrument PSF was determined by fitting an unrestricted combined (broad and narrow component) 2-D Gaussian to a skymap from observations on the Crab Nebula (a known point source) analyzed with the same cuts as the Tycho data.

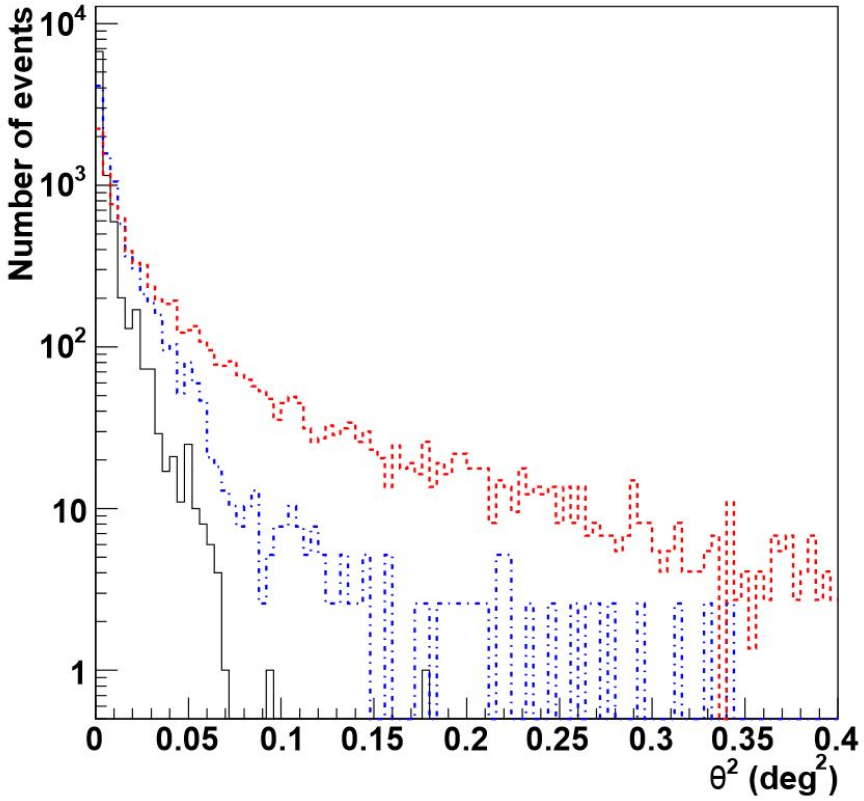

Figure 6.4: Figure 21 from [234]. "θ^2 distribution from 1 TeV γ-ray showers simulated at zenith. (a) Dashed [red] line: events triggering two telescopes. (b) Dashed-dotted [blue] line: events triggering three telescopes. (c) Solid [black] line: events triggering four telescopes."

The symmetric 2-D Gaussian function used to fit to the Tycho map was:

$$A \times \left\{ (r \times e^{-\frac{1}{2}\left(\frac{(x-x_0)^2}{\sigma_o^2+\sigma_n^2}+\frac{(y-y_0)^2}{\sigma_o^2+\sigma_n^2}\right)}) + ((1-r) \times e^{-\frac{1}{2}\left(\frac{(x-x_0)^2}{\sigma_o^2+\sigma_b^2}+\frac{(y-y_0)^2}{\sigma_o^2+\sigma_b^2}\right)}) \right\}$$

where A is the overall normalization (related to the amplitude of the excess emission), r is the ratio of the broad component of the Gaussian defining the PSF to the narrow component of the Gaussian defining the PSF, x_0 is the x-position of the center, y_0 is the y-position of the center, σ_o is the width of the Gaussian function, σ_n is the width of the narrow component of the Gaussian used to define the PSF, and σ_b is the width

of the broad component of the Gaussian used to define the PSF. In the end, the best fit was achieved when σ_o was fixed to be zero, indicating that the source is consistent with a point source convolved with the instrument PSF.

The morphology code I wrote made use of the fitting capabilities in ROOT, a software package published by CERN and used within VERITAS to perform fits and display results, to fit the Gaussian to the uncorrelated *difference* map. In order for the fit to converge, it was necessary to first set the error for bins containing zero events to ± 1 event. The fit was limited to be within a square 0.5° on a side, centered on the nominal source position. This limited the fitting algorithm to finding a fit within the emission area, as opposed to some smaller local maximum elsewhere on the map, while encompassing the entirety of the possible SNR/MC interaction.

6.1.3.5 Testing the Code on Tycho Background

To ensure that the morphological fitting software was providing a good fit to the data, several tests were performed with the code. First, a fixed width, fixed amplitude, symmetric 2-D test Gaussian was superimposed onto the uncorrelated Tycho *difference* map. The test Gaussian had an amplitude $\sim$10 times greater than the amplitude of the Tycho excess. This was to simulate a strong signal on real background data, including fluctuations. The fitting function was then run over the entirety of the map, removing the restriction to fit within a 0.5° square centered on the nominal source position. Then the centroid position of the test Gaussian was shifted by 0.1° and the process was repeated. For each iteration, the χ^2 value of the fit, the probability of being a good fit, and number of degrees of freedom (DOF) available to the fit were recorded.

After tiling the entire map in 0.1° steps, the distribution of χ^2 values of all the fits was examined, excluding those positions within the 0.3° square centered on the nominal source position (i.e., excluding the area containing the real Tycho signal, since one would not necessarily expect a Gaussian to be a good fit to a test Gaussian + real background + real signal). Thus, this distribution of χ^2 values represents only the results of the fitting function on the fixed test Gaussian superimposed on

actual background data. The distribution is shown in Figure 6.5. Mathematically, as the number of DOF increases, any χ^2 distribution quickly approaches a Gaussian distribution with a mean equal to the number of DOF and a width equal to the square root of the number of DOF. The solid line shown in Figure 6.5 is a Gaussian function fit to the distribution of χ^2 from fits to the test Gaussian superimposed on the real Tycho background. The χ^2 of the fit of the Gaussian to this distribution is 61.87, with a probability of goodness of fit of 0.00635, corresponding to a poor fit at the 2.7σ level. The mean of the distribution of data points (455.3) and the mean of the fitted Gaussian function (455.4) agree within 0.02% (3.7σ good agreement), and the RMS width of the data (44.3) and the width of the fitted Gaussian function (25.3) agree within 57% (0.56σ good agreement). This fit was acceptable, given the fluctuations inherent in the real background data on which the test Gaussian was superimposed.

6.1.3.6 Testing the Code on Other Source Backgrounds

As an additional check that the morphological fitting code was robust under varying conditions, the code was tested on two other sets of gamma-ray data. The first dataset contained observations of M82, a starburst galaxy and a comparably weak, but detected, TeV gamma-ray source. The second dataset was comprised of observations of Segue 1, a dark matter candidate with no detected TeV emission. The same process used for the Tycho data was repeated on these sources: superimpose a symmetric 2-D test Gaussian on the uncorrelated *difference* map; use the fitting code to fit a symmetric 2-D Gaussian convolved with the 2-component VERITAS PSF to the map; record the χ^2, probability of goodness of fit, and number of DOF of the resultant fit; shift the position of the superimposed test Gaussian by 0.1° and repeat until the entire map has been covered. For the M82 data, as with Tycho, the results from iterations within a 0.5° square of the nominal source position were excluded from the χ^2 distribution. This was not necessary for the Segue 1 data since there was no statistically significant signal within the field of view.

The distribution of χ^2 values of fits to the test Gaussian atop background data

from M82 was well fit to a Gaussian approximation of a χ^2 distribution with the appropriate number of degrees of freedom. The probability of the fit being good was 35.8% (poor at the 0.92σ level). The distribution of χ^2 values of fits to the test Gaussian atop Segue 1 background data was also a good fit to a χ^2 distribution with the appropriate number of degrees of freedom. The probability of the fit being good ws 40.2% (poor at the 0.84σ level). The success of these fits shows that the morphological fitting code was providing reliable results.

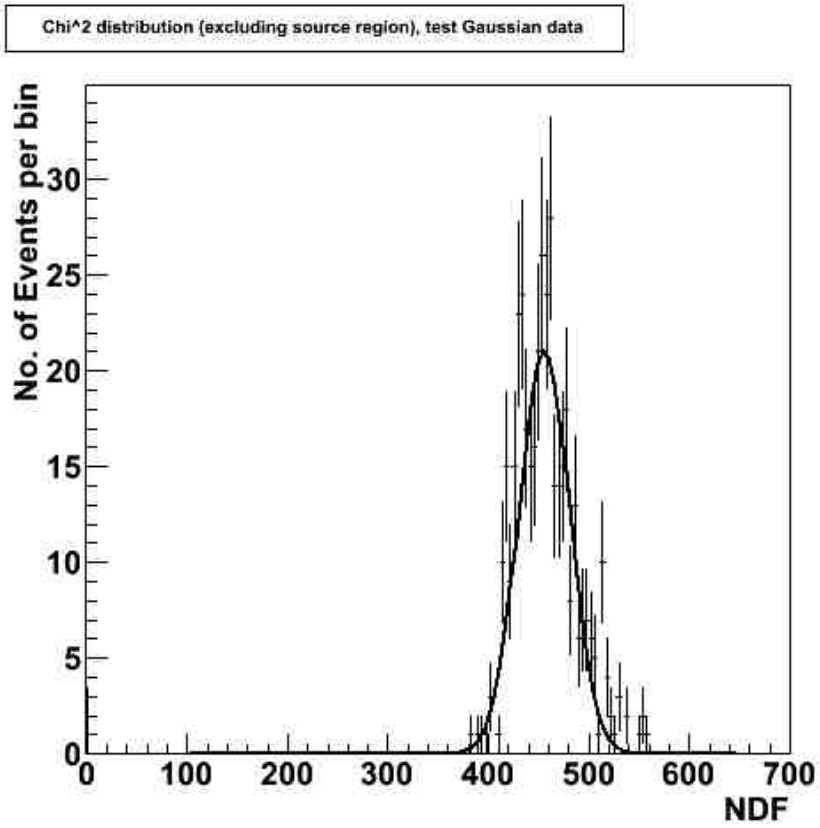

Figure 6.5: χ^2 distribution of results of fit to symmetric test Gaussian superimposed on Tycho background data from 2008-2010. The solid black line is a Gaussian function that has been fit to the data. Here, the events shown on the y-axis are the χ^2 values of fits to the superimposed test Gaussian.

6.1.3.7 Results of Morphological Studies on Tycho

The best-fit position to the 2008-2010 data with a symmetric 2-D Gaussian convolved with the instrument PSF was at RA: 00h 25' 27.0", Dec: 64° 10' 50", offset by 0.04° from the nominal source position towards the MC located to the northeast of the SNR (see Figures 6.1 and 6.2). The statistical uncertainty in the location is 0.023°, and the uncertainty in the position due to telescope pointing accuracy is 0.014°. The systematic uncertainty is determined through the use of the VERITAS Pointing Monitor (VPM) system, discussed in Chapter 4, Section 4.1.3.4.

The statistical significance of the offset from the X-ray and radio remnant center (nominal source position) is 1.6σ; this offset is statistically insignifcant, and thus the emission is consistent with originating from the nominal source position. The Gaussian provided the best fit when the width was fixed to be only that of the PSF; that is, the emission was best fit as a point source.

For the 2008-2011 data, the best-fit position with a symmetric 2-D Gaussian convolved with the instrument PSF was still within errors of the fit to the 2008-2010 data. A map of the 2008-2011 data, along with the best-fit positions from the 2008-2010 and 2008-2011 data sets, is shown in Figure 6.6.

6.1.3.8 Other Attempted Fitting Functions

One can see in Figures 6.2 and 6.6 that by eye, the VERITAS excess emission appears not circular, as would be well-described by a 2-D symmetric Gaussian function, but rather somewhat elongated in the north/south direction. Thus, it was also attempted to fit a 2-D asymmetric Gaussian to the data, convolved with a 2-component symmetric 2-D Gaussian representing the instrument PSF. The 2-D asymmetric Gaussian convolved with the PSF was defined by the following function:

$$A \times \left\{ (r \times e^{-T_1}) + ((1-r) \times e^{-T_2}) \right\}$$

where A is the overall normalization, and r is the ratio of the broad component of the

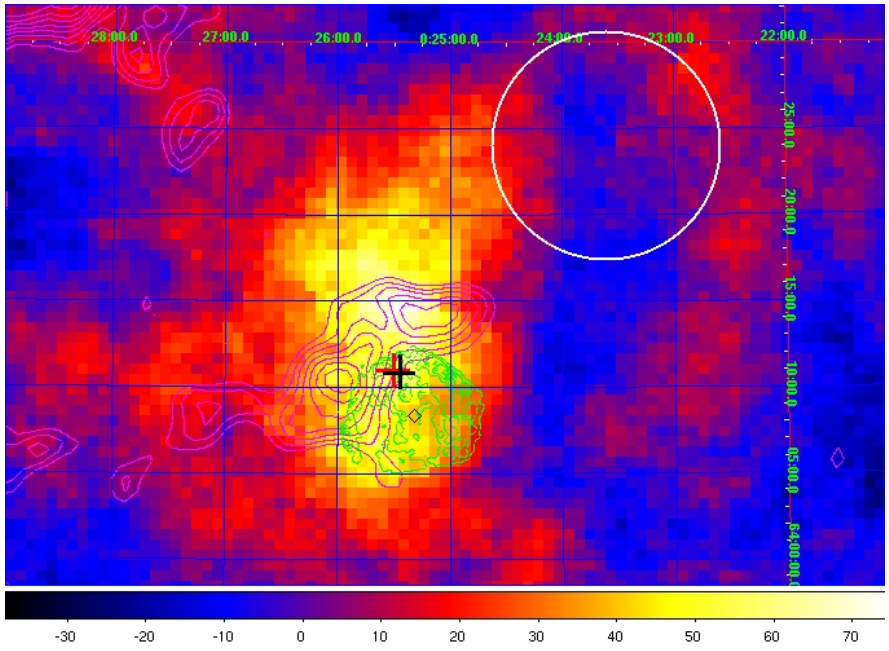

Figure 6.6: Color scale: map of excess events from VERITAS observations of Tycho's SNR from 2008-2011 after background subtraction. Green contours: extent of Tycho's SNR from *Chandra ACIS* observations [64]. Magenta contours: ^{12}CO ($J = 1 - 0$) emission from the *FCRAO* survey [233]. Black diamond: center-of-remnant position. Black cross: best-fit position of gamma-ray emission with a 2-D symmetric Gaussian convolved with the instrument PSF from 2008-2010 data; the lengths of the bars represent 1σ statistical errors on the position . Red cross: best-fit position of gamma-ray emission with a 2-D symmetric Gaussian convolved with the instrument PSF from 2008-2011 data; the lengths of the bars represent 1σ statistical errors on the position. White circle: VERITAS PSF (68% containment). The horizontal direction maps right ascension (J2000 coordinates), and the vertical direction maps declination.

Gaussian forming the PSF to the narrow component of the Gaussian forming the PSF. The functions T_1 and T_2 are defined as follows:

$$T_1 = a_1(dx)^2 + 2b_1(dx)(dy) + c_1(dy)^2$$

$$T_2 = a_2(dx)^2 + 2b_2(dx)(dy) + c_2(dy)^2$$

where

$$dx = (x - x_0) \times \cos dec$$

$$dy = (y - y_0)$$

$$a_1 = \frac{1}{2}\left\{\frac{\cos^2 r_0}{(\sigma_x)^2 + (\sigma_n)^2} + \frac{\sin^2 r_0}{(\sigma_y)^2 + (\sigma_n)^2}\right\}$$

$$b_1 = -\frac{1}{4}\left\{\frac{\sin 2r_0}{(\sigma_x)^2 + (\sigma_n)^2} + \frac{\sin 2r_0}{(\sigma_y)^2 + (\sigma_n)^2}\right\}$$

$$c_1 = \frac{1}{2}\left\{\frac{\sin^2 r_0}{(\sigma_x)^2 + (\sigma_n)^2} + \frac{\cos^2 r_0}{(\sigma_y)^2 + (\sigma_n)^2}\right\}$$

$$a_2 = \frac{1}{2}\left\{\frac{\cos^2 r_0}{(\sigma_x)^2 + (\sigma_b)^2} + \frac{\sin^2 r_0}{(\sigma_y)^2 + (\sigma_b)^2}\right\}$$

$$b_2 = -\frac{1}{4}\left\{\frac{\sin 2r_0}{(\sigma_x)^2 + (\sigma_b)^2} + \frac{\sin 2r_0}{(\sigma_y)^2 + (\sigma_b)^2}\right\}$$

$$c_2 = \frac{1}{2}\left\{\frac{\sin^2 r_0}{(\sigma_x)^2 + (\sigma_b)^2} + \frac{\cos^2 r_0}{(\sigma_y)^2 + (\sigma_b)^2}\right\}$$

where x_0 is again the x-position of the center, y_0 is again the y-position of the center, *dec* is the declination of the source, r_0 is the rotation angle of the function in degrees counter-clockwise from the positive y axis, σ_x is the width in the x-direction of the Gaussian function, σ_y is the width in the y-direction of the Gaussian function, σ_n is the width of the narrow component of the Gaussian used to define the PSF, and σ_b is the width of the broad component of the Gaussian used to define the PSF.

6.1.3.9 Likelihood Ratio Testing

The asymmetric Gaussian did indeed provide a fit with a higher probability of matching the data than did the symmetric Gaussian. However, the asymmetric Gaussian had additional degrees of freedom, so it is not surprising that it provided a better fit. To determine whether or not these additional degrees of freedom are justified by the result, a likelihood ratio test was performed (see, e.g., [235] for a detailed description). This test calculates the χ^2 value of the ratio of the likelihoods of the two hypotheses in question:

$$\lambda = \frac{L_0}{L_1}$$

$$\chi^2 = -2 \ln \lambda$$

and compares the result to a χ^2 percentile distribution with k degrees of freedom, where k is the difference in the number of free parameters between the two models under consideration (in the case of this analysis, $k = 3$). If the calculated χ^2 value is smaller than the χ^2 percentile distribution value chosen by the analyst for comparison, then the extra degrees of freedom are statistically justified.

The fit to a point source convolved with the instrument PSF gave a probability of goodness of fit of 0.0116 (L_0), whereas the asymmetric Gaussian convolved with the instrument PSF gave a probability of goodness of fit of 0.0193 (L_1). The χ^2 value of the ratio of likelihoods is then calculated to be 1.023, corresponding to a probability of 0.80 and a statistical significance of 0.25σ for 3 degrees of freedom. For justification of the extra degrees of freedom at the 3σ level, the χ^2 of the ratio of likelihoods would need a corresponding probability of 0.0027 or lower. Clearly, the extra degrees of freedom provided by the asymmetric fit are not justified at the required level, and so the best fit is a symmetric 2-D Gaussian point source convolved with the instrument PSF.

6.2 Fermi Data on Tycho

In January 2012, the first detection of Tycho's SNR in the MeV-GeV energy range was published [236]. Data from nearly three years of observations with the

Fermi-LAT revealed weak high energy gamma-ray emission from the remnant. The authors found that a simple π^0-decay model was sufficient to fit the observed radio through TeV spectrum.

The *Fermi* Tycho detection included the first 34 months of sky-survey data taken with the LAT. Events included were in the energy range 400 MeV to 100 GeV. The relatively high minimum energy, above the 70 MeV that would reveal any crucial "bump" in the spectrum, was chosen to minimize the interference of low-energy photons that constitute the bulk of the diffuse emission in and around the Galactic plane (Tycho sits only 1.4° above the plane). Additionally, the analysis included only photons with an Earth zenith angle greater than 105° in order to minimize contamination from gamma rays produced by cosmic rays interacting with Earth's upper atmosphere. This cut is standard in most analyses of *Fermi* data.

The excess emission from Tycho was quantified by its likelihood Test Statistic (TS). The TS was determined by accounting for all contributions from diffuse and point sources except for Tycho; the remaining excess at the position of Tycho has TS = 33, corresponding to a statistical excess of $\sim 5\sigma$. The *Fermi*-LAT source localization included events with energy > 1 GeV, and is centered at RA: 00h 25m 37.00s, Dec: +64° 06' 56.″0. The 95% error ellipse is shown in Figure 6.7. Recall when viewing this map that the angular resolution of *Fermi* is 0.5° at 1 GeV. The integral flux from Tycho in the 400 MeV to 100 GeV energy range was measured to be $(3.5 \pm 1.1_{stat} \pm 0.7_{sys}) \times 10^{-9}$ cm^{-2} s^{-1}.

6.3 Spectral Energy Distribution

6.3.1 TeV Spectrum of Tycho's SNR

The spectrum resulting from the 2008-2010 VERITAS data on Tycho's SNR is shown in Figure 6.8. The data were best fit by a power law of the form

$$\frac{dN}{dE} = C\left(\frac{E}{3.42TeV}\right)^{-\Gamma}$$

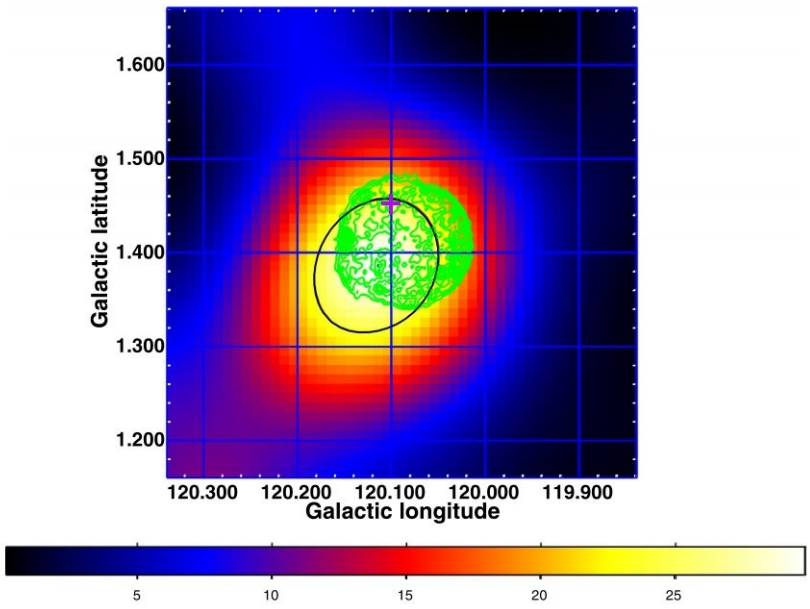

Figure 6.7: Adapted from figure 2 from [236]. ©AAS. Reproduced with permission. "*Fermi*-LAT TS map zoomed in. The green contours are 4.5 keV-5.8 keV continuum band from *XMM-Newton* ([237]) and the black line denotes the 95% confidence area for the *Fermi*-LAT position." Purple cross shows the best fit position of the VERITAS excess from 2008-2010 data; the lengths of the bars represent 1σ statistical errors on the position.

Energy (TeV)	dE (TeV)	Differential Flux (cm^{-2} s^{-1} TeV^{-1})
1.58	1.51	$(7.96 \pm 3.23) \times 10^{-14}$
3.98	3.80	$(8.78 \pm 4.80) \times 10^{-15}$
10.00	9.54	$(2.45 \pm 1.24) \times 10^{-15}$

Table 6.2: The differential flux points in the 1-10 TeV spectrum of Tycho data from 2008-2010.

where $C = (1.55 \pm 0.43_{stat} \pm 0.47_{sys}) \times 10^{-14}$ cm^{-2} s^{-1} TeV^{-1} and $\Gamma = 1.95 \pm 0.51_{stat} \pm 0.30_{sys}$. The integrated flux above 1 TeV is $(1.87 \pm 0.51_{stat}) \times 10^{-13}$ cm^{-2} s^{-1}, equivalent to 0.9±0.2% of the steady flux of the Crab Nebula above the same energy. Table 6.2 lists the differential flux points shown in the spectrum.

The systematic errors on the spectral index and normalization are determined through studies done with simulations [238]. A variety of factors introduce uncertainties into measurements (e.g., modeling atmospheric conditions; modeling of the physics of particle interactions; modeling of the instrument optics, pointing, photon collection efficiency, and digital pulse size and shape; uncertainties in the analysis related to calculating dead time, background models, and gamma/hadron separation cuts; etc.). These effects are studied by changing one factor at a time (e.g., modeling a tropical atmosphere instead of a desert climate) and comparing the results to the results from standard models. It was found that overall, there is ∼30% uncertainty in the flux normalization and ∼15% uncertainty in the spectral index.

The spectrum resulting from the 2008-2011 VERITAS data on Tycho's SNR is shown in Figure 6.9. The data were best fit by a power law of the same form as above. Here, $C = (1.34 \pm 0.37_{stat} \pm 0.40_{sys})$ x 10^{-14} cm^{-2} s^{-1} TeV^{-1} and $\Gamma = 1.94 \pm 0.41_{stat} \pm 0.29_{sys}$. The differential flux points comprising the spectrum are shown in Table 6.3. The integrated flux above 1 TeV was found to be $(1.478 \pm 0.436_{stat})$ x 10^{-13} cm^{-2} s^{-1}, corresponding to 0.7±0.2% of the steady flux of the Crab Nebula above the same energy. All of these measurements agree within errors with the measurements from the 2008-2010 dataset.

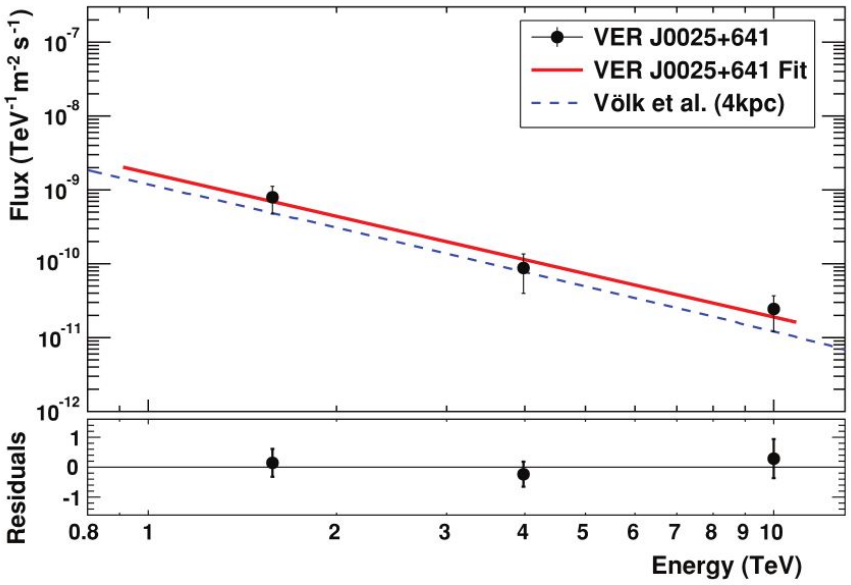

Figure 6.8: Figure 2 from [29]. ©AAS. Reproduced with permission. The differential gamma-ray photon spectrum of VERITAS data on Tycho collected from 2008-2010. Error bars represent 1σ statistical errors. The solid red line shows the result of a power-law fit to the data. The lower panel shows the residuals from this fit. The dashed blue line represents the hadronic model from Völk, Berezhko, and Ksenofontov [20], scaled to a distance of 4 kpc. VER J0025+641 was the name given to the newly-discovered TeV gamma-ray source positionally coincident with Tycho's SNR; the name refers to the detecting instrument (VERITAS) and the source's location measured in Right Ascension and Declination.

Energy (TeV)	dE (TeV)	Differential Flux (cm^{-2} s^{-1} TeV^{-1})
1.58	1.51	$(5.74 \pm 2.57)\times10^{-14}$
3.98	3.80	$(1.06 \pm 0.453)\times10^{-14}$
10.00	9.54	$(1.54 \pm 0.954)\times10^{-15}$

Table 6.3: The differential flux points in the 1-10 TeV spectrum of Tycho data from 2008-2011.

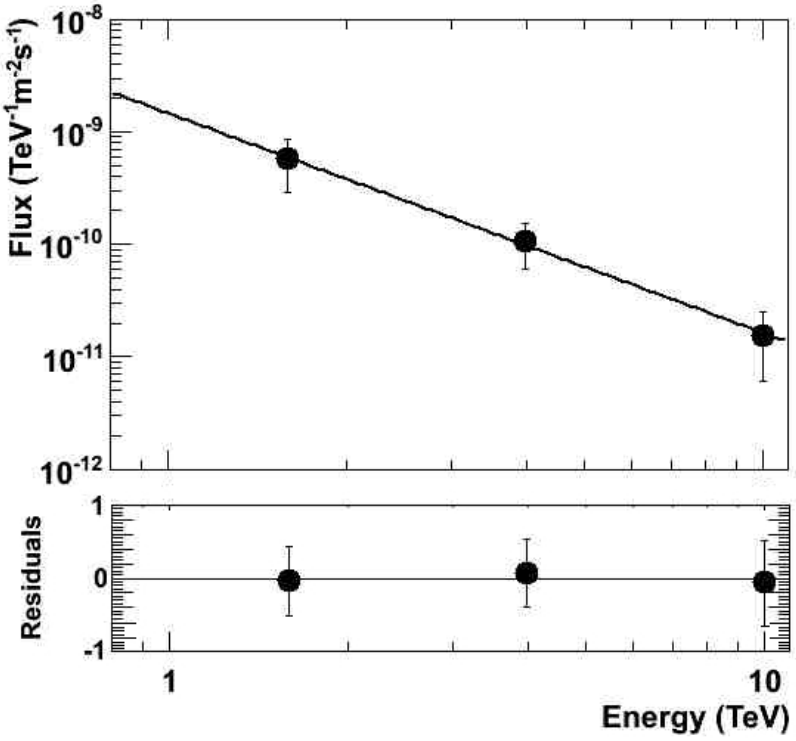

Figure 6.9: The differential gamma-ray photon spectrum of VERITAS data on Tycho collected from 2008-2011. Error bars represent 1σ statistical errors. The black line shows the result of a power-law fit to the data. The lower panel shows the residuals from this fit.

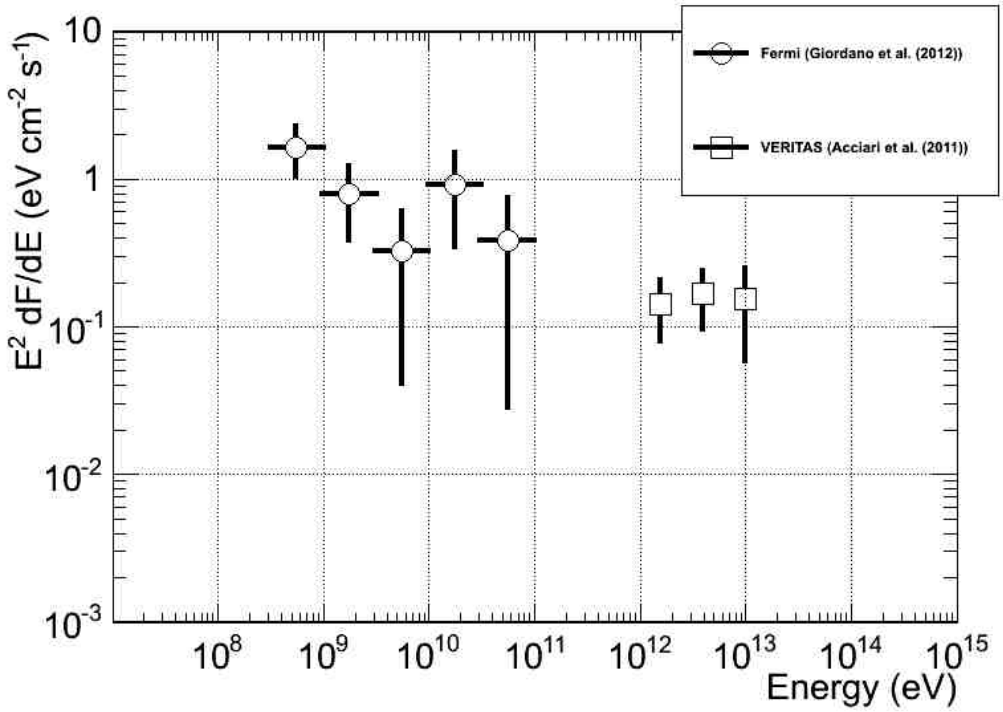

Figure 6.10: Adapted from figure 2 of [239]. The SED data points from *Fermi*-LAT [236] and VERITAS [29] detections of Tycho's SNR. Modeling of the data will be discussed in Chapter 7.

6.3.2 GeV Spectrum of Tycho's SNR

The GeV through TeV SED of Tycho's SNR is shown in Figure 6.10. The spectral index of the best power-law fit to the data from 400 MeV to 100 GeV is $2.3 \pm 0.2_{stat} \pm 0.1_{sys}$. Modeling of the emission will be discussed in the following chapter.

Chapter 7

MODELS, INTERPRETATIONS, AND FUTURE WORK

7.1 Models of MeV-TeV Emission from Tycho's Supernova Remnant

Considering its status as a well-studied historical Type Ia SNR, Tycho is a near-ideal candidate to study CR acceleration. Even before the detection of TeV emission from this remnant, many models of the anticipated emission were proposed. In the paper detailing the TeV detection, we employed relatively simple models created by co-author P. Slane [240]. These models attempted to identify the emission as being of either hadronic or leptonic origin (see Figure 7.1). In either a hadronic or leptonic emission scenario, it is important to remember that both protons and electrons are present, and will contribute to the overall gamma ray emission. The difficulty lies in establishing which population of particles is responsible for the dominant component of the emission. Our models assumed no interaction between the SNR and the MC. One model assumed the TeV emission was due to IC scattering of electrons off the cosmic microwave background. The other assumed the emission originated from neutral pion decay. Both of the models were able to fit the data within the relatively large error bars. These, as well as models by other authors, will be discussed in detail in this chapter. Recall that at the time of the publication of the TeV detection, the MeV - GeV emission was not yet detected.

7.1.1 Modeling of Hadronic Emission

In modeling the TeV emission from Tycho as hadronic in the paper announcing the detection [29], the spectral shape of protons undergoing π^0 decay was assumed, and the normalization was adjusted to match the observed data points. The normalization of the electron spectrum was then adjusted to allow the hadronic emission to dominate.

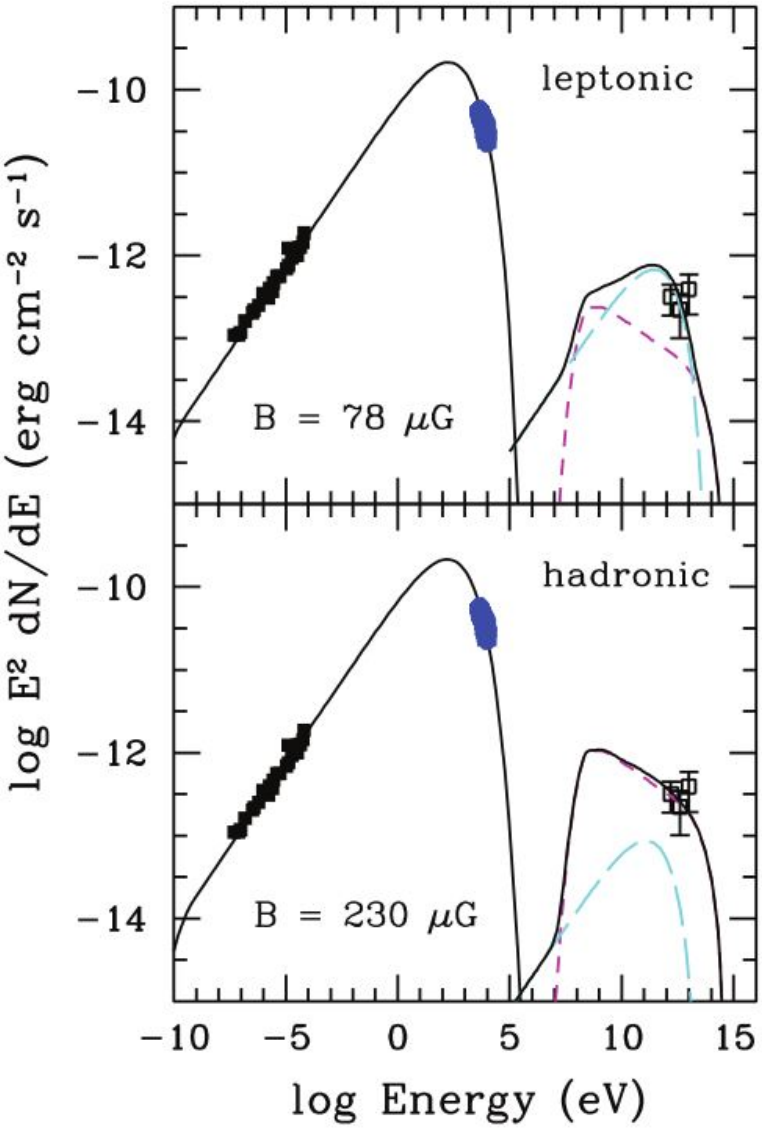

Figure 7.1: Figure 3 from [29]. ©AAS. Reproduced with permission. "Radio, (non-thermal) X-ray, and very high energy gamma-ray emission from *Tycho*'s SNR, along with models for the emission. The upper panel shows a lepton-dominated model, while the lower panel shows a model dominated by hadrons. In each, the IC emission corresponds to the (cyan) long-dashed curve, while the pion-decay emission corresponds to the (magenta) short-dashed curve. The solid curve at high energies is the sum of these components; at lower energies it corresponds to the synchrotron emission."

This resulted in an electron-to-proton ratio $\kappa_{ep} \simeq 4$ x 10^{-4}. Then, the magnetic field required to reproduce the observed synchrotron emission was calculated, and it was found that a minimum of ~230 μG is required, comparable to values found using other models (see [29] and references therein). The calculations assumed no interaction between the remnant and the nearby molecular cloud, but it is noted that involvement of the cloud as target material for hadronic interactions reduces the total particle energy requirements of the model. At the time of publication, a leptonic model fit the data equally well; this model will be discussed in Section 7.1.2 of this chapter.

The authors of the *Fermi* detection paper found that a hadronic origin for the emission provided the best explanation for their observations [236] (see Figure 7.2). They assume efficient acceleration of protons at the SNR shock front, producing a population of protons with the same power-law spectrum and spectral index (2.2-2.3) as the electrons present, but with a much higher cutoff energy ($E_{p,max} = 44 D_{kpc}^2$ TeV for a downstream magnetic field of 215 μG, where $E_{p,max}$ is the maximum proton cutoff energy and D_{kpc} is the distance in kpc; the cutoff energy for electrons was 6-7 TeV). They had the advantage of the TeV detection when forming their models; the TeV data indicates no cutoff. This implies that particle acceleration continues through the present age of the remnant. The gas density required behind the shock front to reproduce the emission in this model is $\sim 3 n_H$, where n_H is the ambient density[1], and the authors assume a modest 10% efficency in the transfer of energy from the shock to the proton population. Thus, a standard neutral pion decay model explains the GeV-TeV emission in a way consistent with all multiwavelength observational constraints.

Soon after the *Fermi* detection was announced, Morlino and Caprioli [241] published a model of emission from Tycho. They used a semi-analytical NLDSA model including magnetic field amplification due to the presence of CRs (see Chapter 2, Section 2.1 for a detailed discussion of this topic). Their model assumes Bohm diffusion[2]

[1] $n_H < 0.3(2.8 kpc/D)^{0.5} cm^{-3}$, where D is the distance to the remnant in kpc

[2] diffusion of a plasma across a magnetic field

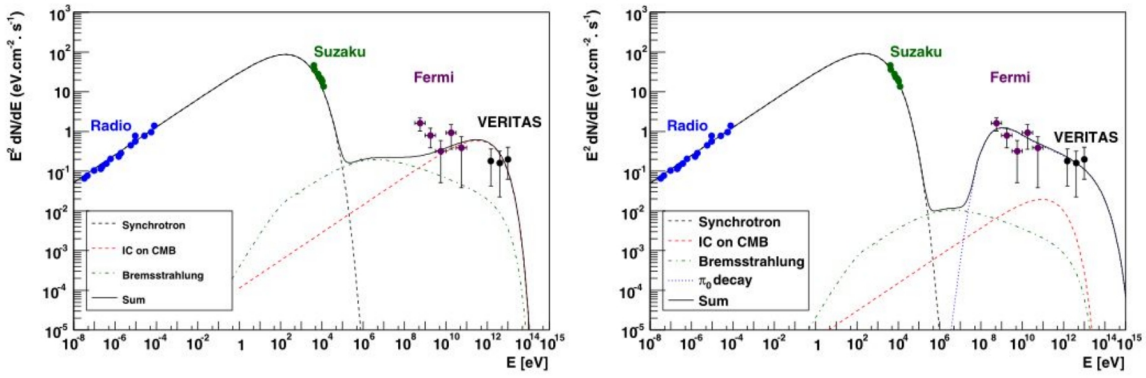

Figure 7.2: Figure 4 from [236]. ©AAS. Reproduced with permission. "Broadband SED model of Tycho's SNR for the far scenario in leptonic model (left) and hadronic interpretation (right)." The text defines the "far" scenario as assuming a distance of 3.5 kpc, leading to an explosion energy of 2 x 10^{51} erg and an ambient density of 0.24 cm^{-3}.

for all particles, and scattering of particles with Alfvén waves[3] as scattering centers. This scattering off Alfvén waves in an enhanced magnetic field leads to a reduced effective compression factor for particles, allowing for a steeper energy spectrum than is expected according to standard models. They conclude that the flux from IC scattering and bremsstrahlung is too low to account for the observed gamma ray SED, and that the shape of the spectrum from these emission mechanisms also does not match the data. In contrast, the SED they find from neutral pion decay matches the data well (see Figure 7.3).

Prior to the detection of GeV and TeV gamma rays from Tycho, researchers Völk, Berezhko, and Ksenofontov produced and refined models of hadronic gamma ray emission in SNRs, and in Tycho's SNR in particular, using the constraints provided by the upper limits on emission available at the time (see, e.g., [243], [244], [20], [245]). In 2013, they published an updated model of the emission from Tycho based on the recent GeV and TeV detections [246]. Their model assumes a warm, clumpy interstellar medium (ISM), where the spatial volume and gas number density of the cooler clumps

[3] magnetohydrodynamic waves in a plasma

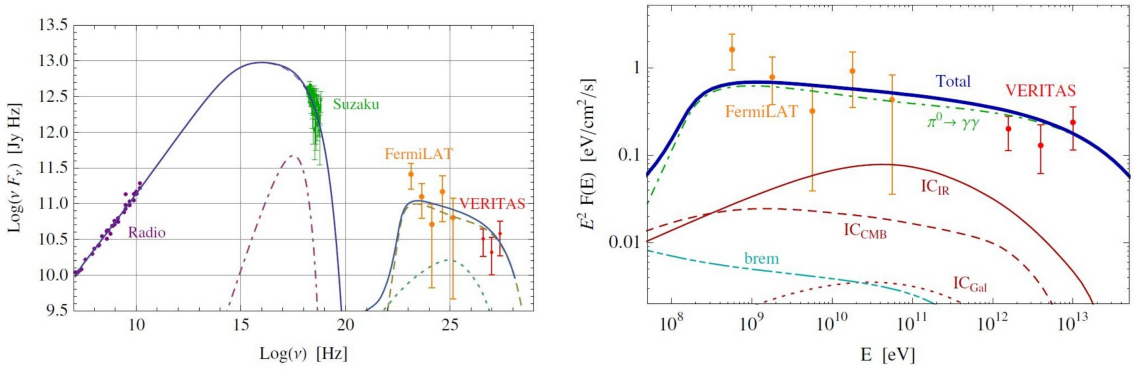

Figure 7.3: Figure 6 (left) and Figure 11 (right) from [241]. Reproduced with permission ©ESO. Left figure: "Spatially integrated spectral energy distribution of Tycho. The curves show synchrotron emission, thermal electron bremsstrahlung and pion decay as calculated within our model. The experimental data are, respectively: radio from Reynolds and Ellison [242]; X-rays from *Suzaku* (courtesy of Toru Tamagawa), GeV gamma-rays from *Fermi*-LAT [236] and TeV gamma-rays from VERITAS [29]. Both *Fermi*-LAT and VERITAS data include only statistical error at 1σ." Right figure: "Gamma-ray emission observed by *Fermi*-LAT and by VERITAS compared with spectral energy distribution produced by pion decay (dot-dashed line), relativistic bremsstrahlung (dot-dot-dashed) and ICS computed for three different photon fields: CMB (dashed), Galactic background (dotted) and IR photons produced by local warm dust (solid). The thick solid line is the sum of all the contributions. Both *Fermi*-LAT and VERITAS data points include only statistical errors at 1σ. For VERITAS data the systematic error is found to be $\sim 30\%$ [29], while for *Fermi*-LAT the systematic uncertainties are comparable to or even larger than the statistical error especially for the lowest energy bins due to difficulties in evaluating the galactic background (see Fig. 3 in [236], and the related discussion)."

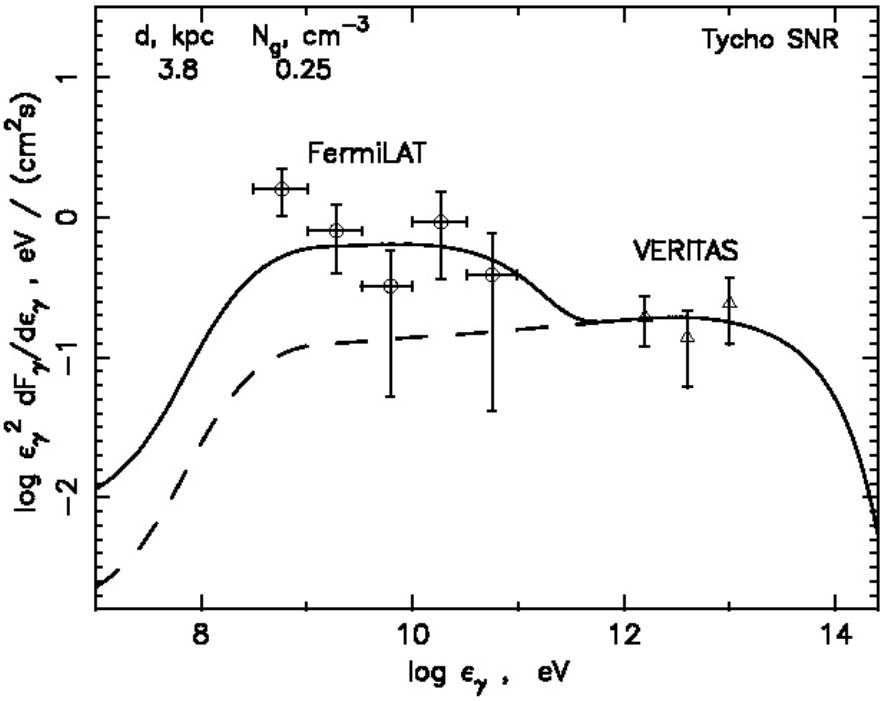

Figure 7.4: Figure 1 from [246]. ©AAS. Reproduced with permission. "Spectral energy distributions of the γ-ray emission from Tycho's SNR as functions of γ-ray energy ϵ_γ, calculated for a source distance $d = 3.8$pc, together with the experimental data obtained by *Fermi* and VERITAS. Dashed and solid lines represent the contribution of the warm-phase ISM and the total γ-ray energy spectrum that includes the contribution of the clouds, respectively."

is much less than that of the warm uniform medium. So, on large scales, the ISM appears warm and uniform. The effect of the clumps is to increase by a factor of $\sim$5 the total gamma ray emission below 100 GeV; their previous model already fit the TeV data well. The SED of gamma ray emission in the MeV-TeV energy range is well-fit by their new model, as shown in Figure 7.4. Furthermore, previous *Chandra* observations had revealed a small amount of thermal X-ray emission in the region just behind the blast wave [247], as well as irregularities in the blast wave itself [64], both of which are consistent with a scenario where the SNR expands into a clumpy medium.

Although Berezhko, Völk, and Ksenofontov reach the same final conclusion that

Morlino and Caprioli did (the gamma ray emission seen from Tycho is likely due to hadrons undergoing neutral pion decay), they had several criticisms of the latter's work. They show that assuming Bohm diffusion for all particles invokes an internal contradiction; the highest energy particles would diffuse with a coefficient approximately ten times that of the Bohm limit, meaning that they largely would not feel the amplified magnetic field and therefore could not gain the momentum that Morlino and Caprioli assume they carry. Additionally, they criticize Morlino and Caprioli's treatment of the large-scale magnetic field near Tycho; Berezko et al. apply, from their study of SN 1006, the idea that only portions of the SNR shock which are quasi-parallel to the magnetic field it expands into will allow for diffusive shock acceleration of particles. This means that only ∼20% of the shock surface efficiently accelerates particles. Morlino and Caprioli ignore this effect. A third criticism is that Morlino and Caprioli do not include nonadiabatic gas heating of the shock precursor, which skews their determination of the shock parameters by overestimating the effect of magnetic field pressure and underestimating the effect of gas pressure. So, although these authors ultimately agree that hadrons are likely responsible for the emission, there is still healthy debate about the exact mechanisms by which the emission is being produced.

Finally, Zhang et al. [248] have proposed a model in which Tycho is interacting with the nearby molecular cloud (MC) (as opposed to the lower-density interstellar medium) to produce emission from accelerated hadrons via neutral pion decay. They assume a distance to the remnant/cloud system of 2.5 kpc (see Chapter 1, Section 1.2 for a review of distance estimates), and a very modest energy conversion efficiency between the shock and the particles of only 1%. They also assume a spectrum with an exponential cutoff. Their calculations lead to a cutoff energy of ∼5.6 TeV for electrons and ∼380 TeV for protons, and an electron-to-proton ratio $\kappa_{ep} \simeq 0.7 \times 10^{-2}$. They note that, unlike other SNRs shown to be interacting with MCs and producing hadronic emission, Tycho is relatively young, and so the protons undergoing the interaction are freshly accelerated, not the result of thousands of years of diffusion out of the remnant. The SED produced by their model is shown in Figure 7.5.

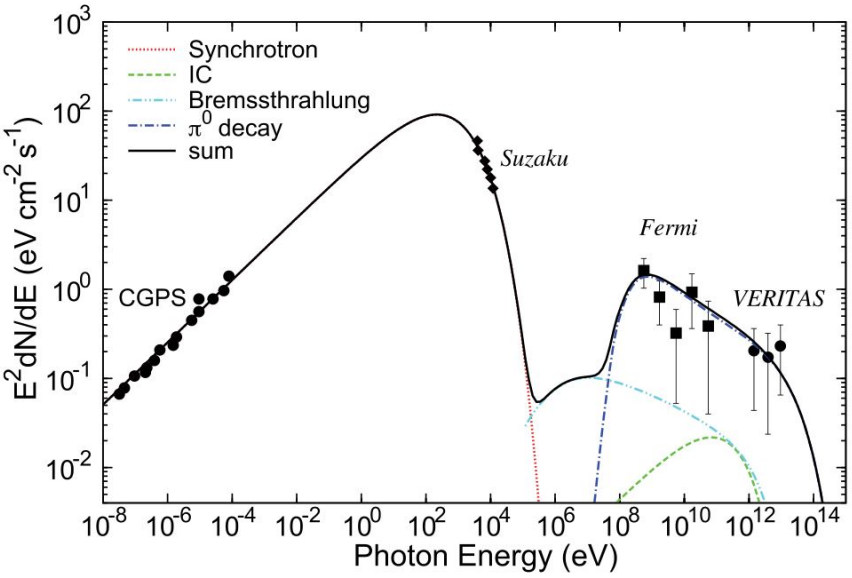

Figure 7.5: Figure 2 from [248]. "Broad-band SED of Tycho's SNR with the observed data in the radio [249], X-rays [250], and γ-rays (*Fermi*:[236], VERITAS: [29])."

7.1.2 Modeling of Leptonic Emission

In the initial publication of TeV emission from Tycho, we also considered a lepton-dominated scenario. To do this, the magnetic field and normalization necessary to reproduce the synchrotron emission seen in radio through X-rays were calculated. Then, IC scattering of cosmic microwave background photons in this environment was modeled. The magnetic field derived for this scenario is $\sim$80μG, with $\sim$15% uncertainty. It is worth noting that this magnetic field, the weaker of the two allowed within the models in the initial publication of a TeV detection, is still significantly higher than the $\sim$3μG typically found in interstellar space. This is additional evidence that magnetic field amplification is occurring in Tycho's SNR.

The authors of the paper detailing the *Fermi* detection considered two mechanisms for electrons to produce the observed emission: bremsstrahlung and IC scattering. For bremsstrahlung to be responsible for the emission, they calculate that the necessary gas density would be $n_H = 9.7$ cm^{-3}. This value is a factor of 30 higher than

the value derived from X-ray observations. The implied SN energy in this scenario is 4.4 x 10^{51} erg, which is rather higher than one would expect from a typical Type Ia SN explosion. In examining IC scattering as a possible origin for the gamma ray emission, the authors calculated the necessary conditions to reproduce the observed gamma ray flux. While the flux could be reproduced at higher energies, the conditions necessary resulted in a flux of bremsstrahlung emission too low to reproduce the MeV portion of the spectrum (since both IC and bremsstrahlung are produced by the same population of particles). Additionally, the shape of the spectrum with IC scattering as the dominant component does not fit the data well.

Although several authors have concluded that a hadronic emission scenario is likely responsible for the observed MeV-TeV emission from Tycho, Atoyan and Dermer [251] have created a model of leptonic emission that also fits the data. Their model features two zones, one narrow zone around the shock front and another zone that occupies most of the SNR interior, each containing a population of electrons. These two zones have different magnetic fields and volume filling factors, with the interior zone having a significantly weaker field and larger volume filling factor. By assuming multiple populations of electrons, they were able to reproduce the observed data points in both the *Fermi* and VERITAS spectra (see Figure 7.6). They restrict their investigation to two zones to illustrate the concept, but note that further division into multiple zones would more realistically represent the environment in a SNR, as well as allowing for additional free parameters to better match observations.

A SED including all models from the authors discussed above is shown in Figure 7.7. Although most literature on Tycho that has been published since the *Fermi* and VERITAS detections were announced concludes that the observed emission is likely from a population of accelerated hadrons, the question has not been firmly settled. Even if the emission is determined to be hadronic in origin, the possiblity of an interaction with the nearby MC (or not) remains open. Spectral measurements near 70 MeV, the energy of the tell-tale pion decay "bump", would be definitive, but will also be very difficult to achieve since Tycho is a weak source in a region bright with diffuse

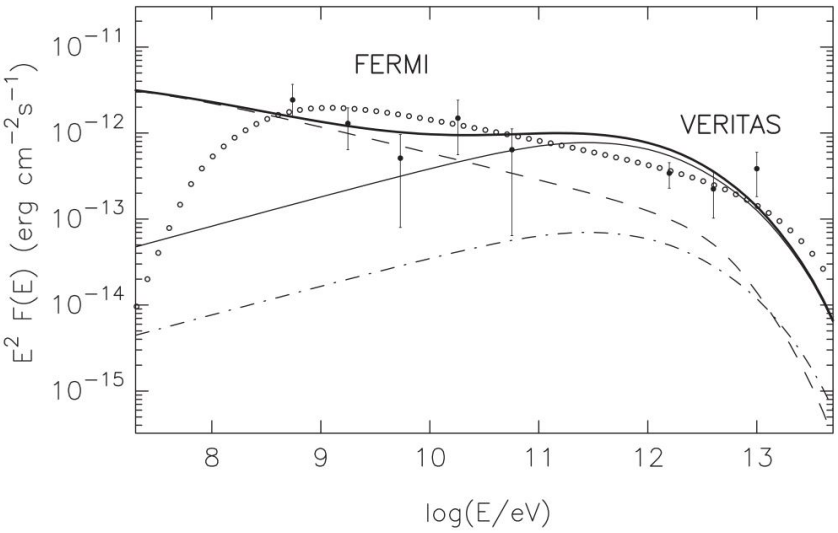

Figure 7.6: Figure 2 from [251]. ©AAS. Reproduced with permission. "γ-ray fluxes in the two-zone model with parameters described in Figure 1 [of [251]]. The heavy solid line shows the total flux of leptonic origin. The total bremsstrahlung and Compton radiation fluxes are shown by dashed and solid (thin) lines, respectively. For comparison, the Compton flux contribution from zone 1 is also shown (dot-dashed line). The open dotted curve shows the flux of hadronic origin calculated for protons with total energy E_p = 3 x 10^{49} erg." The parameters described in Figure 1 are density $n_2 \simeq$3 cm^{-3} at $d_{kpc} = 2.8$, $n_1 \simeq n_2$, $B_1 = 100\mu$G and $B_2 = 34\mu$G, $\eta = 0.2$, $\alpha = 2.31$, and $E_{cut} = 40$TeV.

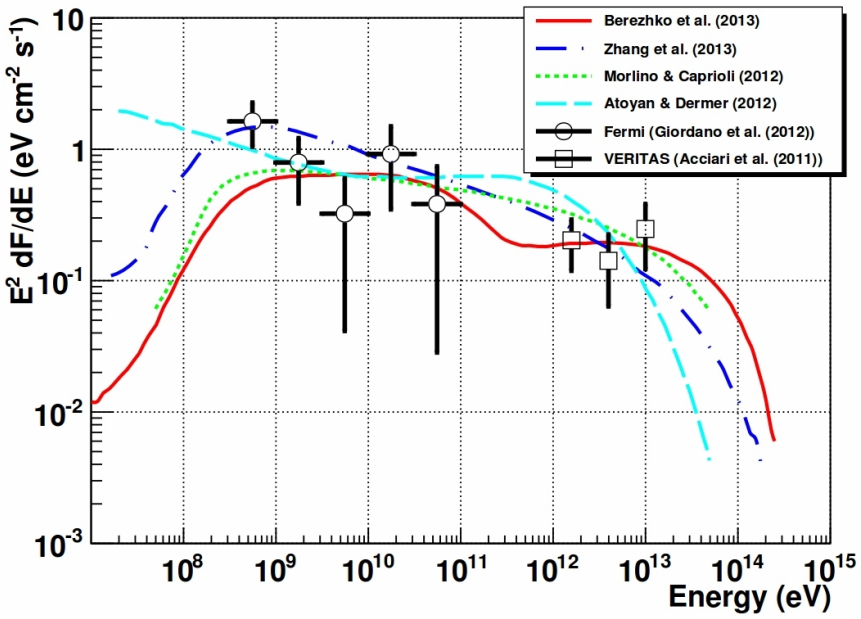

Figure 7.7: Figure 2 from [239]. "Previously published VERITAS [29] and *Fermi*-LAT data [236] with various models. The red solid line shows the model of Berezhko et al. [246], for the case of gamma-ray production in a clumpy ISM. Zhang et al.'s model [248] is plotted as blue dotted line, showing the case of emission mainly coming from MC. Morlino & Caprioli's model [241] appears as a green dotted line, representing CR production in a homogeneous ISM. The cyan dashed line represents the case of a pure leptonic model with multiple emission zones [251]."

emission. A more realistic approach would be to improve the statistics, and hence the spectral measurement, at high energies. This could conclusively determine whether hadrons in Tycho's SNR are truly being accelerated to energies near the "knee" of the CR spectrum.

7.2 Summary of Results

The first detection of TeV gamma rays from Tycho's SNR was published in April 2011 by the VERITAS collaboration [29]. The detection resulted from a total of 66.7 hours of observations between October 2008 and January 2010. Approximately the first 1/3 of the data were taken in the original, less sensitive array configuration,

and the remaining (approximately 2/3) were taken in the current, more sensitive array configuration resulting from the relocation of telescope T1.

The detection was significant at the 5.0σ level, post-trials. The integrated flux above 1 TeV was found to be $(1.87 \pm 0.51_{stat})$ x 10^{-13} cm^{-2} s^{-1}, equivalent to $\sim$0.9% of the steady flux from the Crab Nebula above the same energy. The spectrum was found to be compatible with a simple power law with spectral index $\Gamma = 1.95 \pm 0.51_{stat} \pm 0.30_{sys}$. Models of both hadronic and leptonic emission were able to fit the data within its relatively large statistical error bars.

The morphology of the TeV emission is interesting. There is a possibility that the northeastern portion of the remnant is interacting with a pre-existing molecular cloud, which would provide target material for accelerated hadrons to interact with to produce TeV gamma rays through neutral pion decay. To add further fuel to this scenario, the best-fit centroid position of the TeV emission is offset from the remnant center towards the molecular cloud. However, the evidence regarding the cloud interaction is inconclusive at present, and the offset of the TeV centroid is not significant (1.6σ).

VERITAS observed Tycho for an additional 22.4 hours between September 2010 and January 2011. The addition of this data to the original dataset does increase then number of events available for analysis, thus improving the statistical significance of calculations, but it does not significantly change the previous conclusions.

In January 2012, the first detection of MeV-GeV gamma rays from Tycho's SNR was published using *Fermi*-LAT data [236]. The addition of these lower energy data points to the Tycho SED allowed for much better constrained modeling than did the TeV points alone. The authors of the *Fermi* detection paper conclude that the MeV-TeV emission is likely hadronic in origin, and subsequent models produced by other authors agree (see [241], [246], and [248]). However, it is also possible to fit the MeV-TeV data with a model of leptonic emission [251]. The lowest energy photons included in the *Fermi* analysis were at 400 MeV, above the crucial 70 MeV where a "bump" in the spectrum would unequivocally reveal the presence of hadronic emission.

This threshold was chosen to minimize the interference of low-energy diffuse Galactic emission. As both the *Fermi* spacecraft and VERITAS continue to collect data, improved statistics in MeV-TeV energy bands should allow for eventual determination of the particles responsible for the observed emission. This will be crucial evidence in the search for the origin of cosmic rays.

7.3 Future Work

Both VERITAS and *Fermi* are continuing observations of Tycho's SNR. Based on measurements to date, it is possible to estimate what the spectral measurement from each instrument will look like by the end of the instrument's lifetime. For VERITAS, I assume a total data set on Tycho of 150 usable hours by the end of the instrument's lifetime. This represents an additional ∼60 hours beyond the 2010-2011 data set[4]. I then used the measured flux in each energy bin to estimate how much the existing error bars would be reduced after 150 hours of observation, and fit a power-law spectrum to the spectral data points with the estimated errors. The measured and estimated spectra are shown in Figure 7.8, and the estimated errors on the flux are given in Table 7.1. The data with estimated errors are fit by a power law of the form

$$\frac{dN}{dE} = C\left(\frac{E}{3.42TeV}\right)^{-\Gamma}$$

where $C = (1.57 \pm 0.33_{stat} \pm 0.47_{sys})$ x 10^{-14} cm^{-2} s^{-1} TeV^{-1} and $\Gamma = 1.94 \pm 0.34_{stat} \pm 0.29_{sys}$. These values are in agreement with the published values within errors. The statistical error bars on the normalization constant (C) are reduced by 25% compared to the published value, and those on the spectral index (Γ) are reduced by 29%.

A similar estimate can be made for the predicted spectrum of Tycho as seen by the *Fermi*-LAT after 10 years of operations (the anticipated mission lifetime). Based on the error bars provided in Giordano, et al. [236] for 34 months of data, a 53%

[4] Although additional data may produce enough statistics at higher and lower energies to extend the spectral measurement, errors on the current spectral data points are reduced approximately by a factor of $\sqrt{time}$, meaning that additional observations produce diminishing returns.

Energy (TeV)	dE (TeV)	Differential Flux and Estimated Errors (cm^{-2} s^{-1} TeV^{-1})	Percentage Reduction in Measured Error
1.58	1.51	$(7.96 \pm 2.38) \times 10^{-14}$	14.9%
3.98	3.80	$(8.78 \pm 3.78) \times 10^{-15}$	21.6%
10.00	9.54	$(2.45 \pm 0.90) \times 10^{-15}$	18.4%

Table 7.1: The estimated errors on differential flux points in the 1-10 TeV spectrum of Tycho data after 150 hours of observations.

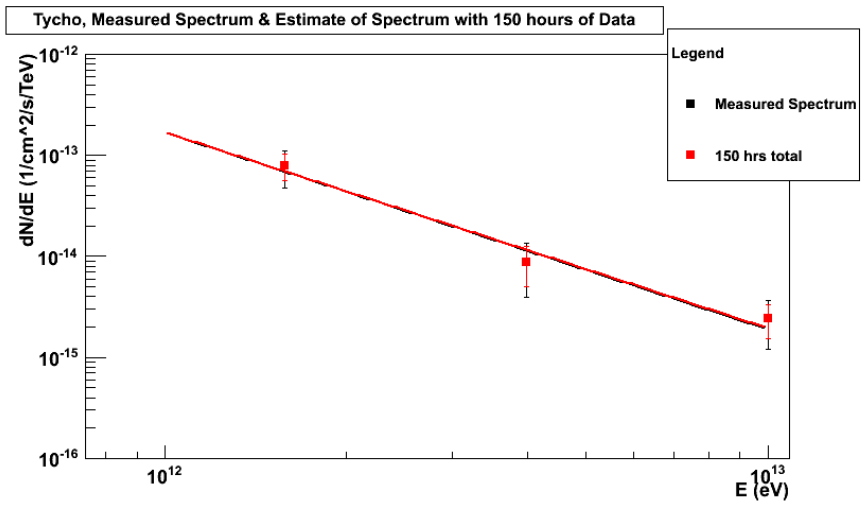

Figure 7.8: The published TeV SED of Tycho's SNR, and the estimated TeV SED of Tycho's SNR after 150 hours of observations.

reduction in the error bars can be expected after 10 years using the $\sqrt{time}$ method of estimation. Figure 7.9 shows the measured and predicted spectra from *Fermi*-LAT and VERITAS data, along with the models discussed previously in this chapter.

Although the reduction in the existing spectral error bars with additional observations, particularly in the *Fermi*-LAT energy range, is not negligible, it does not appear that additional data from this generation of instruments will easily be able to firmly exclude any of the proposed models to explain the emission. However, additional observations could still be useful; besides providing improved statistics at higher and lower energies, the upgraded VERITAS cameras have improved the instrument's sensitivity in these ranges. Additionally, advanced analysis techniques are under development which will improve the sensitivity of the analysis. An extension of the TeV spectrum of Tycho's SNR is possible, and might begin to rule out some of the proposed models. And even if the knowledge to be gleaned from Tycho's SNR is limited with current instrumentation, other, brighter SNRs can still be observed, improving our understanding of the processes at work in this class of objects as a whole.

The next generation of IACT is already being designed, and prototypes are

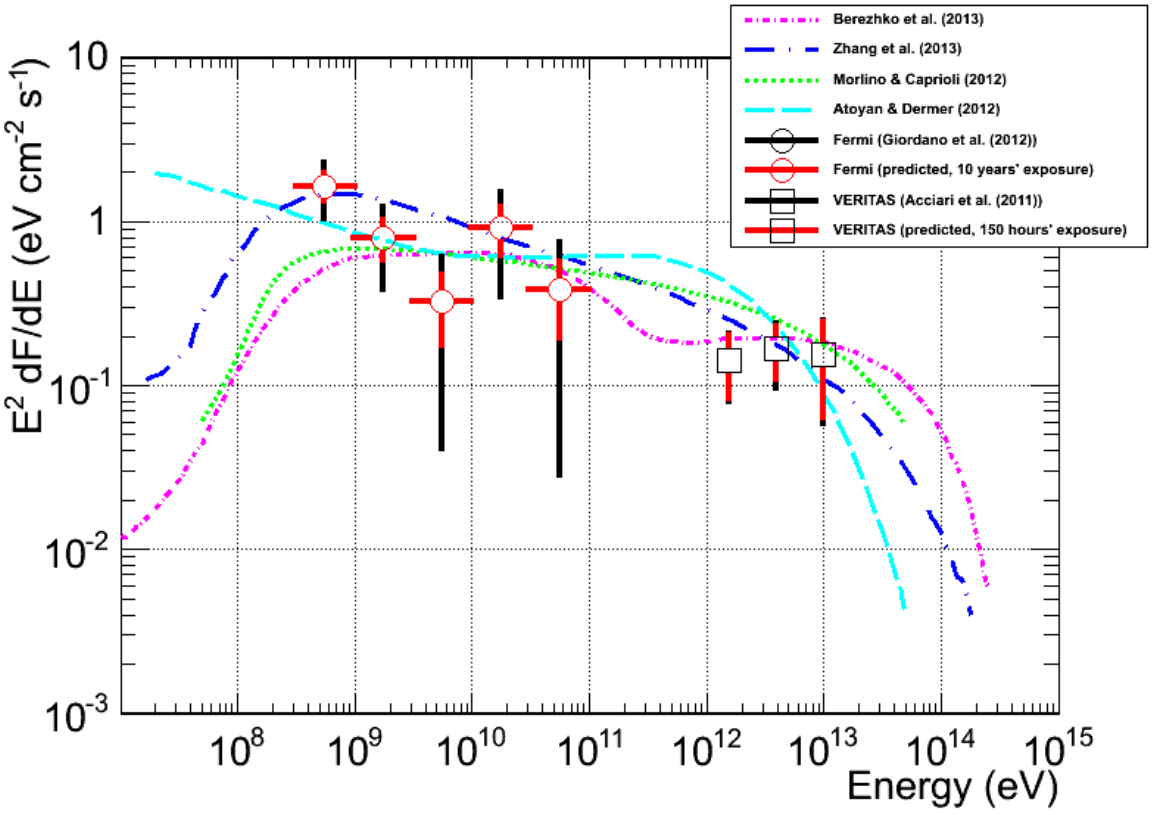

Figure 7.9: Adapted from figure 2 of [239]. The measured spectrum of Tycho's SNR from *Fermi*-LAT and VERITAS data (black data points and error bars), the predicted errors on the spectral points after 10 years (*Fermi*-LAT) and 150 hours (VERITAS) of observations (red error bars), and the models discussed in this chapter.

being tested. The Cherenkov Telescope Array (CTA) is proposed to be the most extensive IACT ever to operate. It will include two physical arrays, one in the Northern hemisphere and one in the Southern hemisphere, to provide all-sky coverage. Each site will include arrays of small (4-6 m diameter), medium (12 m diameter), and large (23 m diameter) telescopes to provide sensitivity to a broad range of energies. The energy coverage is expected to extend from ∼20 GeV [252] to >100 TeV [253]. This instrument will surely lead to new scientific discoveries, and deeper understanding of the universe we live in.

7.4 Summary of Original Work and Conclusion

The author was involved in the entire process of achieving the VHE detection of Tycho's SNR. Beginning with weeks-long observing shifts at the VERITAS site in Arizona to operate the telescopes and collect data, I then completed the analysis of the data. I also wrote an additional piece of software to perform morphological studies on the final result; this tool was then made available to the VERITAS collaboration for general use. Finally, I co-wrote the paper announcing the detection, including editing and revisions of both the text and figures, and went on to present the result in both talk and poster formats at national conferences, and at the Fermi Summer School.

The detection of TeV gamma rays from Tycho's SNR provides a key piece in the cosmic ray origin puzzle. Tycho, being one of only a very few historical SNRs, has been observed across the electromagnetic spectrum for decades. As a young remnant likely expanding into a clean environment, it provides a nearly ideal natural laboratory to test the hypothesis of cosmic ray acceleration at SNR shock fronts, and so extensive and detailed models have been developed. Indeed, within the past decade, the evidence of accelerated particles present in Tycho's SNR has become increasingly convincing. The detection of TeV emission provides unrefutable evidence that particles are being accelerated to at least TeV energies in this remnant. Additionally, the observed SED of TeV emission from Tycho requires the presence of magnetic fields amplified by at

least an order of magnitude above typical interstellar magnetic field strengths; this, too, points directly to the acceleration of cosmic rays in this remnant.

While the nature of the particles being accelerated in Tycho's SNR has yet to be firmly determined, it remains one of only a few SNRs to demonstrate evidence of particle acceleration at all. As the high-energy telescopes suited to probe this topic continue to improve in sensitivity, this situation will likely change. In the current era, however, anything we learn about particle acceleration at any SNR shock front provides extremely valuable information for refining models of the processes we think are at work. VERITAS, *Fermi*, and their successors will certainly continue to study SNRs as the likely birthplace of Galactic cosmic rays, and these models will continue to be refined. Although great strides have been made in solving the mystery of cosmic ray origins, the case is far from closed.

BIBLIOGRAPHY

[1] R. Ball. *Great Astronomers*. Ibister and Company Limited, 1895.

[2] D. A. Green and F. R. Stephenson. Historical Supernovae. In K. Weiler, editor, *Supernovae and Gamma-Ray Bursters*, volume 598 of *Lecture Notes in Physics, Berlin Springer Verlag*, pages 7–19, 2003.

[3] D. W. Olson, M. S. Olson, and R. L. Doescher. The stars of Hamlet. *Sky & Telescope*, 96(5):68–73, November 1998.

[4] Tycho Brahe. *Nova et Nvllivs Ævi Memoria Privs Vis a Stella, iam pridem Anno á nato Christo 1572*. 1573.

[5] Mercury poisoning ruled out as cause of Danish astronomer Tycho Brahe's death. http://phys.org/news/2012-11-mercury-poisoning-tycho-brahe-death.html.

[6] J.L.E. Dreyer. *Tycho Brahe: A Picture of Scientific Life and Work in the Sixteenth Century*. Adam and Charles Black, 1890.

[7] D. Bilefsky. After 400 Years, Still Hot on the Trail. http://www.nytimes.com/2010/11/20/world/europe/20iht-prague.html, 2010.

[8] O. Krause, et al. Tycho Brahe's 1572 supernova as a standard typeIa as revealed by its light-echo spectrum. *Nature*, 456:617–619, December 2008.

[9] B. Wang and Z. Han. Progenitors of type Ia supernovae. *New Astronomy Reviews*, 56:122–141, June 2012.

[10] P. A. Mazzali, F. K. Röpke, S. Benetti, and W. Hillebrandt. A Common Explosion Mechanism for Type Ia Supernovae. *Science*, 315:825–, February 2007.

[11] M. M. Phillips. The absolute magnitudes of Type IA supernovae. *Astrophysical Journal Letters*, 413:L105–L108, August 1993.

[12] R. Scalzo, et al. Type Ia supernova bolometric light curves and ejected mass estimates from the Nearby Supernova Factory. *ArXiv e-prints*, 1402.6842, February 2014.

[13] R. C. Smith, R. P. Kirshner, W. P. Blair, and P. F. Winkler. Six Balmer-dominated supernova remnants. *Astrophysical Journal*, 375:652–662, July 1991.

[14] R. C. Smith, R. P. Kirshner, W. P. Blair, and P. F. Winkler. Six Balmer-dominated Supernova Remnants: Erratum. *Astrophysical Journal*, 384:665, January 1992.

[15] W. M. Goss, U. J. Schwarz, and P. R. Wesselius. The Distance to Tycho's Supernova (3 C 10) and the Nature of 3 C 58. *Astronomy & Astrophysics*, 28:305, October 1973.

[16] R. A. Chevalier, R. P. Kirshner, and J. C. Raymond. The optical emission from a fast shock wave with application to supernova remnants. *Astrophysical Journal*, 235:186–195, January 1980.

[17] J. S. Albinson, R. J. Tuffs, E. Swinbank, and S. F. Gull. Neutral hydrogen towards 3C 10, the remnant of Tycho's supernova. *Monthly Notices of the Royal Astronomical Society*, 219:427–439, March 1986.

[18] U. J. Schwarz, W. M. Goss, P. M. Kalberla, and P. Benaglia. WSRT and VLA observations of HI in the direction of 3C 10. *Astronomy & Astrophysics*, 299:193, July 1995.

[19] A. Hayato, et al. Expansion Velocity of Ejecta in Tycho's Supernova Remnant Measured by Doppler Broadened X-ray Line Emission. *Astrophysical Journal*, 725:894–903, December 2010.

[20] H. J. Völk, E. G. Berezhko, and L. T. Ksenofontov. Internal dynamics and particle acceleration in Tycho's SNR. *Astronomy & Astrophysics*, 483:529–535, May 2008.

[21] E. A. Helder, et al. Measuring the Cosmic-Ray Acceleration Efficiency of a Supernova Remnant. *Science*, 325:719–, August 2009.

[22] E. M. Reynoso, P. F. Velázquez, G. M. Dubner, and W. M. Goss. The Environs of Tycho's Supernova Remnant Explored through the H I 21 Centimeter Line. *Astronomical Journal*, 117:1827–1833, April 1999.

[23] E. M. Reynoso, et al. A VLA Study of the Expansion of Tycho's Supernova Remnant. *Astrophysical Journal*, 491:816, December 1997.

[24] J.-J. Lee, B.-C. Koo, and K. Tatematsu. The Environment of Tycho: Possible Interaction with the Molecular Cloud. *Astrophysical Journal Letters*, 605:L113–L116, April 2004.

[25] W. W. Tian and D. A. Leahy. Tycho SN 1572: A Naked Ia Supernova Remnant Without an Associated Ambient Molecular Cloud. *Astrophysical Journal Letters*, 729:L15, March 2011.

[26] J. H. Buckley, et al. Constraints on cosmic-ray origin from TeV gamma-ray observations of supernova remnants. *Astronomy & Astrophysics*, 329:639–658, January 1998.

[27] F. A. Aharonian, et al. A study of Tycho's SNR at TeV energies with the HEGRA CT-System. *Astronomy & Astrophysics*, 373:292–300, July 2001.

[28] E. Carmona, M. T. Costado, L. Font, J. Zapatero, and for the MAGIC Collaboration. Observation of selected SNRs with the MAGIC Cherenkov Telescope. *ArXiv e-prints*, 0907.1009, July 2009.

[29] V. A. Acciari, et al. Discovery of TeV Gamma-ray Emission from Tycho's Supernova Remnant. *Astrophysical Journal Letters*, 730:L20, April 2011.

[30] T.K. Gaisser. *Cosmic Rays and Particle Physics*. Cambridge University Press, 1990.

[31] K. Kotera and A. V. Olinto. The Astrophysics of Ultrahigh-Energy Cosmic Rays. *Annual Review of Astronomy & Astrophysics*, 49:119–153, September 2011.

[32] S. P. Reynolds. Supernova Remnants at High Energy. *Annual Review of Astronomy & Astrophysics*, 46:89–126, September 2008.

[33] T. Stanev. *High Energy Cosmic Rays, Second Edition*. Praxis Publishing, 2010.

[34] S. P. Swordy. The Energy Spectra and Anisotropies of Cosmic Rays. *Space Science Reviews*, 99:85–94, October 2001.

[35] F. Zwicky. Production of Atomic Rays and of Cosmic Rays in Supernovae. *Proceedings of the National Academy of Science*, 25:338–344, July 1939.

[36] J. A. Hinton and W. Hofmann. Teraelectronvolt Astronomy. *Annual Review of Astronomy & Astrophysics*, 47:523–565, September 2009.

[37] Malcolm S. Longair. *High Energy Astrophysics, Volume 2*. Cambridge University Press, 2002.

[38] E. Parizot, J. Paul, and A. M. Bykov. Galactic cosmic rays from supernova remnants: myth or reality? In *International Cosmic Ray Conference*, volume 6 of *International Cosmic Ray Conference*, page 2070, August 2001.

[39] Y. Butt. Beyond the myth of the supernova-remnant origin of cosmic rays. *Nature*, 460:701–704, August 2009.

[40] E. Fermi. On the Origin of the Cosmic Radiation. *Physical Review*, 75:1169–1174, April 1949.

[41] A. R. Bell. The acceleration of cosmic rays in shock fronts. I. *Monthly Notices of the Royal Astronomical Society*, 182:147–156, January 1978.

[42] A. R. Bell and S. G. Lucek. Cosmic ray acceleration to very high energy through the non-linear amplification by cosmic rays of the seed magnetic field. *Monthly Notices of the Royal Astronomical Society*, 321:433–438, March 2001.

[43] S. G. Lucek and A. R. Bell. Non-linear amplification of a magnetic field driven by cosmic ray streaming. *Monthly Notices of the Royal Astronomical Society*, 314:65–74, May 2000.

[44] A. M. Hillas. TOPICAL REVIEW: Can diffusive shock acceleration in supernova remnants account for high-energy galactic cosmic rays? *Journal of Physics G Nuclear Physics*, 31:95, May 2005.

[45] A. A. Abdo, et al. Discovery of Localized Regions of Excess 10-TeV Cosmic Rays. *Physical Review Letters*, 101(22):221101, November 2008.

[46] A. A. Abdo, et al. The Large-Scale Cosmic-Ray Anisotropy as Observed with Milagro. *Astrophysical Journal*, 698:2121–2130, June 2009.

[47] M. G. Aartsen, et al. Observation of Cosmic-Ray Anisotropy with the IceTop Air Shower Array. *Astrophysical Journal*, 765:55, March 2013.

[48] B. Bartoli, et al. Medium scale anisotropy in the TeV cosmic ray flux observed by ARGO-YBJ. *Physical Review D*, 88(8):082001, October 2013.

[49] A. W. Strong, I. V. Moskalenko, and V. S. Ptuskin. Cosmic-Ray Propagation and Interactions in the Galaxy. *Annual Review of Nuclear and Particle Science*, 57:285–327, November 2007.

[50] P. Blasi. Cosmic Ray Acceleration in Supernova Remnants. In S. Giani, C. Leroy, and P. G. Rancoita, editors, *Cosmic Rays for Particle and Astroparticle Physics*, pages 493–506, June 2011.

[51] K. Koyama, et al. Evidence for shock acceleration of high-energy electrons in the supernova remnant SN1006. *Nature*, 378:255–258, November 1995.

[52] G. E. Allen, et al. Evidence of X-Ray Synchrotron Emission from Electrons Accelerated to 40 TeV in the Supernova Remnant Cassiopeia A. *Astrophysical Journal Letters*, 487:L97, September 1997.

[53] P. Slane, et al. RX J0852.0-4622: Another Nonthermal Shell-Type Supernova Remnant (G266.2-1.2). *Astrophysical Journal*, 548:814–819, February 2001.

[54] K. Koyama, et al. Discovery of Non-Thermal X-Rays from the Northwest Shell of the New SNR RX J1713.7-3946: The Second SN 1006? *Publications of the Astronomical Society of Japan*, 49:L7–L11, June 1997.

[55] Y. Uchiyama, F. A. Aharonian, T. Tanaka, T. Takahashi, and Y. Maeda. Extremely fast acceleration of cosmic rays in a supernova remnant. *Nature*, 449:576–578, October 2007.

[56] S. P. Reynolds, et al. The Youngest Galactic Supernova Remnant: G1.9+0.3. *Astrophysical Journal Letters*, 680:L41–L44, June 2008.

[57] K. Torii, et al. Discovery of a Featureless X-Ray Spectrum in the Supernova Remnant Shell of G330.2+1.0. *Publications of the Astronomical Society of Japan*, 58:L11–L14, February 2006.

[58] P. Slane, et al. Nonthermal X-Ray Emission from the Shell-Type Supernova Remnant G347.3-0.5. *Astrophysical Journal*, 525:357–367, November 1999.

[59] F. Aharonian, et al. Primary particle acceleration above 100 TeV in the shell-type supernova remnant RX J1713.7-3946 with deep HESS observations. *Astronomy & Astrophysics*, 464:235–243, March 2007.

[60] F. Aharonian, et al. Primary particle acceleration above 100 TeV in the shell-type supernova remnant RX J1713.7 - 3946 with deep H.E.S.S. observations (Corrigendum). *Astronomy & Astrophysics*, 531:C1, July 2011.

[61] A. A. Abdo, et al. Observations of the Young Supernova Remnant RX J1713.7-3946 with the Fermi Large Area Telescope. *Astrophysical Journal*, 734:28, June 2011.

[62] F. A. Aharonian. Gamma rays from supernova remnants. *Astroparticle Physics*, 43:71–80, March 2013.

[63] F. Aharonian, et al. Discovery of very high energy gamma-ray emission coincident with molecular clouds in the W 28 (G6.4-0.1) field. *Astronomy & Astrophysics*, 481:401–410, April 2008.

[64] J. S. Warren, et al. Cosmic-Ray Acceleration at the Forward Shock in Tycho's Supernova Remnant: Evidence from Chandra X-Ray Observations. *Astrophysical Journal*, 634:376–389, November 2005.

[65] K. A. Eriksen, et al. Evidence for Particle Acceleration to the Knee of the Cosmic Ray Spectrum in Tycho's Supernova Remnant. *Astrophysical Journal Letters*, 728:L28, February 2011.

[66] A. R. Bell. Turbulent amplification of magnetic field and diffusive shock acceleration of cosmic rays. *Monthly Notices of the Royal Astronomical Society*, 353:550–558, September 2004.

[67] M. Ackermann, et al. Detection of the Characteristic Pion-Decay Signature in Supernova Remnants. *Science*, 339:807–811, February 2013.

[68] J. Albert, et al. Discovery of Very High Energy Gamma Radiation from IC 443 with the MAGIC Telescope. *Astrophysical Journal Letters*, 664:L87–L90, August 2007.

[69] V. A. Acciari, et al. Observation of Extended Very High Energy Emission from the Supernova Remnant IC 443 with VERITAS. *Astrophysical Journal Letters*, 698:L133–L137, June 2009.

[70] T. Kamae, N. Karlsson, T. Mizuno, T. Abe, and T. Koi. Parameterization of γ, $e^{+/-}$, and Neutrino Spectra Produced by p-p Interaction in Astronomical Environments. *Astrophysical Journal*, 647:692–708, August 2006.

[71] M. Mori. Nuclear enhancement factor in calculation of Galactic diffuse gamma-rays: A new estimate with DPMJET-3. *Astroparticle Physics*, 31:341–343, June 2009.

[72] C. D. Dermer. Secondary production of neutral pi-mesons and the diffuse galactic gamma radiation. *Astronomy & Astrophysics*, 157:223–229, March 1986.

[73] Trevor C. Weekes. *Very High Energy Gamma-Ray Astronomy.* Institute of Physics Publishing, 2003.

[74] F.A. Aharonian. *Very High Energy Cosmic Gamma Radiation.* World Scientific, 2004.

[75] J. Holder. TeV gamma-ray astronomy: A summary. *Astroparticle Physics*, 39:61–75, December 2012.

[76] M. Ackermann, et al. The Imprint of the Extragalactic Background Light in the Gamma-Ray Spectra of Blazars. *Science*, 338:1190–, November 2012.

[77] A. Abramowski, et al. Measurement of the extragalactic background light imprint on the spectra of the brightest blazars observed with H.E.S.S. *Astronomy & Astrophysics*, 550:A4, February 2013.

[78] R. C. Gilmore, R. S. Somerville, J. R. Primack, and A. Domínguez. Semi-analytic modelling of the extragalactic background light and consequences for extragalactic gamma-ray spectra. *Monthly Notices of the Royal Astronomical Society*, 422:3189–3207, June 2012.

[79] M. Meyer, M. Raue, D. Mazin, and D. Horns. Limits on the extragalactic background light in the Fermi era. *Astronomy & Astrophysics*, 542:A59, June 2012.

[80] J.V. Jelley. *Cerenkov Radiation and its applications.* Pergamon Press, 1958.

[81] A. M. Hillas. Cerenkov light images of EAS produced by primary gamma. In F. C. Jones, editor, *International Cosmic Ray Conference*, volume 3 of *International Cosmic Ray Conference*, pages 445–448, August 1985.

[82] M. J. Berger and S. M. Seltzer. Tables of Energy Losses and Ranges of Electrons and Positrons. NASA SP-3012. *NASA Special Publication*, 3012, 1964.

[83] Malcom S. Longair. *High Energy Astrophysics, Volume 1.* Cambridge University Press, 1992.

[84] A. M. Hillas. Differences between Gamma-Ray and Hadronic Showers. *Space Science Reviews*, 75:17–30, January 1996.

[85] T. C. Weekes, et al. Observation of TeV gamma rays from the Crab nebula using the atmospheric Cerenkov imaging technique. *Astrophysical Journal*, 342:379–395, July 1989.

[86] S. P. Wakely and D. Horan. TeVCat: An online catalog for Very High Energy Gamma-Ray Astronomy. *International Cosmic Ray Conference*, 3:1341–1344, 2008.

[87] B. M. Gaensler and P. O. Slane. The Evolution and Structure of Pulsar Wind Nebulae. *Annual Review of Astronomy & Astrophysics*, 44:17–47, September 2006.

[88] A. A. Abdo, et al. Fermi Large Area Telescope Observations of the Crab Pulsar And Nebula. *Astrophysical Journal*, 708:1254–1267, January 2010.

[89] A. M. Hillas, et al. The Spectrum of TeV Gamma Rays from the Crab Nebula. *Astrophysical Journal*, 503:744, August 1998.

[90] A. M. Atoyan and F. A. Aharonian. On the mechanisms of gamma radiation in the Crab Nebula. *Monthly Notices of the Royal Astronomical Society*, 278:525–541, January 1996.

[91] L. Kuiper, et al. The Crab pulsar in the 0.75-30 MeV range as seen by CGRO COMPTEL. A coherent high-energy picture from soft X-rays up to high-energy gamma-rays. *Astronomy & Astrophysics*, 378:918–935, November 2001.

[92] J. Albert, et al. VHE γ-Ray Observation of the Crab Nebula and its Pulsar with the MAGIC Telescope. *Astrophysical Journal*, 674:1037–1055, February 2008.

[93] F. Aharonian, et al. Observations of the Crab nebula with HESS. *Astronomy & Astrophysics*, 457:899–915, October 2006.

[94] T. Tanimori, et al. Detection of Gamma Rays of up to 50 TeV from the Crab Nebula. *Astrophysical Journal Letters*, 492:L33, January 1998.

[95] O. Celik. Observations of the Crab Nebula and Pulsar with VERITAS. *International Cosmic Ray Conference*, 2:847–850, 2008.

[96] F. Aharonian, et al. The Crab Nebula and Pulsar between 500 GeV and 80 TeV: Observations with the HEGRA Stereoscopic Air Cerenkov Telescopes. *Astrophysical Journal*, 614:897–913, October 2004.

[97] D. A. Smith, et al. Mrk 421, Mrk 501, and 1ES 1426+428 at 100 GeV with the CELESTE Cherenkov telescope. *Astronomy & Astrophysics*, 459:453–464, November 2006.

[98] F. Aharonian, et al. Energy dependent γ-ray morphology in the pulsar wind nebula HESS J1825-137. *Astronomy & Astrophysics*, 460:365–374, December 2006.

[99] E. Aliu, et al. Observation of Pulsed γ-Rays Above 25 GeV from the Crab Pulsar with MAGIC. *Science*, 322:1221–, November 2008.

[100] E. Aliu, et al. (VERITAS Collaboration). Detection of Pulsed Gamma Rays Above 100 GeV from the Crab Pulsar. *Science*, 334:69–, October 2011.

[101] J. Aleksić, et al. Observations of the Crab Pulsar between 25 and 100 GeV with the MAGIC I Telescope. *Astrophysical Journal*, 742:43, November 2011.

[102] J. Aleksić, et al. Phase-resolved energy spectra of the Crab pulsar in the range of 50-400 GeV measured with the MAGIC telescopes. *Astronomy & Astrophysics*, 540:A69, April 2012.

[103] J. Aleksić, et al. Detection of bridge emission above 50 GeV from the Crab pulsar with the MAGIC telescopes. *ArXiv e-prints*, 1402.4219, February 2014.

[104] A. A. Abdo, et al. The Fermi Gamma-Ray Space Telescope Discovers the Pulsar in the Young Galactic Supernova Remnant CTA 1. *Science*, 322:1218–, November 2008.

[105] M. de Naurois, et al. Measurement of the Crab Flux above 60 GeV with the CELESTE Cerenkov Telescope. *Astrophysical Journal*, 566:343–357, February 2002.

[106] S. Oser, et al. High-Energy Gamma-Ray Observations of the Crab Nebula and Pulsar with the Solar Tower Atmospheric Cerenkov Effect Experiment. *Astrophysical Journal*, 547:949–958, February 2001.

[107] R. W. Lessard, et al. Search for Pulsed TEV Gamma-Ray Emission from the Crab Pulsar. *Astrophysical Journal*, 531:942–948, March 2000.

[108] S. Ohm, J. A. Hinton, and R. White. γ-ray emission from the Westerlund 1 region. *Monthly Notices of the Royal Astronomical Society*, 434:2289–2294, September 2013.

[109] A. Abramowski, et al. Discovery of extended VHE γ-ray emission from the vicinity of the young massive stellar cluster Westerlund 1. *Astronomy & Astrophysics*, 537:A114, January 2012.

[110] M. Lemoine-Goumard, E. Ferrara, M.-H. Grondin, P. Martin, and M. Renaud. Fermi-LAT detection of gamma-ray emission in the vicinity of the star forming regions W43 and Westerlund 2 . *Memorie della Societa Astronomica Italiana*, 82:739, 2011.

[111] A. Abramowski, et al. Revisiting the Westerlund 2 field with the HESS telescope array. *Astronomy & Astrophysics*, 525:A46, January 2011.

[112] R. C. G. Chaves, M. Renaud, M. Lemoine-Goumard, and P. Goret. HESS J1848-018: Discovery Of VHE γ-ray Emission From The Direction Of W 43. In F. A. Aharonian, W. Hofmann, and F. Rieger, editors, *American Institute of Physics Conference Series*, volume 1085 of *American Institute of Physics Conference Series*, pages 372–375, December 2008.

[113] F. Brun, et al. Discovery of VHE gamma-ray emission from the W49 region with H.E.S.S. *ArXiv e-prints*, 1104.5003, April 2011.

[114] S. Ohm, et al. H.E.S.S. Observations of Massive Stellar Clusters. In J. Martí, P. L. Luque-Escamilla, and J. A. Combi, editors, *High Energy Phenomena in Massive Stars*, volume 422 of *Astronomical Society of the Pacific Conference Series*, page 265, May 2010.

[115] M. Sakai, Y. Yajima, and H. Matsumoto. Nature of the Unidentified TeV Source HESS J1614-518, Revealed by Suzaku and XMM-Newton Observations. *Publications of the Astronomical Society of Japan*, 63:879, November 2011.

[116] A. Abramowski, et al. Very-high-energy gamma-ray emission from the direction of the Galactic globular cluster Terzan 5. *Astronomy & Astrophysics*, 531:L18, July 2011.

[117] C. Venter, O. C. De Jager, and A.-C. Clapson. Predictions of Gamma-Ray Emission from Globular Cluster Millisecond Pulsars Above 100 MeV. *Astrophysical Journal Letters*, 696:L52–L55, May 2009.

[118] V. A. Acciari, et al. VERITAS Observations of the TeV Binary LS I +61 303 During 2008-2010. *Astrophysical Journal*, 738:3, September 2011.

[119] V. A. Acciari, et al. Evidence for Long-Term Gamma-Ray and X-Ray Variability from the Unidentified TeV Source HESS J0632+057. *Astrophysical Journal Letters*, 698:L94–L97, June 2009.

[120] M. Chernyakova, et al. Multiwavelength observations of the binary system PSR B1259-63/LS 2883 around the 2010-2011 periastron passage. *Monthly Notices of the Royal Astronomical Society*, 439:432–445, March 2014.

[121] A. A. Abdo, et al. Fermi/LAT observations of LS 5039. *Astrophysical Journal Letters*, 706:L56–L61, November 2009.

[122] D. Hadasch, et al. Long-term Monitoring of the High-energy Gamma-Ray Emission from LS I +61 303 and LS 5039. *Astrophysical Journal*, 749:54, April 2012.

[123] M. Ackermann, et al. Periodic Emission from the Gamma-Ray Binary 1FGL J1018.6-5856. *Science*, 335:189–, January 2012.

[124] V. A. Acciari, et al. VERITAS Observations of the Gamma-Ray Binary LS I +61 303. *Astrophysical Journal*, 679:1427–1432, June 2008.

[125] V. A. Acciari, et al. Multiwavelength Observations of LS I +61 303 with Veritas, Swift, and RXTE. *Astrophysical Journal*, 700:1034–1041, August 2009.

[126] J. Albert, et al. Multiwavelength (Radio, X-Ray, and Gamma-Ray) Observations of the Gamma-Ray Binary LS I +61 303. *Astrophysical Journal*, 684:1351–1358, September 2008.

[127] F. Aharonian, et al. HESS Observations of the Galactic Center Region and Their Possible Dark Matter Interpretation. *Physical Review Letters*, 97(22):221102, December 2006.

[128] K. Tsuchiya, et al. Detection of Sub-TeV Gamma Rays from the Galactic Center Direction by CANGAROO-II. *Astrophysical Journal Letters*, 606:L115–L118, May 2004.

[129] K. Kosack, et al. TeV Gamma-Ray Observations of the Galactic Center. *Astrophysical Journal Letters*, 608:L97–L100, June 2004.

[130] J. Albert, et al. Observation of Gamma Rays from the Galactic Center with the MAGIC Telescope. *Astrophysical Journal Letters*, 638:L101–L104, February 2006.

[131] A. Abramowski, et al. Search for a Dark Matter Annihilation Signal from the Galactic Center Halo with H.E.S.S. *Physical Review Letters*, 106(16):161301, April 2011.

[132] P. L. Nolan, et al. Fermi Large Area Telescope Second Source Catalog. *Astrophysical Journal Supplement*, 199:31, April 2012.

[133] A. A. Abdo, et al. Spectrum and Morphology of the Two Brightest Milagro Sources in the Cygnus Region: MGRO J2019+37 and MGRO J2031+41. *Astrophysical Journal*, 753:159, July 2012.

[134] E. Aliu, et al. Observations of the Unidentified Gamma-Ray Source TeV J2032+4130 by VERITAS. *Astrophysical Journal*, 783:16, March 2014.

[135] A. R. Taylor, et al. The Canadian Galactic Plane Survey. *Astronomical Journal*, 125:3145–3164, June 2003.

[136] G. H. Rieke, et al. The Multiband Imaging Photometer for Spitzer (MIPS). *Astrophysical Journal Supplement*, 154:25–29, September 2004.

[137] E. Churchwell, et al. The Spitzer/GLIMPSE Surveys: A New View of the Milky Way. *Publications of the Astronomical Society of the Pacific*, 121:213–230, March 2009.

[138] R. A. Benjamin, et al. GLIMPSE. I. An SIRTF Legacy Project to Map the Inner Galaxy. *Publications of the Astronomical Society of the Pacific*, 115:953–964, August 2003.

[139] F. Comerón and A. Pasquali. New members of the massive stellar population in Cygnus. *Astronomy & Astrophysics*, 543:A101, July 2012.

[140] V. S. Avedisova. Catalog of Star-Forming Regions in the Galaxy (Avedisova, 2002). *VizieR Online Data Catalog*, 5112:0, July 2002.

[141] H. Krawczynski and E. Treister. Active galactic nuclei – the physics of individual sources and the cosmic history of formation and evolution. *Frontiers of Physics*, 8:609–629, December 2013.

[142] F. A. Aharonian. TeV gamma rays from BL Lac objects due to synchrotron radiation of extremely high energy protons. *New Astronomy*, 5:377–395, November 2000.

[143] A. A. Abdo, et al. Insights into the High-energy γ-ray Emission of Markarian 501 from Extensive Multifrequency Observations in the Fermi Era. *Astrophysical Journal*, 727:129, February 2011.

[144] A. Franceschini, G. Rodighiero, and M. Vaccari. Extragalactic optical-infrared background radiation, its time evolution and the cosmic photon-photon opacity. *Astronomy & Astrophysics*, 487:837–852, September 2008.

[145] J. Aleksić, et al. MAGIC Discovery of Very High Energy Emission from the FSRQ PKS 1222+21. *Astrophysical Journal Letters*, 730:L8, March 2011.

[146] A. Abramowski, et al. H.E.S.S. discovery of VHE γ-rays from the quasar PKS 1510-089. *Astronomy & Astrophysics*, 554:A107, June 2013.

[147] J. Aleksić, et al. MAGIC Observations and multiwavelength properties of the quasar 3C 279 in 2007 and 2009. *Astronomy & Astrophysics*, 530:A4, June 2011.

[148] F. Aharonian, et al. Is the giant radio galaxy M 87 a TeV gamma-ray emitter? *Astronomy & Astrophysics*, 403:L1–L5, May 2003.

[149] F. Aharonian, et al. Fast Variability of Tera-Electron Volt γ Rays from the Radio Galaxy M87. *Science*, 314:1424–1427, December 2006.

[150] V. A. Acciari, et al. Observation of Gamma-Ray Emission from the Galaxy M87 above 250 GeV with VERITAS. *Astrophysical Journal*, 679:397–403, May 2008.

[151] J. Albert, et al. Very High Energy Gamma-Ray Observations of Strong Flaring Activity in M87 in 2008 February. *Astrophysical Journal Letters*, 685:L23–L26, September 2008.

[152] F. Aharonian, et al. Discovery of Very High Energy γ-Ray Emission from Centaurus a with H.E.S.S. *Astrophysical Journal Letters*, 695:L40–L44, April 2009.

[153] J. Aleksić, et al. Detection of very-high energy γ-ray emission from NGC 1275 by the MAGIC telescopes. *Astronomy & Astrophysics*, 539:L2, March 2012.

[154] E. Aliu, et al. Discovery of a Very High Energy Gamma-Ray Signal from the 3C 66A/B Region. *Astrophysical Journal Letters*, 692:L29–L33, February 2009.

[155] V. A. Acciari, et al. (VERITAS Collaboration). A connection between star formation activity and cosmic rays in the starburst galaxy M82. *Nature*, 462:770–772, December 2009.

[156] F. Acero, et al. Detection of Gamma Rays from a Starburst Galaxy. *Science*, 326:1080–, November 2009.

[157] D. Berge, S. Funk, and J. Hinton. Background modelling in very-high-energy γ-ray astronomy. *Astronomy & Astrophysics*, 466:1219–1229, May 2007.

[158] A. Abramowski, et al. Discovery of gamma-ray emission from the extragalactic pulsar wind nebula N 157B with H.E.S.S. *Astronomy & Astrophysics*, 545:L2, September 2012.

[159] G. Schilling. *Flash! : the hunt for the biggest explosions in the universe*. Cambridge University Press, 2002.

[160] P. Mészáros. Theories of Gamma-Ray Bursts. *Annual Review of Astronomy & Astrophysics*, 40:137–169, 2002.

[161] P. Mészáros. Gamma ray bursts. *Astroparticle Physics*, 43:134–141, March 2013.

[162] J. Buckley, et al. The Status and future of ground-based TeV gamma-ray astronomy. A White Paper prepared for the Division of Astrophysics of the American Physical Society. *ArXiv e-prints*, 0810.0444, October 2008.

[163] T. A. Porter, R. P. Johnson, and P. W. Graham. Dark Matter Searches with Astroparticle Data. *Annual Review of Astronomy & Astrophysics*, 49:155–194, September 2011.

[164] E. Aliu. et al. VERITAS deep observations of the dwarf spheroidal galaxy Segue 1. *Physical Review D*, 85(6):062001, March 2012.

[165] T. Arlen, et al. Constraints on Cosmic Rays, Magnetic Fields, and Dark Matter from Gamma-Ray Observations of the Coma Cluster of Galaxies with VERITAS and Fermi. *Astrophysical Journal*, 757:123, October 2012.

[166] W. Galbraith and J. V. Jelley. Light Pulses from the Night Sky associated with Cosmic Rays. *Nature*, 171:349–350, February 1953.

[167] A. Konopelko, et al. (HEGRA Collaboration). Performance of the stereoscopic system of the HEGRA imaging air Čerenkov telescopes: Monte Carlo simulations and observations. *Astroparticle Physics*, 10:275–289, May 1999.

[168] R. Mukherjee, et al. The current status and future plans of the STACEE observatory. In S. Ritz, N. Gehrels, and C. R. Shrader, editors, *Gamma 2001: Gamma-Ray Astrophysics*, volume 587 of *American Institute of Physics Conference Series*, pages 932–936, October 2001.

[169] M. de Naurois. First Results & Future Prospects for 30 GeV Gamma Rays from CELESTE. In *International Cosmic Ray Conference*, volume 5 of *International Cosmic Ray Conference*, page 211, 1999.

[170] D. A. Smith. Review of the Solar Array Telescopes. *ArXiv Astrophysics e-prints*, astro-ph/0608251, August 2006.

[171] B. M. Vladimirsky, et al. Cerenkov Gamma-telescope GT-48 of the Crimean Astrophysical Observatory of the USSR Academy of Sciences. In A. A. Stepanian, D. J. Fegan, and M. F. Cawley, editors, *Very High Energy Gamma Ray Astronomy*, page 21, 1989.

[172] Gamma Telescope GT-48. http://lerga.crao.crimea.ua/Instr/gt48_en.html.

[173] T. Hara, et al. A 3.8 m imaging Cherenkov telescope for the TeV gamma-ray astronomy collaboration between Japan and Australia. *Nuclear Instruments and Methods in Physics Research A*, 332:300–309, July 1993.

[174] S. I. Nikolsky and V. G. Sinitsyna. Investigation of Gamma-sources by Mirror Telescopes. In A. A. Stepanian, D. J. Fegan, and M. F. Cawley, editors, *Very High Energy Gamma Ray Astronomy*, page 11, 1989.

[175] V. G. Sinitsyna, et al. TeV to PeV neutrinos and gamma-rays with Mountain SHALON Mirror Cherenkov Telescope. In *International Cosmic Ray Conference*, volume 5 of *International Cosmic Ray Conference*, pages 79–82, 2005.

[176] P. Armstrong, et al. The University of Durham Mark 6 Gamma Ray Telescope. *Experimental Astronomy*, 9:51–80, 1999.

[177] K. T. Brazier, A. Carraminana, P. M. Chadwick, T. R. Currell, and N. A. Dipper. The University of Durham Southern Hemisphere VHE gamma ray telescope. *Experimental Astronomy*, 1:77–99, 1989.

[178] A. Barrau, et al. The CAT imaging telescope for very-high-energy gamma-ray astronomy. *Nuclear Instruments and Methods in Physics Research A*, 416:278–292, October 1998.

[179] C. L. Bhat and et al. In *Proc. Workshop on VHE Gamma Ray Astronomy*, page 196, 1997.

[180] C. L. Kaul, K. Shanthi, C. L. Bhat, A. K. Tickoo, and R. K. Kaul. AGN Detection Ranges of MACE and TACTIC Imaging Gamma-Ray Telescopes. *Experimental Astronomy*, 8:187–210, 1998.

[181] Cangaroo ii: Our new eye for the gamma-ray sky. http://icrhp9.icrr.u-tokyo.ac.jp/c-ii.html.

[182] Y. Mizumura, et al. Searches for very high energy gamma rays from blazars with CANGAROO-III telescope in 2005-2009. *Astroparticle Physics*, 35:563–572, April 2012.

[183] D. B. Tridon, T. Schweizer, F. Goebel, R. Mirzoyan, M. Teshima, and MAGIC Collaboration. The MAGIC-II gamma-ray stereoscopic telescope system. *Nuclear Instruments and Methods in Physics Research A*, 623:437–439, November 2010.

[184] Y. Becherini, M. Punch, and H. E. S. S. Collaboration. Performance of HESS-II in multi-telescope mode with a multi-variate analysis. In F. A. Aharonian, W. Hofmann, and F. M. Rieger, editors, *American Institute of Physics Conference Series*, volume 1505 of *American Institute of Physics Conference Series*, pages 741–744, December 2012.

[185] J. Holder, et al. Status of the VERITAS Observatory. In F. A. Aharonian, W. Hofmann, and F. Rieger, editors, *American Institute of Physics Conference Series*, volume 1085 of *American Institute of Physics Conference Series*, pages 657–660, December 2008.

[186] E. Lorenz. The MAGIC Telescope, Status and Future Plans. In F. A. Aharonian, H. J. Völk, and D. Horns, editors, *High Energy Gamma-Ray Astronomy*, volume 745 of *American Institute of Physics Conference Series*, pages 622–627, February 2005.

[187] W. Benbow. The Status and Performance of H.E.S.S. In F. A. Aharonian, H. J. Völk, and D. Horns, editors, *High Energy Gamma-Ray Astronomy*, volume 745 of *American Institute of Physics Conference Series*, pages 611–616, February 2005.

[188] J. S. Perkins, G. Maier, and The VERITAS Collaboration. VERITAS Telescope 1 Relocation: Details and Improvements. *ArXiv e-prints*, 0912.3841, December 2009.

[189] D. Kieda. Status of the VERITAS Upgrade. *International Cosmic Ray Conference*, 9:14, 2011.

[190] J. M. Davies and E. S. Cotton. Design of the quartermaster solar furnace. *Journal of Solar Energy Science and Engineering*, 1:16–22, 1957.

[191] E. Roache, R. Irvin, J. S. Perkins, and et al. Mirror Facets for the VERITAS Telescopes. In *International Cosmic Ray Conference*, volume 3 of *International Cosmic Ray Conference*, pages 1397–1400, 2008.

[192] N. OTTE. Upgrade of VERITAS with high efficiency photomultipliers. In *International Cosmic Ray Conference*, volume 9 of *International Cosmic Ray Conference*, page 242, 2011.

[193] S. Le Bohec and G. Sleege. Design of the preamplifier for VERITAS. (VERITAS internal memo), March 2004.

[194] VERITAS Collaboration: T. Nagai, R. McKay, G. Sleege, and D. Petry. Focal Plane Instrumentation of VERITAS. *ArXiv e-prints*, 0709.4517, September 2007.

[195] R. Guenette. *VERITAS observations of galactic compact objects*. PhD thesis, McGill University (Canada, 2010.

[196] J. Grube, et al. VERITAS Pointing Monitor (VPM). (VERITAS internal memo), December 2011.

[197] VERITAS, Sub Project 8, Constant Fraction Discriminator. http://www.astro.ucla.edu/ veritas/subproj8.htm.

[198] A. Weinstein. The VERITAS Trigger System. In *International Cosmic Ray Conference*, volume 3 of *International Cosmic Ray Conference*, pages 1539–1542, 2008.

[199] C. Winkler, et al. The INTEGRAL mission. *Astronomy & Astrophysics*, 411:L1–L6, November 2003.

[200] M. Basset and AGILE Team. The AGILE gamma ray satellite. *Nuclear Instruments and Methods in Physics Research A*, 572:474–475, March 2007.

[201] W. B. Atwood, et al. The Large Area Telescope on the Fermi Gamma-Ray Space Telescope Mission. *Astrophysical Journal*, 697:1071–1102, June 2009.

[202] N. Gehrels, et al. The Swift Gamma-Ray Burst Mission. *Astrophysical Journal*, 611:1005–1020, August 2004.

[203] N. Gehrels, et al. Erratum: "The Swift Gamma-Ray Burst Mission". *Astrophysical Journal*, 621:558–558, March 2005.

[204] M. Ackermann, et al. The Fermi Large Area Telescope on Orbit: Event Classification, Instrument Response Functions, and Calibration. *Astrophysical Journal Supplement*, 203:4, November 2012.

[205] G. Sullivan and MILAGRO Collaboration. Status of the MILAGRO gamma ray observatory. In *International Cosmic Ray Conference*, volume 7 of *International Cosmic Ray Conference*, page 2773, August 2001.

[206] Physics with milagro. http://umdgrb.umd.edu/cosmic/milagro.html.

[207] A. Tepe and the Hawc Collaboration. HAWC - The High Altitude Water Cherenkov Detector. *Journal of Physics Conference Series*, 375(5):052026, July 2012.

[208] HAWC Collaboration. The HAWC Instrument: The HAWC Detector. http://www.hawc-observatory.org/observatory/#sec:wcd.

[209] A. A. Abdo, et al. TeV Gamma-Ray Sources from a Survey of the Galactic Plane with Milagro. *Astrophysical Journal Letters*, 664:L91–L94, August 2007.

[210] G. Marsella and ARGO-YBJ coll. ARGO-YBJ: a unique device for the EAS study. *Journal of Physics Conference Series*, 39:475–477, May 2006.

[211] C. Bacci, et al. Results from the ARGO-YBJ test experiment. *Astroparticle Physics*, 17:151–165, May 2002.

[212] B. Bartoli, et al. TeV Gamma-Ray Survey of the Northern Sky Using the ARGO-YBJ Detector. *Astrophysical Journal*, 779:27, December 2013.

[213] M. Amenomori, et al. The energy spectrum of all-particle cosmic rays around the knee region observed with the Tibet-III air-shower array. *Advances in Space Research*, 42:467–472, August 2008.

[214] M. Amenomori, et al. Multi-TeV Gamma-Ray Observation from the Crab Nebula Using the Tibet-III Air Shower Array Finely Tuned by the Cosmic Ray Moon's Shadow. *Astrophysical Journal*, 692:61–72, February 2009.

[215] M. Amenomori, et al. Performance of the Tibet-III Air Shower Array. *International Cosmic Ray Conference*, 5:3019, July 2003.

[216] D. Hanna, A. McCann, M. McCutcheon, and L. Nikkinen. An LED-based flasher system for VERITAS. *Nuclear Instruments and Methods in Physics Research A*, 612:278–287, January 2010.

[217] L. Valcarcel. *VERITAS, 1ES 1218 + 30.4 and the extragalactic background light.* PhD thesis, McGill University, Canada, 2008.

[218] D. Hanna. Measuring Single Photoelectrons with the LED-based Flasher System. (VERITAS internal memo), July 2011.

[219] G. Tesic and D. Staszak. D.C. to PE Ratio from Photostatistics and Single Photoelectron Runs. Internal VERITAS Collaboration Meeting presentation, June 2012.

[220] M. P. Kertzman and G. H. Sembroski. Computer simulation methods for investigating the detection characteristics of TeV air Cherenkov telescopes. *Nuclear Instruments and Methods in Physics Research A*, 343:629–643, April 1994.

[221] D. Heck. Corsika: A monte carlo code to simulate extensive air showers. Report FZKA 6019, 1998.

[222] G. Maier. Monte Carlo studies of the VERITAS array of Cherenkov telescopes. *International Cosmic Ray Conference*, 3:1413–1416, 2008.

[223] GrISU(tah). http://www.physics.utah.edu/gammaray/GrISU/.

[224] F. Schmidt. CORSIKA Shower Images. https://web.ikp.kit.edu/corsika/.

[225] H. Prokoph. *Observations and modeling of the active galactic nucleus B2 1215+30 together with performance studies of the ground-based gamma-ray observatories VERITAS and CTA.* PhD thesis, Mathematisch-Naturwissenschaftlichen Fakultät I der Humboldt-Universität zu Berlin, 2013.

[226] M.W. McCutcheon. *Search for VHE gamma-ray emission from the globular cluster M13 with VERITAS.* PhD thesis, McGill University (Canada, 2012.

[227] P. T. Reynolds, et al. Survey of candidate gamma-ray sources at TeV energies using a high-resolution Cerenkov imaging system - 1988-1991. *Astrophysical Journal*, 404:206–218, February 1993.

[228] S. Lebohec, C. Duke, and P. Jordan. Minimal stereoscopic analysis for imaging atmospheric Cherenkov telescope arrays. *Astroparticle Physics*, 24:26–31, September 2005.

[229] V. P. Fomin, et al. New methods of atmospheric Cherenkov imaging for gamma-ray astronomy. I. The false source method. *Astroparticle Physics*, 2:137–150, May 1994.

[230] T.-P. Li and Y.-Q. Ma. Analysis methods for results in gamma-ray astronomy. *Astrophysical Journal*, 272:317–324, September 1983.

[231] F. Aharonian, et al. The H.E.S.S. Survey of the Inner Galaxy in Very High Energy Gamma Rays. *Astrophysical Journal*, 636:777–797, January 2006.

[232] S. D. Biller. Hypothesis ranking and the context of probabilities in an open-ended search. *Astroparticle Physics*, 4:285–291, February 1996.

[233] M. H. Heyer, et al. The Five College Radio Astronomy Observatory CO Survey of the Outer Galaxy. *Astrophysical Journal Supplement*, 115:241, April 1998.

[234] M. Lemoine-Goumard, B. Degrange, and M. Tluczykont. Selection and 3D-reconstruction of gamma-ray-induced air showers with a stereoscopic system of atmospheric Cherenkov telescopes. *Astroparticle Physics*, 25:195–211, April 2006.

[235] NIST/Sematech e-Handbook of Statistical Methods. http://www.itl.nist.gov/div898/handbook/apr/section2/apr233.htm, 2012.

[236] F. Giordano, et al. Fermi Large Area Telescope Detection of the Young Supernova Remnant Tycho. *Astrophysical Journal Letters*, 744:L2, January 2012.

[237] A. Decourchelle, et al. XMM-Newton observation of the Tycho supernova remnant. *Astronomy & Astrophysics*, 365:L218–L224, January 2001.

[238] G. Maier. Systematic errors in spectral energy reconstruction. (VERITAS internal memo), October 2007.

[239] N. Park and the VERITAS Collaboration. Study of high energy cosmic ray acceleration in Tycho SNR with VERITAS. *ArXiv e-prints*, 1308.0610, August 2013.

[240] P. Slane, et al. Fermi Detection of the Pulsar Wind Nebula HESS J1640-465. *Astrophysical Journal*, 720:266–271, September 2010.

[241] G. Morlino and D. Caprioli. Strong evidence for hadron acceleration in Tycho's supernova remnant. *Astronomy & Astrophysics*, 538:A81, February 2012.

[242] S. P. Reynolds and D. C. Ellison. Electron acceleration in Tycho's and Kepler's supernova remnants - Spectral evidence of Fermi shock acceleration. *Astrophysical Journal Letters*, 399:L75–L78, November 1992.

[243] H. J. Völk, E. G. Berezhko, and L. T. Ksenofontov. Magnetic field amplification in Tycho and other shell-type supernova remnants. *Astronomy & Astrophysics*, 433:229–240, April 2005.

[244] H. J. Völk, E. G. Berezhko, and L. T. Ksenofontov. New evidence for strong non-thermal effects in Tycho's supernova remnant. *Astrophysics and Space Science*, 309:389–394, June 2007.

[245] H. J. Völk, E. G. Berezhko, L. T. Ksenofontov, and G. P. Rowell. The high energy gamma-ray emission expected from Tycho's supernova remnant. *Astronomy & Astrophysics*, 396:649–656, December 2002.

[246] E. G. Berezhko, L. T. Ksenofontov, and H. J. Völk. The Nature of Gamma-Ray Emission of Tycho's Supernova Remnant. *Astrophysical Journal*, 763:14, January 2013.

[247] G. Cassam-Chenaï, J. P. Hughes, J. Ballet, and A. Decourchelle. The Blast Wave of Tycho's Supernova Remnant. *Astrophysical Journal*, 665:315–340, August 2007.

[248] X. Zhang, Y. Chen, H. Li, and X. Zhou. On the hadronic γ-ray emission from Tycho's supernova remnant. *Monthly Notices of the Royal Astronomical Society*, 429:L25–L29, February 2013.

[249] R. Kothes, K. Fedotov, T. J. Foster, and B. Uyanıker. A catalogue of Galactic supernova remnants from the Canadian Galactic plane survey. I. Flux densities, spectra, and polarization characteristics. *Astronomy & Astrophysics*, 457:1081–1093, October 2006.

[250] T. Tamagawa, et al. Suzaku Observations of Tycho's Supernova Remnant. *Publications of the Astronomical Society of Japan*, 61:167, January 2009.

[251] A. Atoyan and C. D. Dermer. Gamma Rays from the Tycho Supernova Remnant: Multi-zone versus Single-zone Modeling. *Astrophysical Journal Letters*, 749:L26, April 2012.

[252] G. Ambrosi, et al. The Cherenkov Telescope Array Large Size Telescope. *ArXiv e-prints*, 1307.4565, July 2013.

[253] A. Barnacka, et al. Performance of the Cherenkov Telescope Array at energies above 10 TeV. *ArXiv e-prints*, 1307.3409, July 2013.

Appendix

PUBLICATION PERMISSIONS

Permissions for Figure 1.1

Both of these images are in the Public Domain

Permissions for Figure 1.2

Reproduced by permission of the original author(s) and the AAS

Permissions for Figure 2.1

License Number: 3390470610688
License date: May 15, 2014
Licensed content publisher: Springer
Licensed content publication: Space Science Reviews
Licensed content title: The Energy Spectra and Anisotropies of Cosmic Rays
Licensed content author: S.P. Swordy
Licensed content date: Jan 1, 2001
Volume number: 99
Issue number: 1
Type of Use: Thesis/Dissertation
Portion: Figures
Author of this Springer article: No
Original figure numbers: Figure 1
Title of your thesis / dissertation: Very High Energy Gamma-Ray Emission from Tycho's Supernova Remnant
Expected completion date: May 2014
Estimated size (pages): 190
Total: 0.00 USD

Permissions for Figure 2.2

From an email response from the Copyright Clearance Center: "Material may be republished in a thesis / dissertation without obtaining additional permission from Annual Reviews, providing that the author and the original source of publication are fully acknowledged."

Permissions for Figure 2.3

License Number: 3390490112236
License date: May 15, 2014

Licensed content publisher: Elsevier
Licensed content publication: Astroparticle Physics
Licensed content title: Gamma rays from supernova remnants
Licensed content author: Felix A. Aharonian
Licensed content date: March 2013
Licensed content volume number: 43
Number of pages: 10
Type of Use: reuse in a thesis/dissertation
Portion: figures/tables/illustrations
Number of figures/tables/illustrations: 1
Format: both print and electronic
Are you the author of this Elsevier article? No
Will you be translating? No
Title of your thesis/dissertation: Very High Energy Gamma-Ray Emission from Tycho's Supernova Remnant
Expected completion date: May 2014
Estimated size (number of pages): 190
Elsevier VAT number: GB 494 6272 12
Permissions price: 0.00 USD
VAT/Local Sales Tax: 0.00 USD / 0.00 GBP
Total: 0.00 USD

Permissions for Figure 2.4

Reproduced by permission of the original author(s) and the AAS

Permissions for Figure 2.5

License Number: 3390490875683
License date: May 15, 2014
Licensed content publisher: The American Association for the Advancement of Science
Licensed content publication: Science
Licensed content title: Detection of the Characteristic Pion-Decay Signature in Supernova Remnants
Licensed content author: M. Ackermann, M. Ajello, A. Allafort, L. Baldini, J. Ballet, G. Barbiellini, M. G. Baring, D. Bastieri, K. Bechtol, R. Bellazzini, R. D. Blandford, E. D. Bloom, E. Bonamente, A. W. Borgland, E. Bottacini, T. J. Brandt, J. Bregeon, M. Brigida, P. Bruel, R. Buehler, G. Busetto, S. Buson, G. A. Caliandro, R. A. Cameron, P. A. Caraveo, J. M. Casandjian, C. Cecchi, O. Celik, E. Charles, S. Chaty, R. C. G. Chaves, A. Chekhtman, C. C. Cheung, J. Chiang, G. Chiaro, A. N. Cillis, S. Ciprini, R. Claus, et al.
Licensed content date: Feb 15, 2013
Volume number: 339

Issue number: 6121
Type of Use: Thesis / Dissertation
Requestor type: Scientist/individual at a research institution
Format: Print and electronic
Portion: Figure
Number of figures/tables: 1
Order reference number: None
Title of your thesis / dissertation: Very High Energy Gamma-Ray Emission from Tycho's Supernova Remnant
Expected completion date: May 2014
Estimated size(pages): 190
Total: 0.00 USD

Permissions for Figures 3.1, 3.7, 7.3

Astronomy and Astrophysics
Editor in Chief: T. Forveille

T. Forveille
Astronomy & Astrophysics
Observatoire de Paris
61, avenue de l'Observatoire
75014 Paris, France

Tel.: 33 0(1) 43 29 05 41
Fax: 33 0(1) 43 29 05 57
e-mail: aanda.paris@obspm.fr
Web: http://www.aanda.org

merging
Annales d'Astrophysique
Arkiv for Astronomi
Bulletin of the Astronomical Institutes of the Netherlands
Bulletin Astronomique
Journal des Observateurs
Zeitschrift fur Astrophysik
Bulletin of the Astronomical Institutes of Czechoslovakia

Paris, May 19, 2014

Reprint Permission

Material:
Fig. 5 from Abramowski et al. 2013, A&A, 550, A4
Fig. 4 from Aharonian et al. 2006, A&A, 460, 365
Figs. 6&11 from Morlino & Caprioli, 2012, A&A, 538, A81

To be used in:
PhD dissertation, entitled, "Very High Energy Gamma-Ray Emission from Tycho's Supernova Remnant," to be published via ProQuest and the University of Delaware

Permission granted to:
Dana B. Saxon
Department of Physics and Astronomy
University of Delaware
dbsaxon@udel.edu

I hold copyright on the material referred to above, and hereby grant permission for its use as requested herewith. The credit should be given as follows:
Credit: Author, A&A, vol, page, year, reproduced with permission © ESO.

Thierry Forveille
A&A Editor-in-Chief

Sponsored by Argentina, Austria, Belgium, Brazil, Chile, Czech Republic, Denmark, Estonia, Finland, France, Germany, Greece, Hungary, Italy, Netherlands, Poland, Portugal, Slovak Republic, Spain, Sweden, and Switzerland.
Produced and distributed by EDP Sciences for ESO.

Permissions for Table 3.1

Order Detail ID: 64997685

Very high energy gamma-ray astronomy by WEEKES T Reproduced with permission of TAYLOR & FRANCIS GROUP LLC - BOOKS in the format Republish in a thesis/dissertation via Copyright Clearance Center.

Permissions for Figures 3.2 and 3.3

PERMISSION INVOICE

Inv. # P03B 24090

May 29, 2014

Dana Saxon
1412 Pawlings Rd.
Phoenixville, PA

CAMBRIDGE UNIVERSITY PRESS

32 Avenue of the Americas
New York, NY 10013-2473, USA

www.cambridge.org

Telephone 212 924 3900
Fax 212 691 3239

REFERENCE

ISBN:	HB 9780521756181	PB	Other
Author:	Malcolm S. Longair		
Title:	High Energy Astrophysics, 3rd Edition		
Selection/pp.:	Figure 4.17 on page 120; Figure 5.11 on page 149		
Additional:	Copyright © 2011 Malcolm S Longair. Reprinted with the permission of Cambridge University Press.		

USE

Reprint Title:	Very High Energy Gamma-Ray Emission from Tycho's Supernova Remnant
Publisher:	University of Delaware
Format:	dissertation / thesis
Quantity (Limit*):	100
Avail. Date:	2014

RIGHTS/ACKNOWLEDGEMENT

Permission is granted for nonexclusive rights throughout the World in the English language for interior text editorial use in the format described above only, including non-profit editions for the blind and handicapped. Please fully acknowledge our material and indicate the copyright notice as it appears in our publication, followed by the phrase "Reprinted with the permission of Cambridge University Press."
All requests from third parties to reproduce this material must be forwarded to Cambridge University Press.

FEES/RESTRICTIONS

$0.00

*This permission is restricted to the indicated format and quantity; for additional use, you must reapply for permission. This permission does not allow reprinting of any material copyrighted by or credited in our publication to another source; Cambridge disclaims all liability in connection with the use of such material without proper consent.
A COPY OF THIS INVOICE MUST ACCOMPANY PAYMENT. Payment is due upon receipt of invoice. Terms: Net 60 days. Make check payable to Cambridge University Press, Attn: Rights and Permissions. (Fed. I.D. #: 13-1599108.)

This permission does not supersede permission that may be required from the original source indicated in our publication.
This permission requires that you send zero (0) copies of your publication directly to our author and zero (0) copy of your publication to this office upon availability.

Authorization: Adam Hirschberg

Adam Hirschberg
Rights and Permissions Associate
ahirschberg@cambridge.org

Permissions for Figure 3.4

License number: 3390500023662
License date: May 15, 2014
Licensed content publisher: Springer
Licensed content publication: Space Science Reviews
Licensed content title: Differences between gamma-ray and hadronic showers
Licensed content author: A.M. Hillas
Licensed content date: Jan 1, 1996
Volume number: 75
Issue number: 1
Type of use: Thesis/Dissertation
Portion: Figures
Author of this Springer article: No
Original figure numbers: Figure 2
Title of your thesis/dissertation: Very High Energy Gamma-Ray Emission from Tycho's Supernova Remnant
Expected completion date: May 2014
Estimated size (pages): 190
Total: 0.00 USD

Permissions for Figure 3.5

Reproduced by permission of the original author

Permissions for Figure 3.6

Reproduced by permission of the original author(s) and the AAS

Permissions for Figure 3.8

License Number: 3390501048601
License date: May 15, 2014
Licensed content publisher: The American Association for the Advancement of Science
Licensed content publication: Science
Licensed content title: Detection of Pulsed Gamma Rays Above 100 GeV from the Crab Pulsar
Licensed content author: The VERITAS Collaboration, E. Aliu, T. Arlen, T. Aune, M. Beilicke, W. Benbow, A. Bouvier, S. M. Bradbury, J.H. Buckley, V. Bugaev, K. Byrum, A. Cannon, A. Cesarini, J.L. Christiansen, L. Ciupik, E. Collins-Hughes, M.P. Connolly, W. Cui, R. Dickherber, C. Duke, M. Errando, A. Falcone, J.P. Finley, G. Finnegan, L. Fortson, A. Furniss, N. Galante, D. Gall, K. Gibbs, G.H. Gillanders, S. Godambe, S. Griffin, J. Grube, R. Guenette, G. Gyuk, D. Hanna, J. Holder, H. Huan, G. Hughes, C.M. Hui, T.B. et al.
Licensed content date: Oct 7, 2011
Volume number: 334

Issue number: 6052
Type of use: Thesis/Dissertation
Requestor type: Author of the AAAS published paper
Format: Print and electronic
Portion: Figure
Number of figures/tables: 1
Order reference number: None
Title of your thesis/dissertation: Very High Energy Gamma-Ray Emission from Tycho's Supernova Remnant
Expected completion date: May 2014
Estimated size (pages): 190
Total: 0.00 USD

Permissions for Figure 3.9

Reproduced by permission of the original author(s) and the AAS

Permissions for Figure 3.10

Reproduced by permission of the original author(s) and the AAS

Permissions for Figure 3.11

Reproduced by permission of the original author(s) and the AAS

Permissions for Figure 3.12

I am a co-author of this paper. Following is a partial excerpt from www.nature.com/reprints/permission-requests.html:

"The authors of articles published by Nature Publishing Group, or the authors' designated agents, do not usually need to seek permission for re-use of their material as long as the journal is credited with initial publication. Since 2003, ownership of copyright in original research articles remains with the Authors, and provided that, when reproducing the Contribution or extracts from it, the Authors acknowledge first and reference publication in the Journal, the Authors retain the following non-exclusive rights:

- To reproduce the Contribution in whole or in part in any printed volume (book or thesis) of which they are they author(s).
- To reuse figures or table created by them and contained in the Contribution in other works created by them."

Permissions for Figure 4.1

Order Detail ID: 64997685

Very high energy gamma-ray astronomy by WEEKES T Reproduced with permission of TAYLOR & FRANCIS GROUP LLC - BOOKS in the format Republish in a thesis/dissertation via Copyright Clearance Center.

Permissions for Figure 4.2

Order Detail ID: 64997685

Very high energy gamma-ray astronomy by WEEKES T Reproduced with permission of TAYLOR & FRANCIS GROUP LLC - BOOKS in the format Republish in a thesis/dissertation via Copyright Clearance Center.

Permissions for Figure 4.3

Reproduced by permission of the original author

Permissions for Figure 4.4

Reproduced by permission of the original author

Permissions for Figure 4.5

Reproduced by permission of the original author

Permissions for Figure 4.9

Reproduced by permission of the original author

Permissions for Figure 4.10

Reproduced by permission of the original author(s) and the AAS

Permissions for Figure 4.11

Reproduced by permission of the original author(s) and the AAS

Permissions for Figure 4.12

Reproduced by permission of the original author

Permissions for Figure 4.13

Reproduced by permission of the original author(s) and the AAS

Permissions for Figure 5.6

Reproduced by permission of the original author(s)

Permissions for Figure 5.8

From http://www-zeuthen.desy.de/ jknapp/fs/: "You are invited to use these plots in theses, publications, etc.. If you do, please cite / acknowledge this website."

Permissions for Figure 5.10

Order Detail ID: 64997685

Very high energy gamma-ray astronomy by WEEKES T Reproduced with permission of TAYLOR & FRANCIS GROUP LLC - BOOKS in the format Republish in a thesis/dissertation via Copyright Clearance Center.

Permissions for Figure 5.12

License Number:3390530824943
License date: May 15, 2014
Licensed content publisher: Elsevier
Licensed content publication: Astroparticle Physics
Licensed content title: Minimal stereoscopic analysis for imaging atmospheric Cherenkov telescope arrays
Licensed content author: S. LeBohec,C. Duke,P. Jordan
Licensed content date: September 2005
Licensed content volume number: 24
Licensed content issue number: 1-2
Number of pages: 6
Type of Use: reuse in a thesis/dissertation
Portion: figures/tables/illustrations
Number of figures/tables/illustrations: 1
Format: both print and electronic
Are you the author of this Elsevier article? No
Will you be translating? No
Title of your thesis/dissertation: Very High Energy Gamma-Ray Emission from Tycho's Supernova Remnant
Expected completion date: May 2014
Estimated size (number of pages): 190
Elsevier VAT number: GB 494 6272 12
Permissions price: 0.00 USD
VAT/Local Sales Tax: 0.00 USD / 0.00 GBP
Total: 0.00 USD

Permissions for Figures 6.3 and 6.4

Licensed content publisher: Elsevier
Licensed content publication: Astroparticle Physics
Licensed content title: Selection and 3D-reconstruction of gamma-ray-induced air showers with a stereoscopic system of atmospheric Cherenkov telescopes
Licensed content author: M. Lemoine-Goumard,B. Degrange,M. Tluczykont
Licensed content date: April 2006
Licensed content volume number: 25
Licensed content issue number: 3
Number of pages: 17
Type of Use: reuse in a thesis/dissertation

Portion: figures/tables/illustrations
Number of figures/tables/illustrations: 2
Format: both print and electronic
Are you the author of this Elsevier article? No
Will you be translating? No
Title of your thesis/dissertation: Very High Energy Gamma-Ray Emission from Tycho's Supernova Remnant
Expected completion date: May 2014
Estimated size (number of pages): 190
Elsevier VAT number: GB 494 6272 12
Permissions price: 0.00 USD
VAT/Local Sales Tax: 0.00 USD / 0.00 GBP
Total: 0.00 USD

Permissions for Figure 6.7

Reproduced by permission of the original author(s) and the AAS

Permissions for Figure 6.8

Reproduced by permission of the original author(s) and the AAS

Permissions for Figure 6.10

Reproduced by permission of the original author

Permissions for Figure 7.1

Reproduced by permission of the original author(s) and the AAS

Permissions for Figure 7.2

Reproduced by permission of the original author(s) and the AAS

Permissions for Figure 7.4

Reproduced by permission of the original author(s) and the AAS

Permissions for Figure 7.5

From www.oxfordjournals.org/access_purchase/rights_permissions_ras.html:

"You are not required to obtain permission to reuse figures (including tables) for academic, educational or non-commercial research for the following material provided full acknowledgment is given to the original source including Figure Number, Title of the Article, Author, Journal Title and Volume or Issue.

Post 1998: a maximum of two figures (including tables) from a journal article or five figures per journal issue (unless a separate copyright holder is identified in such figure, in which event permission should be sought from that holder)."

Permissions for Figure 7.6

Reproduced by permission of the original author(s) and the AAS

Permissions for Figure 7.7

Reproduced by permission of the original author

Permissions for Figure 7.9

Reproduced by permission of the original author